Eindhoven University of Technology

MASTER

Novel APC-methods for accurate pattern determination

van Norel, J.

Award date:
1993

Link to publication

TECHNISCHE UNIVERSITEIT EINDHOVEN

FACULTEIT ELEKTROTECHNIEK

VAKGROEP Elektromagnetisme

Novel APC-methods for accurate
pattern determination

by

J. van Norel

EM-6-93

Eindhoven, 16 juni 1993.

Preface

This final work has been performed in the period of August 1992 - June 1993 at the Electromagnetics Group, Eindhoven University of Technology, Eindhoven under supervision of Dr.ir. V.J. Vokurka. It is based on an original idea to correct antenna radiation patterns for reflections in anechoic rooms. The latter consists of measuring at different positions, so that the reflecting component can be distinguished from the measurements by making use of the different change in phase of the direct and reflecting component between positions. For, the reflecting signal travels another path as the main signal. In fact a synthetic aperture has been created this way which allows to distinguish different signals.

As one can suspect a lot of experimental work had to be done. For example the realization of an automated linear scan axis and the development of accurate measurements of the distances between positions took a great deal of time. Also much time has been spend on the design of a solid and fast algorithm and on extensive verification measurements. The programming language is Fortran to be compatible with the ARCS-software. The results of the new technique are very promising. In literature several other methods had been found for correcting or suppressing environmental effects on antenna measurements, but none of them is easy applicable. However nowadays there is a real need for accurate antenna measurements and correction for the presence of extraneous fields is an important item. I hope that the new technique, based on a simple idea, will be a new step in performing accurate antenna measurements on compact ranges. Finally I wish to thank all members of the Electromagnetics Group for their support of this project.

Summary

Nowadays there is an increasing need for accurate antenna measurements. Far-field ranges do no longer meet the stringent requirements. Therefore, near-field testing has been grown to a form of maturity. Further improvements are achieved by reducing the effects of error sources. Several sources of error are present in the measurements, among which extraneous fields are very important. The appropriate use of high-quality absorber materials is very effective. Recently, a few techniques have been developed for suppression of the effects of field irregularities. Each one of them has specific benefits and drawbacks. However the most practical and frequently used technique is time-gating. To cope with the problems accompanying time-gating a new technique has been developed for making accurate pattern measurements. This technique has been called "novel APC-methods", for the implementation resembles a lot the well-known APC-method. The realization is quite simple without the need for extra equipment. Corrections are made for both mutual coupling and extraneous fields. Extensive verifications show reliable corrections can be made. As a drawback the technique is only suitable for high-gain antennas. However it is just this type of antenna that suffers the most from large mutual coupling on the mainlobe and disturbances on the low-sidelobes due to extraneous fields. The prospects for the "novel APC-method" in future seem promising because it offers a good concurrence to other techniques.

List of abbreviations

APC   : antenna pattern comparison
AUT   : antenna under test
CATR   : compact antenna-test range
CW   : continuous wave
EUT   : Eindhoven University of Technology
FF   : far field
FFT   : fast Fourier transform
IF   : intermediate frequency
NF   : near field
NPWAS : non-plane wave aperture synthesis
PWS   : plane wave spectrum
PSAS   : probe scan/antenna scan
SNR   : signal-to-noise ratio
SPCR   : single-plane collimating range
VSWR   : voltage standing wave ratio

Contents

Chapter 1

Introduction

The development of modern satellite and radar antenna technologies has placed stringent requirements on testing and evaluation of the antenna and system performance. The importance of high-quality measuring ranges is evident. Traditional far-field measurement ranges can no longer satisfy many current requirements. Various techniques for antenna testing have been developed since the late sixties but near-field test techniques have emerged to dominate the scene. Nowadays these techniques have evolved to a state of maturity. Therefore an increasing attention is paid for the investigation to sources of error in these techniques [1,2,3,4]. There are many sources of error as can be observed from [5,6]. One factor that affects the accuracy in measurements is the presence of extraneous fields in the test zone of the antenna measurement range. Extraneous fields are for example created by reflections of the field produced by the range antenna. Several techniques have been developed to compensate for the environmental effects on the measurement [7,8,9,10,11,12,13].

The purpose of this final work is to develop a new technique for correction of antenna measurements for extraneous fields. The technique is referred to as "Novel APC-methods" because there is a lot resemblance with the famous APC-method. In chapter 2 the antenna measurement techniques will be reviewed. Chapter 3 is devoted to the error sources that might be present in a measurement system. Of course special attention is paid to the effects of extraneous fields in the test zone. Two well-known techniques are presented to characterize the performance of the anechoic chamber. It should be noticed that an overall knowledge of the error sources is necessary to correct for one of them. Chapter 4 deals with the existing correction techniques for field irregularities. Especially emphasized is the technique of deconvolution processing because this approach gives a good insight in the antenna measurement problem by using the concept of a plane-wave spectrum. Also important is time-gating, for this is the most frequently used technique to remove unwanted responses from the measurements. In chapter 5 the new technique is presented. First, the theory of this

technique and its implementation is explained. Then the algorithm to process the measurement data is outlined. Finally, the experimental results and a discussion follows. Throughout the explanation of the implementation also the influence of other error sources will be considered. The benefits and drawbacks of every technique in chapter 4 and 5 will be treated. Chapter 6 will finish this report with a conclusion.

Chapter 2

Antenna measurement techniques

2.1 Introduction

This chapter is an introduction to antenna measurements. Several methods for testing antennas will be concerned. But first a discussion about field regions follows.

2.2 Field regions

The distribution of field strength around an antenna is a function of the distance from the antenna. Three field regions are distinguished to express field distributions in zones surrounding the antenna, see figure 2.1.
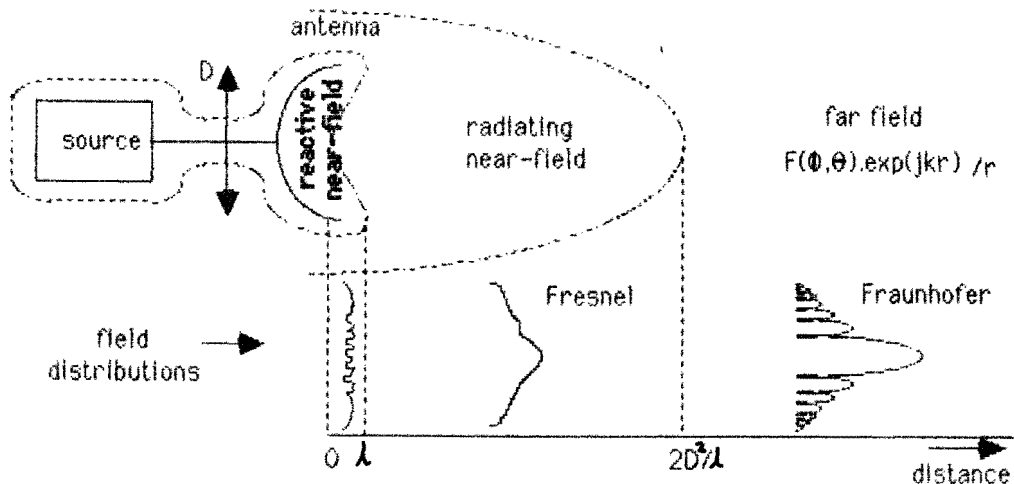

Figure 2.1 *Exterior field of radiating antenna.*

3

In close proximity to the antenna the reactive field predominates. The strength of the reactive field components decays rapidly with the distance from the antenna. A reasonable outer boundary to the reactive near-field region is about a wavelength. Beyond the reactive near-field region the radiating field predominates. The radiating region is divided in two subregions: radiating near-field region and the far-field region. In the radiating near-field region the angular distribution of the field (radiation pattern) is dependent on the distance from the antenna. This region is often referred to as the Fresnel region in analogy to optical terminology.

In the far-field region the angular distribution of the field becomes essentially independent of distance. Correspondingly the amplitude of the field is given by the reciprocal of the first power of distance. For an antenna focused at infinity, the optical term Fraunhofer region can be used.

A commonly used criterion to define the distance to the boundary between the Fresnel and Fraunhofer region is

$$R = \frac{2D^2}{\lambda} , \qquad (2.1)$$

where D is the largest dimension of the aperture and λ is the wavelength.

This theory of field regions is essential in understanding the following antenna measurement methods:
* far-field testing
* near-field testing:
    - NF/FF methods,
    - plane-wave synthesis,
    - compact antenna-test range,
    - hybrid testing.

2.3 Far-field testing

The measurement of the far-field radiation pattern of an antenna requires an illuminating plane-wave front. Traditionally this condition was achieved by situating the AUT at a large distance of the source antenna. In general distances equal to or larger than that given in eqn. (2.1) are sufficient. However, the wave illuminating the AUT is part of a spherical wave and still should be regarded as a pseudo plane-wave at large distances. For example with the separation given by eqn. (2.1) a phase variation of 22.5° at the edges of the AUT relative to the centre will be obtained. Larger range distances are required for measurement of antennas with very low sidelobes; the ideal case is infinity. The influence of phase curvature on sidelobes will be explained in

section 3.3. Large antennas operating at high frequencies may need test ranges of 1 km or more. Other problems concerning outdoor ranges are the dependence upon the weather conditions, interference by other sources and reflections.

2.4 Near-field testing

It is obvious that far-fields measurement ranges do not satisfy many of the stringent requirements on testing modern antennas. Current requirements for accurate knowledge of the far-field patterns of microwave antennas have led towards the development of several sophisticated techniques for the extraction of this information from near-field measurements. These measurements can be performed indoor, providing a controlled environment. Reflections can be minimized by covering the walls with high-quality RF absorbing materials such that an anechoic chamber is obtained. The most important antenna-test methods will be discussed now briefly.

NF/FF-methods

In these methods the near-field of the AUT is measured on a certain surface [14,15]. Then analytical methods are used to transform the measured near field to the far-field radiation pattern. Such methods are well established and exhibit high quality predictions, but require large measurement times and extensive data manipulation.
Three possible arrangements are planar, cylindrical and spherical scanning. The corresponding NF/FF-transformation algorithms are based on expressing the near field as a summation of planar (plane waves), cylindrical (Hankel functions) or spherical (spherical-wave functions) modes. Next these mode expansions can be processed to derive the far-field radiation patterns. Among these three is spherical near-field scanning the most complete method since the near field can be collected over the entire sphere. On the other hand planar scanning is the most simple technique. Sometimes probe correction is necessary to account for the radiation pattern of the scanning probe.

Plane-wave synthesis

The method of plane-wave synthesis is in fact an alternative for the NF/FF-method. The idea is to generate virtually a plane wave in the region of the AUT. In practice this could be achieved by means of a phased array. However by introducing the concept of a synthesized aperture, the phased array can be replaced by a single moving element. Generally a probe is taken to scan the surface of a plane, cylinder or a sphere surrounding the AUT. After this the radiation pattern of the AUT can be computed by

summing the responses multiplied by an appropriate weighting function. The weighting coefficients must be equivalent to those of the phased array that could have been virtually used. Just like the other NF/FF-methods does plane-wave synthesis require large measurement times and computer power [16].

Compact antenna-test range

The compact antenna-test range is attractive since it provides a direct measurement of the far-field pattern of the AUT by generating a plane wave in the test zone and thus avoids the need for increased measurement times and data processing. The plane wave is usually created by reflectors that collimate the radiation from a point source [17]. The AUT, located close to the reflector(s), is then illuminated by a wave front which is approximately uniform in amplitude and phase. The quality of the pseudo plane-wave across the test zone is the most important indicator of the range performance as far as measurement accuracy is concerned.

Design problems having influence on the quality of the plane wave in the test area are [18]:
- direct radiation from the source feed,
- diffraction of the edges of the reflector(s),
- wall reflections,
- feed characteristics,
- surface accuracy,
- cross-polarization performance,
  etc.

Another important characteristic of the CATR is the size of the test zone. This is determined by the maximal allowable taper and ripple of the field. The CATR at Eindhoven University of Technology belongs to the class of two-reflector CATR's. An impression of such a range is given in figure 2.2.
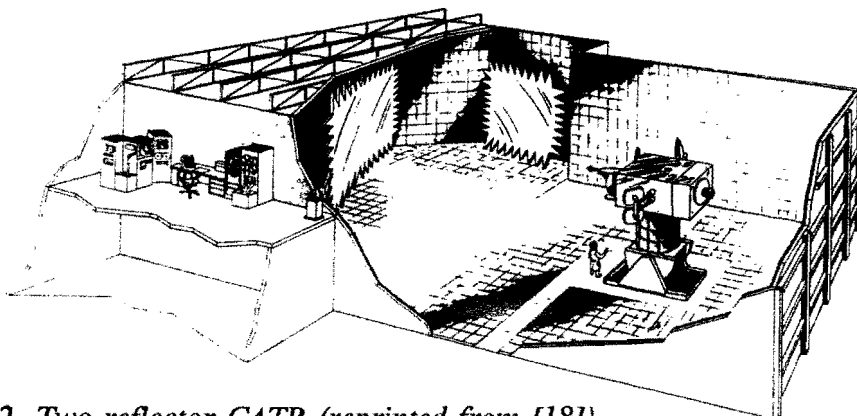

Figure 2.2 Two-reflector CATR (reprinted from [18]).

The system consists of two parabolic cylinders positioned perpendicular to each other. When illuminated by a spherical source the resulting wavefront in the aperture of the main reflector will have a plane-wave character.

Hybrid testing

Hybrid techniques combine the attributes of compact ranges and NF/FF-methods. In general they perform the integration along one of the two axes in real time with the use of a suitable line source probe. Thereafter only the measurement of a single array of data along a single cut over the other axis is required. Hence the result is a reduction of data acquisition requirements and faster processing algorithms. An implementation of the hybrid approach is the Single-Plane Collimating Range (SPCR) at EUT [19]. In conventional cylindrical near-field scanning techniques, the near fields are probed on a cylindrical surface surrounding the antenna in a 2-dimensional way. In the SPCR a cylindrical wave is generated using a single parabolic reflector in combination with a spherical source. Now scanning is reduced to one dimension and a 1-dimensional NF/FF-algorithm computes the far-field pattern. So the advantages of the hybrid approach are indeed a reduction of data acquisition and processing time. Due to the diverging character of the wavefront in one plane, this system is suitable for antennas having large physical dimensions.

Chapter 3

Error sources in antenna measurements

3.1 Introduction

There are many sources of error that affect antenna measurements. In addition the total measurement error is a complex summation of the contribution of every single error source in the entire measurement and data processing system. In practice it is impossible to divide the entire system in subsystems thereby isolating the error sources, then determine every error contribution and finally join them to find the total error of the entire system. This is due to the complex interaction between subsystems and their error sources. Therefore the calculation of an error budget is a difficult task. Quantitative information about error sources is difficult to get so an error budget is mainly based on estimations. Then the result must be considered as an upper-bound error.

The aim of this chapter is to show the kinds of errors to be aware of during antenna measurements. On most indoor antenna test ranges are field irregularities the most important factor among all error sources. However elimination of this factor requires at least a knowledge of the other error sources due to the complex nature of the total measurement error. Eventually this knowledge can be used to suppress other errors for a better elimination of field irregularities and higher accuracies. In literature more can be found about suppressing them. However it is important to notice that only systematic error sources can be corrected. The effect of random errors in measurements is expressed by the signal-to-noise ratio.

In the following section a full description is given about the extraneous fields including two techniques for the determination of reflectivity levels. Then in the next section a summation of the other most well known error sources is given.

3.2 Extraneous fields

Different kinds of extraneous fields may be present:
* Extraneous fields created by reflections and scattering of the field produced by the range antenna.
  These fields comprise:
  - near-axis incident fields from the region in front of the test area, for example caused by the serrated edges of the compact range mirror,
  - wide-angle incident fields from wide angles from the line-of-sight, for example caused by reflections against the chamber walls.
* Extraneous fields created by leakage of the range antenna system, for example direct radiation from the range-feed to the test zone.
* Mutual coupling between the range antenna and the AUT due to multiple reflections.
* Mutual coupling between the range antenna and the AUT due to inductive coupling; usually negligible when the separation is greater then ten wavelength.

On outdoor ranges also extraneous fields of other interfering sources may be present, but this will not be considered in this report. All of these fields produce unwanted ripple in the range field. This situation is illustrated in figure 3.1.
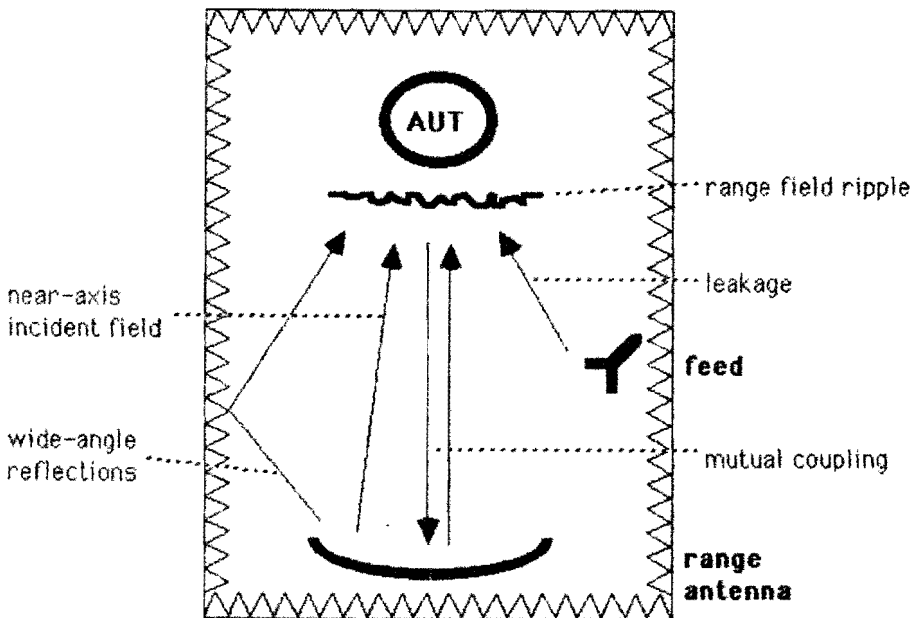

Figure 3.1   Range field ripple created by extraneous fields.

The ripple in the test-zone field is a complex variation, caused by the interference of the main field with many extraneous fields falling in from different directions. The main field, or direct signal, can be represented by a vector $\overline{E}_d$. The extraneous field is a vector sum of several components arriving from different parts of the chamber. This sum can be represented by the vector $\overline{E}_r$. The signal $\overline{E}_r$ will cause errors in measurements. A theoretical evaluation of the error is prevented due to the very complicated diffraction problem of finding the total interference pattern between $\overline{E}_d$ and $\overline{E}_r$. For determining the errors experimentally much time is required, since measurements of the extraneous field should be made at a sufficient number of points, so that it is possible to derive the constructive and destructive interference between $\overline{E}_d$ and $\overline{E}_r$ at every point in a specified test zone. This zone is the volume in which the actual measurements are made and is included in the so-called quiet zone of the anechoic chamber. The quiet zone is the volume of the chamber in which certain specifications with respect to uniformity of the field are met. The extent of the quiet zone may for example be made dependent on how large an amplitude and phase difference of $\overline{E}_d$ is specified between the centre and the edge of the quiet zone. The quietness of this zone depends on the magnitude of extraneous fields. A typical interference pattern may for example be shown in figure 3.2.
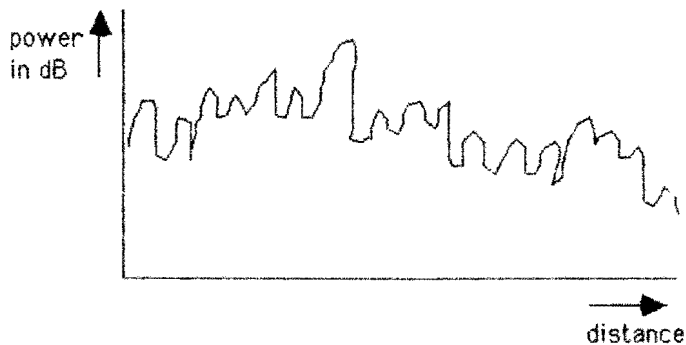

Figure 3.2 Interference pattern.

Interference patterns are measured by moving a receiving antenna along a line in the quiet zone, while sampling the field. The variations in the recorded pattern as illustrated in figure 3.2 are due to two effects. The first effect is the aforementioned constructive and destructive interference between the extraneous signal and the direct signal. The second effect is variations in amplitude of the direct and extraneous signal. In general the main field is a plane wave, its amplitude being constant. However the vector $\overline{E}_r$, that represents an equivalent signal for all extraneous fields being present, will cause variations in distance.

In the above, the specification of the test zone was in terms of the overall amplitude and phase variations. Another method to describe the test zone performance is in terms of reflectivity level. The reflectivity level R is defined as the ratio of the field strength of the equivalent signal $|\overline{E}_r|$ and the direct signal $|\overline{E}_d|$ in decibels:

$$R = 20LOG(\frac{E_r}{E_d}) \qquad (3.1)$$

Two test methods are frequently used for measuring the reflectivity level inside a quiet zone: the Antenna Pattern Comparison technique (APC) and the free-space Voltage Standing Wave Ratio technique (VSWR) [20].

3.2.1 APC-technique

This technique is based on the premise that in the absence of extraneous signals any two patterns recorded with the same geometrical relationship between the incident field and the receiving antenna will be identical. If, on the other hand, antenna patterns are measured for several different positions of the receiving antenna, and the pattern exhibits changes from position to position, then this indicates the presence of extraneous signals. To illustrate the effect that extraneous signals have on the measured pattern of a directive antenna, consider the situation depicted in figure 3.3.
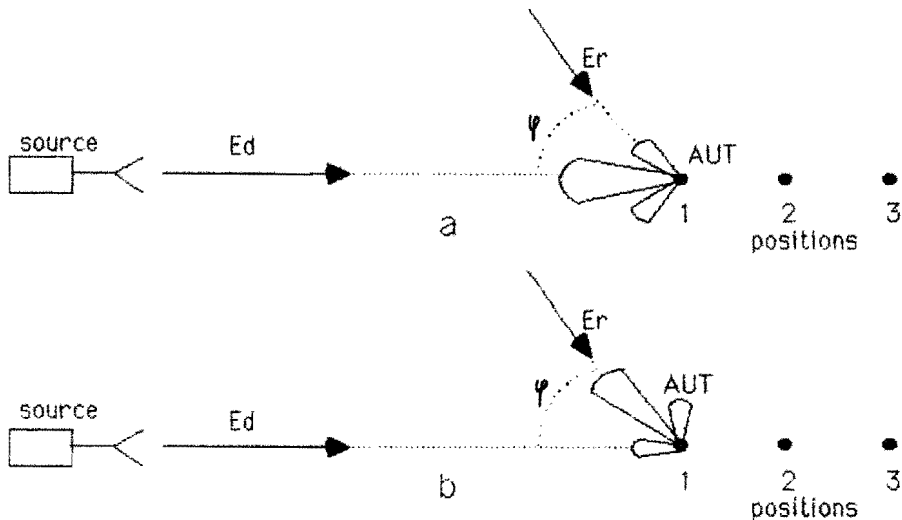
Figure 3.3 *Illustration of how sidelobe levels of AUT are affected.*
a) AUT pointing toward source
b) sidelobe pointing toward source

A reflected wave is incident from a direction φ degrees from the test antenna's main beam axis. Usually the level of the wide-angle reflected waves is at least 30 dB below the level of the direct wave. When the AUT is oriented so that its main beam is pointing toward the source antenna the reflected wave is received on a sidelobe, see figure 3.3a. The effect upon the measured level of the main beam is negligible. However if the antenna is rotated such that the major lobe is pointing toward the

direction of the reflected wave, then the level of the sidelobe deviates significantly, see figure 3.3b. The actual deviation depends upon the relative amplitude and phase of the direct and reflected wave.

The graphs in figure 3.4 are very useful to determine the possible error in the relative amplitude pattern of the test antenna due to an extraneous signal.
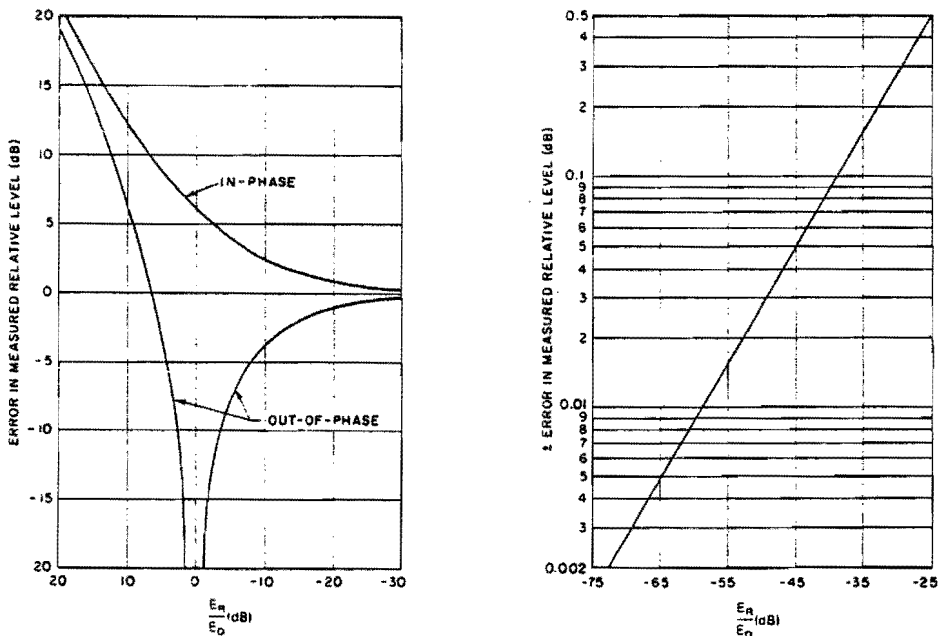

Figure 3.4   *Possible error in the measured relative pattern level due to a coherent extraneous signal.*

Consider as an example figure 3.3 and assume that the measured sidelobe level is 25 dB below the maximum level and the signal E_r is 40 dB below the main signal E_d. Then in figure 3.3a $20LOG(E_r/E_d) = -65dB$ which results in ± 0.005 dB error in the mainlobe according to the graph.

And in figure 3.3.b $20LOG(E_r/E_d) = -15dB$ which results in -1.70 dB to +1.42 dB error in the sidelobe according to the graph. These errors given in the graph may also be calculated according to eqn. (3.2).

$$error = 20LOG(\frac{E_d \pm E_r}{E_d}) = 20LOG(1 \pm \frac{E_r}{E_d}) \quad [dB] \tag{3.2}$$

If the azimuthal pattern of the AUT is measured at several positions along the range axis, variations will occur in the resulting pattern because of the change in the relative path-lengths of the two waves. The APC-method then consists of recording the azimuthal patterns of an AUT for different positions along the range axis. The separation between the successive positions must be chosen such as to obtain the

maximum deviation in sidelobe levels.

Another useful APC-method is recording two patterns about a fixed centre of rotation for the AUT as shown in figure 3.5.
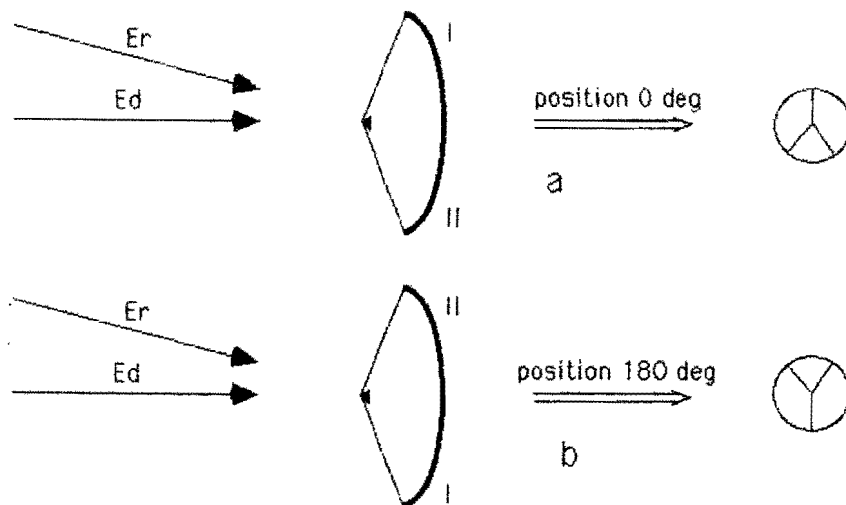

Figure 3.5   *APC-method that employs a rotation of the AUT around the main beam axis.*

The rotation of the AUT around the main beam axis results in another view to the extraneous field sources in the chamber when recording pattern cuts. Because the rotation is 180° there is no need to change the polarization of the range antenna between cuts. When the pattern recorded at 180° is reversely plotted over the pattern at 0° there will be deviations because reflections from the left side differ from reflections from the right side of the chamber. From these data one can deduce the apparent direction from which the extraneous signal is incident upon the antenna. An important limitation is that this method of rotation is only applicable to antennas without any backlash. This means that the electrical axis must be identical to the mechanical axis of rotation.

From APC-data reflectivity levels can be calculated. Let us consider the situation in figure 3.6.
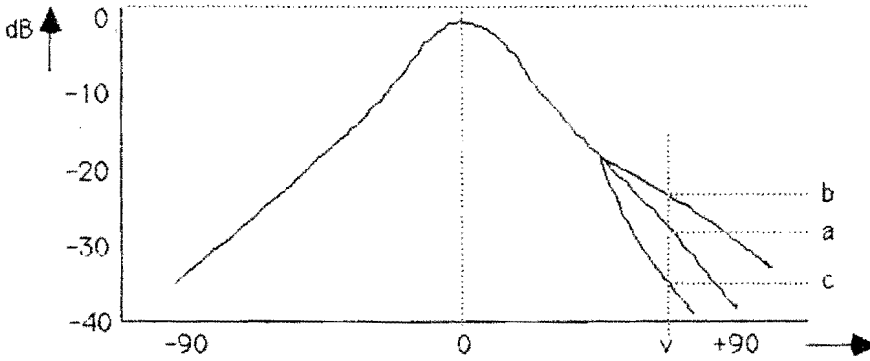
Figure 3.6 *Derivation of reflectivity levels from APC-data.*

Let the pattern level in dB at the angle v be a(v) and let the detected field be b(v) and c(v) when the direct signal E_d and the extraneous signal E_r are detected in-phase and out-of-phase respectively. Then:

$$a(v) = 20LOG(\frac{E_d(v)}{E_d(0)}) \quad [dB] \tag{3.3}$$

$$b(v) = 20LOG(\frac{E_d(v) + E_r(v)}{E_d(0)}) = 20LOG(\frac{E_d(0) \cdot 10^{\frac{a(v)}{20}} + E_r(v)}{E_d(0)}) \quad [dB] \tag{3.4}$$

$$c(v) = 20LOG(\frac{E_d(v) - E_r(v)}{E_d(0)}) = 20LOG(\frac{E_d(0) \cdot 10^{\frac{a(v)}{20}} - E_r(v)}{E_d(0)}) \quad [dB] \tag{3.5}$$

And the reflectivity level:

$$R = 20LOG(\frac{E_r(v)}{E_d(0)}) = 20LOG(\frac{10^{\frac{b(v)}{20}} - 10^{\frac{c(v)}{20}}}{2}) \quad [dB] \tag{3.6}$$

It is important to notice that in antenna radiation patterns the reflectivity level at angle v is determined as the quotient of the extraneous signal that disturbs the pattern at an angle v and the direct signal at the angle 0°, in dB.

Example:
Assume a variation of 1 dB top-top is noticed on a pattern level of -30 dB. Then the linear variation top-top is:

$$10^{\frac{-29.5}{20}} - 10^{\frac{-30.5}{20}} = 0.00364$$

Thus the reflectivity level $R = 20LOG(0.00364/2) = -55dB$. The graph in figure 3.7, based on eqn. (3.6), is very convenient in the determination of reflectivity levels from APC-data without the need to calculate.
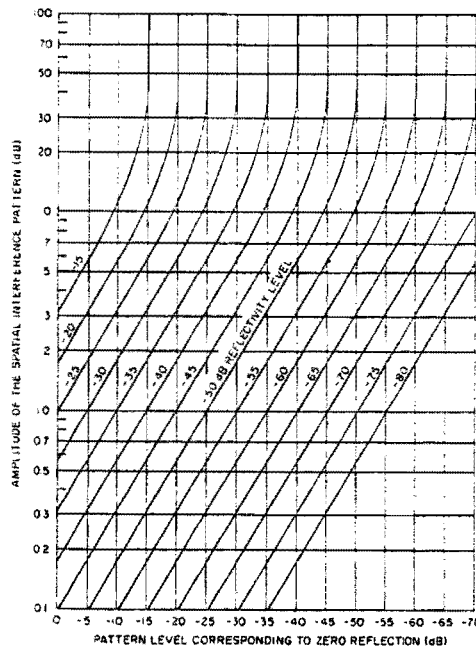

Figure 3.7   *Amplitude of spatial interference pattern for a given reflectivity level and pattern level.*

The APC-method is unable to detect all details of the standing-wave pattern because of the complexity of the interferences. But it conveniently gives a preliminary indication of the accuracy of antenna measurements. Another advantage of this method is that amplitude data is sufficient for determination of the reflectivity level. Phase information is not required. The VSWR-technique is a more accurate method for measuring the reflectivity level in an anechoic chamber.

3.2.2 Free-space VSWR-technique

The method uses a probe to measure the field in the quiet zone as a function of the probe position. Typically, a number of scans are made with different aspect angles to obtain complete interference pattern information. The result of these measurements depends upon the radiation pattern of the probe antenna. For example incoming signals

arriving at angles within pattern nulls are discriminated. This effect is avoided by the use of an omnidirectional probe. The advantage of this type of probe is that complete reflectivity information can be obtained with only three orthogonal scans [21]. The reflectivity levels are derived from the maximum amplitude variations in the recorded interference patterns. In general this system yields higher reflectivity levels than that obtained with a directional antenna since the equivalent reflected wave is composed of all the reflectivity waves from all surfaces. Sometimes it is better to use a directional antenna to obtain extra resolution for the location of the source of reflection. Then remedial action can be taken.

If there is only one principal source of reflection contributing to the incident field, it is a rather simple matter to locate it from the measured data. Suppose that the direct wave is incident upon the test zone from a direction perpendicular to the plane of the test zone and the extraneous wave arrives at an angle θ with respect to that direction. From figure 3.8 it is seen that an interference pattern over the test zone results.
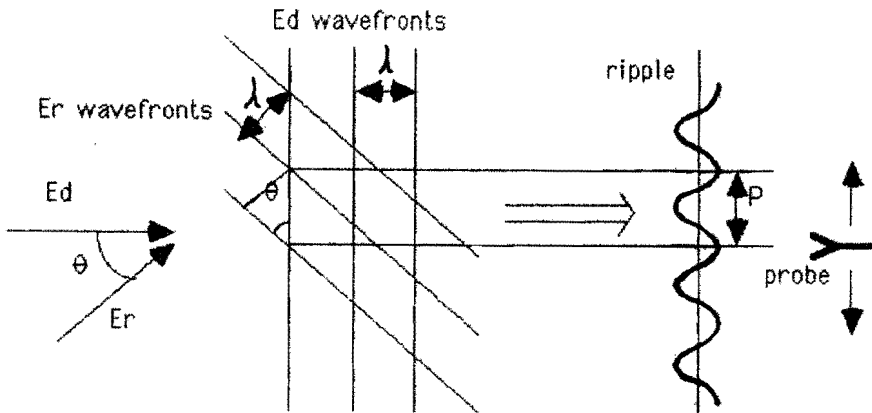
Figure 3.8 Geometrical relations for transversal probing.

The spatial period P of the resultant wave form is given by

$$P = \frac{\lambda}{SIN\theta} \tag{3.7}$$

It is seen from eqn. (3.7) that by probing the field in the test zone over lines perpendicular to the direction of propagation of the direct wave the direction from which the extraneous signal arrives can be determined. This way of probing is called transversal field probing because the movement of the probe is transverse to the range axis.

Another way is longitudinal field probing, thereby moving a probe longitudinally along the range axis. Figure 3.9 illustrates the geometrical relationship of the direct path and the extraneous signals, and the line of probe travel.
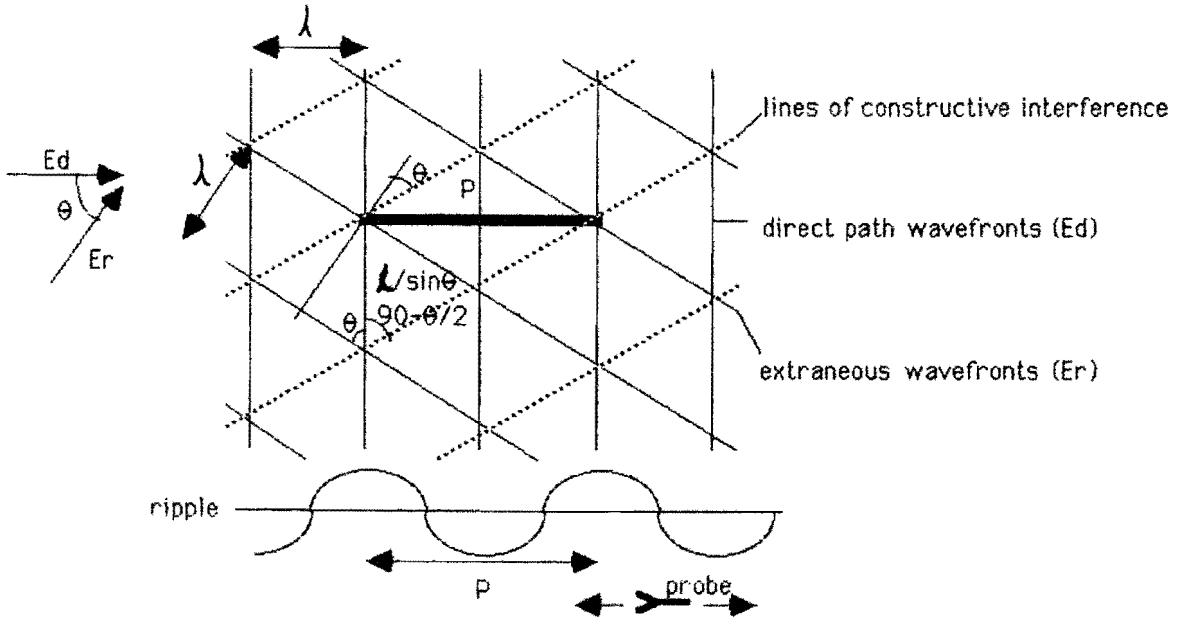
Figure 3.9 *Geometrical relations for longitudinal probing.*

As a result of this geometrical relationship, the spatial period can be derived:

$$P = \frac{\lambda}{2 \cdot SIN^2(\frac{\theta}{2})} = \frac{\lambda}{1 - COS\theta} \tag{3.8}$$

Again by noting the period of the amplitude variation of the received signal, the direction to the source of extraneous energy may be determined. Besides transversal or longitudinal probing of course other variations of field probing may be applied.

The reflectivity level of the interfering signal relative to the desired direct-path signal may be approximately determined by considering the peak-to-peak amplitude variation of the received signal in conjunction with the radiation pattern of the probe. First, consider the probe as omnidirectional and just a single disturbing signal is present. Then the total interference signal E_t can be thought of to be composed of the direct signal E_d and the extraneous signal E_r. In vector notation all possible amplitudes of E_t can be shown.
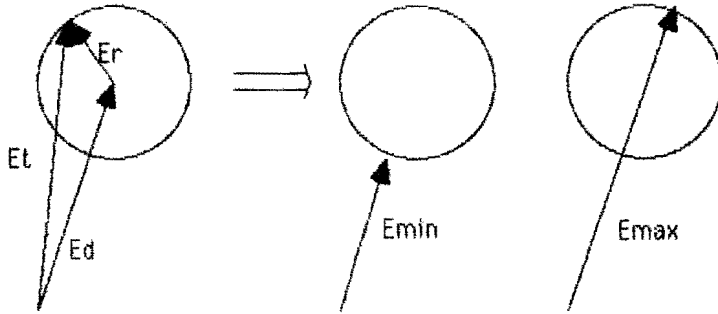
Figure 3.10 $\vec{E}_t = \vec{E}_d + \vec{E}_r$

Of course in figure 3.10 frequency and polarization of the extraneous signal E_r and the direct signal E_d are the same. Relating to figure 3.10 an expression is derived between E_d/E_r and the peak-to-peak values of E_t:

$$\sigma = 20LOG(\frac{E_{max}}{E_{min}}) = 20LOG(\frac{E_d + E_r}{E_d - E_r}) \quad [dB]$$

$$\Rightarrow \ 20LOG(\frac{E_r}{E_d}) = 20LOG(\frac{10^{\sigma/20} - 1}{10^{\sigma/20} + 1}) \quad [dB]$$

(3.9)

In the case of an omnidirectional probe eqn. (3.9) expresses the ratio of field strengths of the extraneous signal to the direct signal. Now consider the probe is directive. In conjunction to the recorded amplitude variations now also the relative gain of the probe antenna in the directions of the desired and interfering signals must be considered. So in general the reflectivity level R may be calculated from the peak-to-peak ripple σ (dB) of the recorded interference pattern using

$$R = P + 20LOG(\frac{10^{\sigma/20} - 1}{10^{\sigma/20} + 1}) \quad [dB]$$

(3.10)

where P is the relative power pattern in dB (negative value) of the probe in the direction v. It can be easily shown that eqn. (3.10) equals eqn. (3.6) by remarking that

$$E_{max}(v) - E_{min}(v) = 2E_r(v)$$
$$E_{max}(v) + E_{min}(v) = 2E_d(v)$$

(3.11)

where v is the angle.
Finally, we will finish the description of the VSWR-technique by remarking that all measurements should be made with both vertical and horizontal polarization and different frequencies. For, the reflectivity level depends upon polarization and frequency. From the discussion of the VSWR-technique it is concluded that a complete evaluation using this method is very time consuming.

3.3 Other error sources

Besides the presence of extraneous fields there are several other sources of error that affect the accuracy in antenna measurements. If one wants to improve the accuracy by eliminating the influence of extraneous fields on radiation patterns, a knowledge of the other important error sources is inevitable. That is why in this section a short description is given of all well-known error sources, differentiated in categories.

I) Errors inherent to the measurement technique

* Scan plane truncation
   In planar or cylindrical near-field scanning only a finite area in space around the AUT is being scanned. The field outside this area will be unknown, causing an error in the far-field prediction. However if the scan zone is large enough, fields outside this region can be neglected, so the error is small. A spherical test setup doesn 't suffer this problem.

* Mutual coupling
   Because the distance between source antenna and AUT is relative small on a near-field range, the mutual coupling between both antennas is inevitably larger than on a far-field range.

* Aliasing
   On near-field ranges often sampling is employed. When the sampling spacing does not obey Nyquist's theorem (minimal 1 sample/$\frac{\lambda}{2}$) aliasing will occur. This causes an error in the far-field prediction.

* Non-plane wave illumination
   A true far-field measurement requires the AUT to be illuminated by a plane wave having a uniform amplitude and phase. This condition can only be achieved in theory by measuring the AUT at infinity from the source antenna. A good approximation of the far-field criterion that is commonly employed is a minimal range length of

$$R = \frac{2D^2}{\lambda} \, , \tag{3.12}$$

where D is the diameter of the source antenna. Using this criterion there will still be a significant phase curvature ($\leq 22.5°$) that has its largest effects on the first null. In figure 3.11 the effect of the separation distance on the radiation pattern is shown.
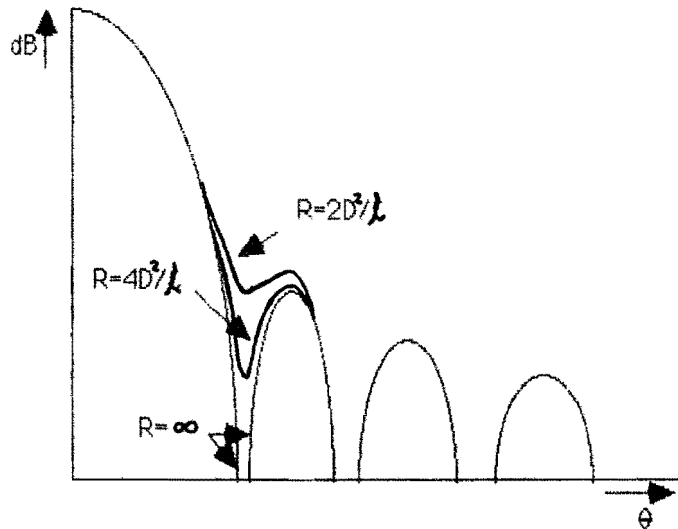
Figure 3.11 The effect of phase curvature at different distances.

Figure 3.11 shows that the effect of phase variation is that nulls of the pattern are partially filled and the amplitudes of the sidelobes are changed.

Modern compact ranges often are optimized to produce very low phase taper in the test zone, sometimes at the expense of amplitude taper. The amplitude taper that large antennas see near the edges of the quiet zone lowers the gain and distort the sidelobes as illustrated in figure 3.12.
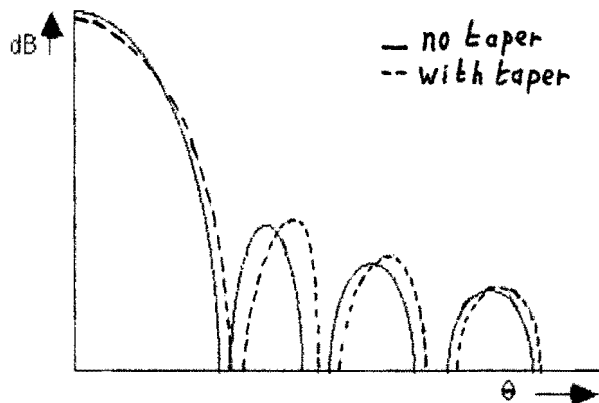

Figure 3.12 The effect of amplitude taper.

II) RF-path error sources

* Cable variations

   In making measurements of microwave signals there often arises the need to pass the signal through a moving RF-path. But torsion and bending of RF-cables contribute to changes in electrical length in addition to temperature variations. This has the

most impact on the phase stability ($\pm 1°$). Minimization of cable motion and temperature changes suppresses phase drift in time. Several techniques have been developed for correction of cable variations such as the three-cable method [22,23].

* Rotary joint
  To minimize cable motion rotary joints are often employed, but this introduces extra discontinuities due to connectors etc. and only very good rotary joints provide a phase stability in the order of $\pm 1°$.

* Connectors
  Reflections arise from connectors and other discontinuities in the RF-path.

* RF-path leakage
  Microwave leakage in the RF-system can seriously corrupt the antenna measurement. For example leakage via connectors is prevented by taping them with copper foil.

III) Instrumentation errors

* Receiver sensitivity
  Sensitivity or noise floor is defined as the average noise floor of the receiver at the RF-input port without averaging. If an antenna has very low sidelobes high sensitivity is recommended for high accuracy since noise may not affect the antenna's signal too much. High sensitivity allows more dynamic range.

* Receiver isolation
  Isolation or crosstalk is the signal in one receiver channel appearing on another receiver channel. If an antenna has very low sidelobes a low crosstalk will prevent significant errors in one channel due to signal on another channel.

* Receiver linearity
  Linearity or dynamic accuracy is a measure of the error in conversion gain as an RF-signal varies in power. This will affect the accuracy of the measurement as the signal changes during the measurement of the sidelobes.

* Non-zero response time of the receiver
  IF-settling errors can result if measurements are made before allowing the receiver IF to settle to a steady state after an abrupt change in amplitude and phase of the input signal.

* Antenna-receiver mismatch

Mismatch between the receiver and the AUT can be a significant cause of antenna gain measurement inaccuracy [3]. Reflections arise from the mismatch as illustrated in figure 3.13. Receiver and antenna are well matched when $\Gamma_R.\Gamma_A=0$.
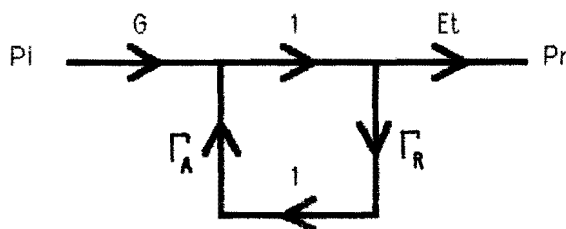
P_i = incident signal
P_R = received signal
E_t = receiver tracking error
Γ_R = reflection coefficient of receiver
Γ_A = reflection coefficient of antenna
G = antenna gain

Figure 3.13 *Flowgraph illustrating mismatch between antenna and receiver.*

* Source power variations

Modern transmitters provide a levelled output power so that variations in source power are no problem.

* Output frequency accuracy

Modern transmitters are synthesized so the frequency will always be correct.

IV) Positioning errors

Mechanical positioning is inherent to antenna pattern measurements. In general on a far-field range or on a Compact Range with collimators only an azimuth-over-elevation positioner is sufficient. In a NF/FF-measurement setup employing planar, cylindrical or spherical scanning often a probe scanner is used. The positioning of the probe is according to the appropriate grid belonging to the scanning method (e.g. planar, cylindrical, spherical). By positioning errors of the probe errors arise in the near-field data. Equivalently after NF/FF-transformation errors occur in the far-field data. Positioning errors can be divided in two categories:
- mechanical positioning errors,
- errors in position measurement.
Other important factors in positioning are the law of gravitation and vibrations due to driving gear etc.

V) Polarization mismatch

A crosspolar component in the range field introduces errors in the measured radiation pattern of the AUT.

VI) Computational errors

Quantization of the measurement data by the acquisition system and approximations and assumptions made in the data processing algorithm produce errors in the far-field radiation pattern.

Chapter 4

Correction techniques for field irregularities

4.1 Introduction

On current antenna test ranges a very important factor that affects the accuracy in measurements are field irregularities.

Field irregularities are caused by:
* Range-amplitude and -phase errors such as taper (non-plane-wave illumination).
* The presence of extraneous fields.

The extraneous fields can be divided in (see section 3.2):
* Extraneous fields created by reflections and scattering of the field produced by the range antenna.
* Extraneous fields created by leakage of the range antenna system.
* Mutual coupling between the range antenna and the AUT.

The need to reduce the effects of field irregularities in an antenna measurement will become even more important as accuracy requirements become stringent. Ideally the antenna test zone should be free of reflections and interferences and should be illuminated with an electromagnetic field of uniform amplitude and phase, i.e. a plane wave. One way to reduce the effect of extraneous fields is to modify the range environment. This modification could include locating and removing or suppressing the extraneous fields by covering the reflecting, scattering or leaking object with absorber. Environmental modification techniques improve measurement accuracy in an antenna range, but this improvement is limited because extraneous fields cannot always be completely removed or suppressed. Another way is using a certain correction technique for removal of the effect of field irregularities from the radiation pattern. This chapter deals with the existing techniques and shows its advantages and disadvantages. It

should be noted that some techniques not only remove or suppress the effects of extraneous fields, but also suppress the influence of range-amplitude and -phase errors on antenna radiation patterns.

4.2 Deconvolution processing

The idea behind the technique of deconvolution processing is to first characterize the test environment and then use this signature to remove unwanted effects from subsequent test antenna scans through a form of deconvolution processing. This technique will be explained extensively because it gives a good insight in the measurement problem of an antenna illuminated by a non-plane-wave. We will first focus our attention on the characterization of the test-zone field by plane-wave spectral analysis [7,25]. Next the correction of antenna measurements using this concept is explained [8,24,26].

4.2.1 Plane wave spectral analysis

To measure the far field pattern of an antenna, it must be situated in a test zone where the field is a uniform plane wave. The expression for a uniform plane wave propagating in the $\bar{k}$ direction is

$$\bar{E} = \bar{A}(\bar{k}) e^{-j\bar{k}\cdot\bar{r}} \tag{4.1}$$

where:
* $\bar{k} = k_x \bar{u}_x + k_y \bar{u}_y + k_z \bar{u}_z$ is the complex wavenumber and $k = \dfrac{\omega}{c} = \dfrac{2\pi}{\lambda}$
* $\bar{r} = x\bar{u}_x + y\bar{u}_y + z\bar{u}_z$ is the position vector
* $\bar{A}(\bar{k}) = A_x \bar{u}_x + A_y \bar{u}_y + A_z \bar{u}_z$ is the complex amplitude of the wave
* $\bar{k}\cdot\bar{A}(\bar{k}) = 0$ is the plane wave condition

At a fixed frequency only two components of $\bar{k}$ are specified independently since $\bar{k}$ is determined by the frequency and the properties of the medium. So the argument of the amplitude vector can be expressed by $\bar{A}(k_x, k_y)$.

In practice it is impossible to create a perfect plane wave in the test zone. For example the test-zone field generated by a CATR approximates a local plane wave as illustrated in figure 4.1
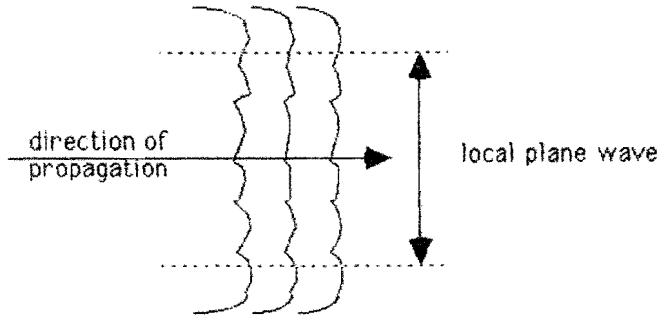
Figure 4.1 Pseudo plane wave of CATR.

The test-zone field can be expanded in terms of spectral components. Mathematical convenient expansions are planar, cylindrical or spherical modes. In our case it is obvious to choose an expansion in terms of plane-wave spectral components. For, the antenna should ideally be illuminated by a perfect plane wave. Plane-wave spectral analysis is a widely known concept to describe the quality of a wavefront in the test zone [7,25,26]. If the wavefront is sampled in amplitude and phase over the test zone in a plane perpendicular to the direction of propagation of the direct wave, the $\vec{E}$ and $\vec{H}$ field may be written as:

$$\vec{E}(\vec{r}) = \int\limits_{-\infty}^{\infty} \int\limits_{-\infty}^{\infty} \vec{A}(k_x,k_y)e^{-j\vec{k}\cdot\vec{r}}dk_x dk_y$$

$$\vec{H}(\vec{r}) = \frac{\vec{k}\times\vec{E}(\vec{r})}{kZ}$$

(4.2)

under the same conditions as eqn. (4.1) and linearity of the field equations and the medium. $\vec{A}(k_x,k_y)$ is called the plane wave spectrum because eqn. (4.2) represents a summation of uniform plane waves propagating in the directions $\vec{k}$.

Suppose that in the plane $z=0$ the components of the electric field are prescribed by means of an antenna aperture, then:

$$\vec{E}(x,y,0) = \vec{E}_a(x,y) = E_{ax}(x,y)\vec{u}_x + E_{ay}(x,y)\vec{u}_y$$

(4.3)

For $z=0$ the x- and y-polarized components are 2-dimensional Fourier transforms of the corresponding spectra A_x and A_y:

$$E_{ax}(x,y) = \int_{-\infty}^{\infty} \int_{-\infty}^{\infty} A_x(k_x,k_y) e^{-j(k_x x + k_y y)} dk_x dk_y$$

$$E_{ay}(x,y) = \int_{-\infty}^{\infty} \int_{-\infty}^{\infty} A_y(k_x,k_y) e^{-j(k_x x + k_y y)} dk_x dk_y$$

(4.4)

or inverted:

$$A_x(k_x,k_y) = \frac{1}{4\pi^2} \int_{-\infty}^{\infty} \int_{-\infty}^{\infty} E_{ax}(x,y) e^{j(k_x x + k_y y)} dx dy$$

$$A_y(k_x,k_y) = \frac{1}{4\pi^2} \int_{-\infty}^{\infty} \int_{-\infty}^{\infty} E_{ay}(x,y) e^{j(k_x x + k_y y)} dx dy$$

(4.5)

Writing eqn. (4.4) and (4.5) in short notation:

$$E_{ax}(x,y) = F[A_x(k_x,k_y)]$$
$$E_{ay}(x,y) = F[A_y(k_x,k_y)]$$

(4.6)

and

$$A_x(k_x,k_y) = F^{-1}[E_{ax}(x,y)]$$
$$A_y(k_x,k_y) = F^{-1}[E_{ay}(x,y)]$$

(4.7)

For example (1D), if a test region contains the wavefront s(x), where

$$s(x) = 1 + 0.2 COS(\frac{2\pi}{P}x)$$

(4.8)

Then as shown in figure 4.2, the unwanted residual is

$$r(x) = 0.2 COS(\frac{2\pi}{P}x) = 0.1 e^{j\frac{2\pi}{P}x} + 0.1 e^{-j\frac{2\pi}{P}x}$$

(4.9)
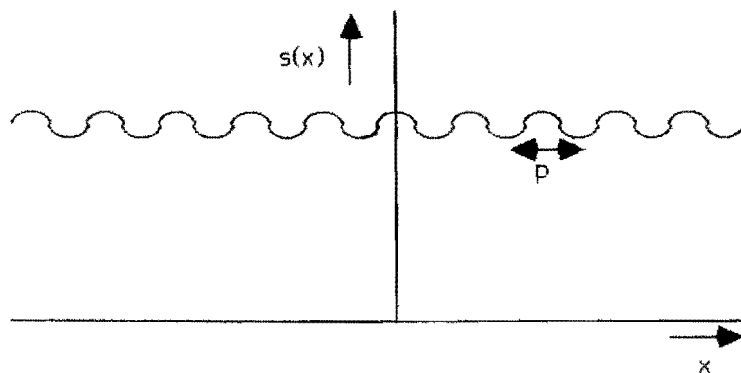
Figure 4.2 Wavefront in test region.

r(x) can therefore be composed from two plane waves, each of magnitude 0.1, incident from the directions $SIN\theta = \pm \frac{\lambda}{P}$, where λ is the wavelength of operation. A Fourier transformation of s(x) produces the PWS shown in figure 4.3 ($S(\theta)=F[s(x)]$) and indicates that the residuals are at a level of 20log(0.1) = -20 dB relative to the main source.
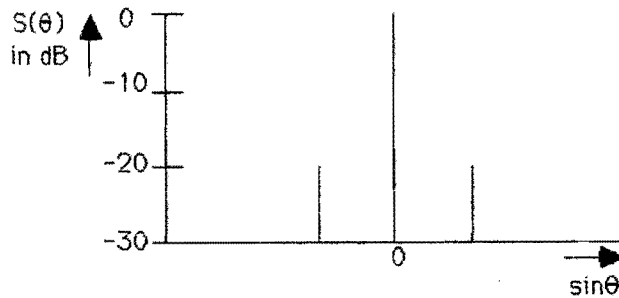
Figure 4.3 *Plane wave spectrum of s(x).*

There are two practical considerations concerning the previous example. First the sampling of the range field takes place on a finite surface that comprises the test zone. If the recorded amplitude and phase are constant and the assumption is made that the field is zero elsewhere (compare figure 4.1), then it behaves like a rectangular function. The spectrum of this field is a sinc-function. It seems now that the description of the field in terms of plane-wave spectra is not very useful, since it cannot be evaluated easy. Therefore, in practice a periodic expansion of the measured data is necessary before spectral analysis. The rectangular function leads to a plane wave after periodic expansion, which results in a delta-function at the origin of the spectral domain. The periodic function differs from the actual overall test-zone field, but this is not a problem because only the performance of the actual test-zone region is of importance. Secondly we consider the 1-dimensional evaluation of the test-zone field in the example of figure 4.2. Suppose that the field is measured in the plane y=0 such that $E_{ax}(x,0)$ is known. The 1-dimensional inverse-Fourier transform of this function can be written as

$$a_x(k_x) = \frac{1}{2\pi} \int\limits_{-\infty}^{\infty} E_{ax}(x,0)e^{jk_x x}dx \qquad (4.10)$$

The spectrum $a_x(k_x)$, which corresponds to figure 4.3, can be interpreted as a projection of the 2-dimensional spectrum $A_x(k_x,k_y)$ on the k_x-axis. This can be seen readily taking the 2-dimensional Fourier transform of $A_x(k_x,k_y)$ for y=0:

$$E_{ax}(x,0) = \int\limits_{-\infty}^{\infty} [\int\limits_{-\infty}^{\infty} A_x(k_x,k_y)dk_y]e^{-jk_x x}dk_x \qquad (4.11)$$

Combining eqn. (4.10) and (4.11) shows that

$$a_x(k_x) = \int_{-\infty}^{\infty} A_x(k_x,k_y)dk_y \tag{4.12}$$

Thus $a_x(k_x)$ indeed represents the projection of the 2-dimensional function $A_x(k_x,k_y)$ on the k_x-axis. So a 1-dimensional plane wave spectrum also provides interpretable information as to the 2-dimensional spectrum.

4.2.2 Heuristic approach

The plane-wave spectrum of the test-zone field reveals the directions and levels of reflections and leakage sources and thus can be used to improve the chamber. Besides this, the plane wave spectral analysis offers a powerful tool for correction of antenna measurements for the effects of field irregularities. PWS-analysis gives much insight in the response of an antenna to a non-plane wave. Bennett [7,24] demonstrated a 1-dimensional deconvolution processing method based on an heuristic analytical description of the antenna measurement problem. It states that the result of a measurement of the radiation pattern of an antenna under test, $F(\theta)$, will be the true antenna pattern, $A(\theta)$, convolved with the plane wave spectrum of the test zone, $S(\theta)$:

$$F(\theta) = A(\theta) * S(\theta) \tag{4.13}$$

This suggests that if the plane wave spectrum $S(\theta)$ can be deconvolved from the measurement, this will allow the effect of field irregularities to be removed from the measurement and hence allow the true antenna radiation pattern to be determined. A way to derive the plane wave spectrum $S(\theta)$ is by probing the test-zone field using a small probe with a known far field response, $P(\theta)$. Phase and amplitude data are recorded at half-wavelength intervals over a linear region. The set of data, $D(\theta)$, recorded is then

$$D(\theta) = P(\theta) * S(\theta) \tag{4.14}$$

Eqn. (4.14) can be used to deduce $S(\theta)$ because $P(\theta)$ and $D(\theta)$ are known. Now by deconvolution $S(\theta)$ can be used to extract $A(\theta)$ from $F(\theta)$ in eqn. (4.13), thereby removing field irregularities.

The following relations (4.15), (4.16), (4.17) will improve the comprehensibility. If the unwanted contribution to the radiation pattern is called $U(\theta)$, then

$$U(\theta) = A(\theta) * F[r(x)] \tag{4.15}$$

where r(x) is the field irregularity in the test zone, see eqn. (4.9). Now the true radiation pattern is given by

$$A(\theta) * F[s(x)-r(x)]=A(\theta) * F[1]=A(\theta) * \delta(\theta)=A(\theta) \tag{4.16}$$

where s(x) is the wavefront in the test zone, see eqn. (4.8).
Summation of eqn. (4.15) and (4.16) shows:

$$F(\theta)=A(\theta)+U(\theta) \tag{4.17}$$

The technique based on the equations (4.13) and (4.14) not only suppresses environmental effects, but can inherently provide a near-field/far-field transformation. In [24] an example is provided for a separation between source and test antenna of $0.15D^2/\lambda$ and it is illustrated that the near-field is equivalent to distributed point sources in the far-field.

The heuristic analytical description of the antenna test problem of Bennett [7,24] provides a good insight in the response of an antenna to a non-plane wave. In [7] the term residuals is introduced to describe the unwanted spectral components. Residuals can be used to examine the errors to be expected in a pattern measurement on the far field range, the compact range and the NF/FF-method as described in section 3.3 I.

Far-field range
Measurement of an antenna at a finite distance on a far field range introduces errors in the radiation pattern due to the spherical wavefront. The spherical wavefront can be analytically decomposed into a plane wave spectrum. The predominant effect of the residuals at these ranges is the filling in of the nulls near the mainlobe. As expressed by eqn. (4.13) the measurement of a sidelobe for example is the response derived from a summation of the PWS weighted by the true antenna pattern. Two dominant contributions occur as shown by eqn. (4.17). One is from the sidelobe being measured, eqn. (4.16), and the other from the residual distribution which is weighted by the antenna pattern, see eqn. (4.15). In general it is the mainlobe of the antenna pattern which plays the dominant role in corrupting the pattern measurement via the residual source distribution. In [7] it is demonstrated that when measuring the response at null n, the antenna mainlobe is directed towards residual source n at angle $SIN\theta= \frac{n\lambda}{P}$ and the zeroes of the antenna pattern are directed towards the remaining residual sources and the main source. Consequently the field amplitude recorded for the null position will be a value corresponding to the level of residual n. In general as sidelobes are measured out to larger angles the mainlobe moves further into a region of decreasing residuals. So its effect becomes much less significant and the measurement becomes

increasingly more accurate. The filling in of nulls, especially near the mainlobe, is illustrated in figure 4.4.
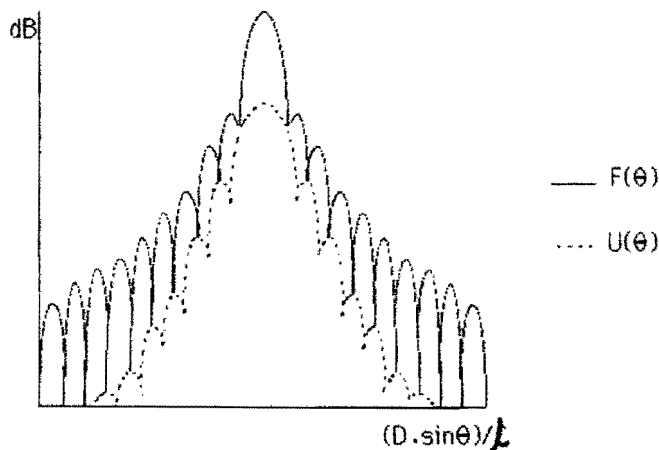
Figure 4.4 *Radiation pattern and residual contribution.*

In summary, the effect of measuring on a conventional far field range are that the close-in nulls become filled due to the presence of the distributed residual source distribution. The peak levels of sidelobes at wider angles are relatively unaffected. This is in accordance with practical experience.

Compact range
In compact ranges a predominant field irregularity is taper at the edges of the test zone. The figures 4.5, 4.6, 4.7, reprinted from [7], demonstrate three different types of compact range distributions.
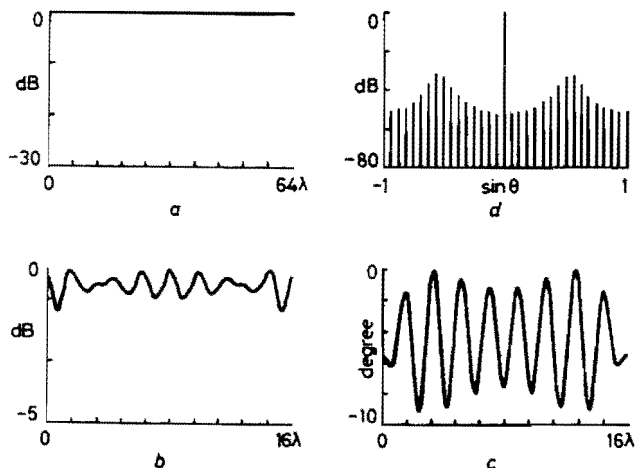
Fig. 4.5 *Simulated compact range with uniform illumination distribution*
a Effective aperture distribution
b Wavefront amplitude at 50λ
c Wavefront phase at 50λ
d Equivalent far-field source distribution
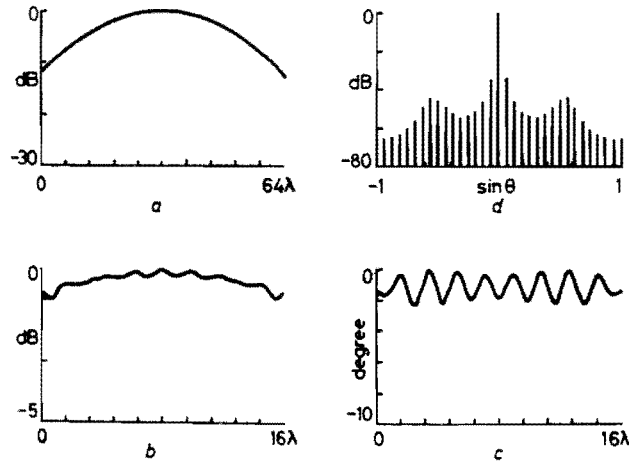
Fig. 4.6 *Simulated compact range with 12 dB tapered Gaussian illumination distribution*

a Effective aperture distribution
b Wavefront amplitude at 50λ
c Wavefront phase at 50λ
d Equivalent far-field source distribution
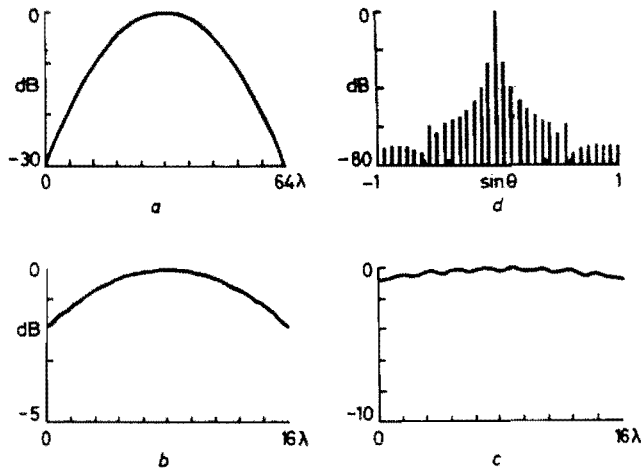
Fig. 4.7 *Simulated compact range with 30 dB tapered Gaussian illumination distribution*

a Effective aperture distribution
b Wavefront amplitude at 50λ
c Wavefront phase at 50λ
d Equivalent far-field source distribution

For the case of the uniform distribution shown in figure 4.5 the high edge illumination has caused severe amplitude and phase ripple in the test zone. As a result of the edge discontinuity two extra peaks occur in the PWS. The introduction of a -12 dB Gaussian taper in figure 4.6 results in a reduction of these peaks, but cause the appearance of residuals close to the main plane wave. Increasing the taper to -30 dB in figure 4.7 further reduces the two peaks, but gives rise to larger residuals near the main source. This means that especially the near-in sidelobes are affected during an antenna measurement on a heavily tapered compact range, as already described in section 3.3 I.

<u>NF/FF-method</u>
Measurements that are processed by means of a NF/FF transformation show a very low residual contribution, since the synthesized plane wave will theoretically be perfect, see section 4.5.

4.2.3 Analytical explanation

The description in the previous section is oversimplified. A complete treatment of this subject is found in [26]. However we will highlight the measurement of an high-gain antenna.

Application of the well-known Lorentz theorem to the coupling of an antenna with a non-planar wave results in eqn. (4.18), under the condition that multiple scattering between the AUT and the range antenna is negligible. Eqn. (4.18) is an expression for the measured voltage v:

$$v = \int\int_S (\vec{E}_a \times \vec{H}_b - \vec{E}_b \times \vec{H}_a) \cdot \vec{n} ds \tag{4.18}$$

where $\vec{E}_a$ and $\vec{H}_a$ represent the fields due to the range antenna, $\vec{E}_b$ and $\vec{H}_b$ represent the fields due to the AUT, S is the infinite integration surface parallel to the test zone area and $\vec{n}$ is the unit surface-normal on S. The fields $\vec{E}_a$, $\vec{H}_a$, $\vec{E}_b$, $\vec{H}_b$ can be expressed in terms of their plane wave spectra as shown by eqn. (4.2). This is used to derive an expression in [26] for the coupling of a high-gain antenna with a nearly plane wave:

$$v(k_{xr},k_{yr}) = \int_{-\infty}^{\infty}\int_{-\infty}^{\infty} [A_x(k_x,k_y)v_{co}(k_{xr}+k_x,k_{yr}-k_y) +$$
$$A_y(k_x,k_y)v_{cr}(k_{xr}+k_x,k_{yr}-k_y)]e^{-j(k_x x_0 + k_y y_0)}dk_x dk_y \tag{4.19}$$

The integral represents the measured signal $v(k_{xr},k_{yr})$, where:
* x_0 and y_0 are the position coordinates of the AUT in a plane parallel to S
* $A_x(k_x,k_y)$ and $A_y(k_x,k_y)$ are the spectra of the x- and y-polarized incident fields
* $v_{co}(k_{xr},k_{yr})$ and $v_{cr}(k_{xr},k_{yr})$ are the measured signals due to respectively an x- and y-polarized incident plane wave

The assumptions made during the various steps leading to relation (4.19) are:
* high-gain test antenna
* small angle approximation
* pure rotation of the test antenna

If we assume that co- and cross-polarization correspond to respectively the x- and y-direction then v_{co} and v_{cr} can be identified as respectively the co- and cross-polarization far-field functions. Two measurements are required to measure the co- and cross-polar patterns.

Measurement 1, main polarization in x-direction:

$$A_x(k_x,k_y)=\delta(k_x,k_y)+R_{x1}(k_x,k_y)$$
$$A_y(k_x,k_y)=R_{y1}(k_x,k_y)$$

(4.20)

Measurement 2, main polarization in y-direction:

$$A_x(k_x,k_y)=R_{x2}(k_x,k_y)$$
$$A_y(k_x,k_y)=\delta(k_x,k_y)+R_{y2}(k_x,k_y)$$

(4.21)

where $R_{x1}, R_{y1}, R_{x2}, R_{y2}$ represent deviations from the ideal x- and y-polarized incident wave spectra, also referred to as residuals.

The measured far-field signals $v_1(k_{xr},k_{yr})$ and $v_2(k_{xr},k_{yr})$, which are obtained by the two measurements mentioned in eqn. (4.20) and (4.21), can be represented by the following equations:

$$v_1(k_{xr},k_{yr})=v_{co}(k_{xr},k_{yr})+\int_{-\infty}^{\infty}\int_{-\infty}^{\infty}[R_{x1}(k_x,k_y)v_{co}(k_{xr}+k_x,k_{yr}-k_y)+$$

$$R_{y1}(k_x,k_y)v_{cr}(k_{xr}+k_x,k_{yr}-k_y)]e^{-j(k_xx_0+k_yy_0)}dk_xdk_y$$

(4.22)

$$v_2(k_{xr},k_{yr})=v_{cr}(k_{xr},k_{yr})+\int_{-\infty}^{\infty}\int_{-\infty}^{\infty}[R_{x2}(k_x,k_y)v_{co}(k_{xr}+k_x,k_{yr}-k_y)+$$

$$R_{y2}(k_x,k_y)v_{cr}(k_{xr}+k_x,k_{yr}-k_y)]e^{-j(k_xx_0+k_yy_0)}dk_xdk_y$$

When all the error contributions due to the error spectra $R_{x1}, R_{y1}, R_{x2}, R_{y2}$ of the test zone field are negligible, then eqn. (4.22) shows that the measured far-field patterns v_1 and v_2 indeed correspond to respectively the co- and crosspolar pattern of the AUT. Here R_{x1} and R_{x2} are the co-polarized residuals while R_{y1} and R_{y2} are the cross-polarized residuals. In practice the cross-polarized residuals R_{y1} and R_{y2} are negligible and the cross-polarized far-field v_{cr} is much smaller than the co-polarized far-field v_{co}. Eqn. (4.22) can be simplified to eqn. (4.23).

$$v_1(k_{xr},k_{yr})=v_{co}(k_{xr},k_{yr})+\int_{-\infty}^{\infty}\int_{-\infty}^{\infty} R_{x1}(k_x,k_y)v_{co}(k_{xr}+k_x,k_{yr}-k_y)e^{-j(k_xx_0+k_yy_0)}dk_xdk_y$$

$$v_2(k_{xr},k_{yr})=v_{cr}(k_{xr},k_{yr})+\int_{-\infty}^{\infty}\int_{-\infty}^{\infty} R_{x2}(k_x,k_y)v_{co}(k_{xr}+k_x,k_{yr}-k_y)e^{-j(k_xx_0+k_yy_0)}dk_xdk_y$$

(4.23)

Bennett's description of the antenna measurement problem [7,24] given in the previous section corresponds to the measurement of the co-polarized far-field v_1 in eqn. (4.23). Here the AUT is located at the origin $(x_0=0,y_0=0)$ and the cross-polar incident field spectral component $A_y(k_x,k_y)=0$. Eqn. (4.19) reduces to:

$$v(k_{xr},k_{yr})=\int_{-\infty}^{\infty}\int_{-\infty}^{\infty} A_x(k_x,k_y)v_{co}(k_{xr}+k_x,k_{yr}-k_y)dk_xdk_y$$

(4.24)

This 2-dimensional equation is comparable to the 1-dimensional eqn. (4.13) because they both express that the measured far-field is the true far-field convolved by the plane wave spectrum of the test zone field.

The heuristic analytical approach in section 4.2.2 doesn't apply to the measurement problem of the cross-polarized far-field pattern v_2 as shown in eqn. (4.23). For, this relation shows that the measured cross-polar far-field v_2 is composed of the true cross-polar far-field v_{cr} and the co-polar far-field v_{co} convolved by the co-polar residual R_{x2} in $(x_0=0,y_0=0)$.

The convolution in the spectral domain given by eqn. (4.24) can be rewritten to an inverse-Fourier integral of a multiplication in the space domain resulting in eqn. (4.25), for $F[A_1(k_x,k_y)*A_2(k_x,k_y)]=F[A_1(k_x,k_y)]\cdot F[A_2(k_x,k_y)]=E_1(x,y)\cdot E_2(x,y)$.

$$v(k_{xr},k_{yr})=-\frac{1}{4\pi^2}\int_{-\infty}^{\infty}\int_{-\infty}^{\infty} E_{ax}(x,y)e_{co}(-x,y)e^{j(-k_{xr}x+k_{yr}y)}dxdy$$

(4.25)

Here $E_{ax}(x,y)=eqn.(4.4)$ and:

$$e_{co}(x,y)=F[v_{co}(k_x,k_y)]=\int_{-\infty}^{\infty}\int_{-\infty}^{\infty} v_{co}(k_x,k_y)e^{-j(k_xx+k_yy)}dk_xdk_y$$

(4.26)

e_{co} and v_{co} are respectively the aperture field distribution and far-field distribution of the high-gain test antenna. The test-zone field distribution and the corresponding plane wave spectrum are given by respectively E_{ax} and A_x.

A special case illustrates the antenna measurement problem as one would expect. The AUT is a high-gain antenna with linear polarization in the x-direction. The antenna is being illuminated by an x-polarized plane wave. We expect the true co-polarized far

field to be measured. Substitution of the following field equations describing the plane wave in eqn. (4.24) or (4.25) confirms our proposition:

$$\begin{cases} E_{ax}(x,y) = 1 \\ E_{ay}(x,y) = 0 \end{cases} \quad or \quad \begin{cases} A_x(k_x,k_y) = \delta(k_x,k_y) \\ A_y(k_x,k_y) = 0 \end{cases} \qquad (4.27)$$

4.2.4 Advantages and disadvantages

Advantages:

* The PWS gives a good quantitative impression of the Compact Range performance.
* The technique corrects for all field irregularities including range amplitude and phase errors and errors due to the presence of extraneous fields.
* The technique can function as a NF/FF-transformation process.

Disadvantages:

* A 1- or 2-dimensional scan has to be performed first to characterize the test zone and then the assumption is made that the field doesn't change meanwhile between the antenna measurement.
* An increase of measurement and computation time.
* Mutual coupling not taken into account.

4.3 Range field compensation

4.3.1 The technique

The idea behind the technique of range field compensation resembles the technique of deconvolution. They both need a characterization of the test environment and then use this signature to remove unwanted effects from subsequent test antenna scans by some form of processing. The range field is measured over a spherical surface encompassing the test zone using a low gain probe with a known pattern. A spherical mode expansion of the measured range field is used in subsequent antenna measurements to compensate for the effects of extraneous fields. The range field is separated into two parts, the $\mu = \pm 1$ part and the $\mu \neq \pm 1$ part. The $\mu = \pm 1$ part of the range field is the sum of the range field spherical modes with a ϕ-dependence of $\cos\phi$ or $\sin\phi$. Range antennas in spherical far-field and near-field ranges create $\mu = \pm 1$ fields. The $\mu \neq \pm 1$ part of the range field is the sum of all the range field spherical modes with a ϕ-dependence that

is not given by $COS\phi$ or $SIN\phi$. Extraneous field sources create $\mu \neq \pm 1$ fields. The effect of the $\mu \neq \pm 1$ part cannot be compensated for efficiently using existing probe compensation. The basic idea behind range field compensation is to analytically reduce the effect of the $\mu \neq \pm 1$ part on the pattern. This can be done using the $\mu \neq \pm 1$ part and an estimate of the AUT pattern. The result after reduction is mostly the effect of the $\mu = \pm 1$ part if the range antenna field is the dominant field in the range. The effect of the $\mu = \pm 1$ part can be compensated for using existing probe compensation. The result is a better estimate of the AUT pattern which can be used to further reduce the effects of the $\mu \neq \pm 1$ part. Repeated iterations will result in an accurate depiction of the AUT pattern. A more precise description of this technique is found in [9].

4.3.2 Advantages and disadvantages

Advantages:
* Extraneous source detection possible.
* Very well applicable when spherical measurement equipment is already available.
* Good results without being limited in the amount of compensation it can provide.
* Using spherical mode expansion the test-zone field can be determined at any point on or inside the source free measurement sphere.

Disadvantages:
* Spherical probing requires extra equipment when normally other range positioners are applied such as a linear scanner.
* Spherical results have to be converted to linear results to get a meaningful display of the range-field amplitude and phase taper and ripple.
* A spherical scan has to be performed first to characterize the test zone and then the assumption is made that the range field doesn't change meanwhile for different AUT's
* A large sphere requires a lot of measurement and computation time.
* Mutual coupling not taken into account.

4.4 Pattern subtraction

4.4.1 The technique

The technique of pattern subtraction [10] is just like range field compensation based on a spherical mode expansion. In the first step, the test-zone field is measured with a probe moving over a spherical surface containing the test zone. From this measured field distribution, the location of the extraneous field sources can be determined. In the

second step the range reflections are used in an iterative procedure that, starting with the actual measured pattern, produces an error-free pattern with a few iterations.

The expression (4.18) that has been derived from the Lorentz theorem, can be used to find a relation between the measured and true radiation pattern of the AUT. In this case the surface S in eqn. (4.18) is a sphere that completely encloses the AUT. The fields radiated by the AUT are denoted by $\vec{E}_b$, $\vec{H}_b$ and the test-zone fields are denoted by $\vec{E}_a$, $\vec{H}_a$. These fields are expressed in spherical mode expansions to obtain a relation between the measured pattern $\vec{E}_m$ and the undistorted pattern $\vec{E}_b$ as shown in [10]:

$$\vec{E}_b(r_0,\theta,\phi)= \frac{1}{\vec{S}_0(\vec{r}_0)}[\vec{E}_m(r_0,\theta,\phi)-\sum_{n=1}^{N} \vec{S}_i(r_i,\theta_i,\phi_i)\cdot\vec{E}_m(r_i,\theta,\phi;\theta_i,\phi_i)] \qquad (4.28)$$

where the test-zone field is supposed to be created by a main spherical source $\vec{S}_0(\vec{r}_0)$ and a small number N of additional spherical sources $\vec{S}_i(\vec{r}_i)$, with $|\vec{S}_i| \ll |\vec{S}_0|$. Formula (4.28) is used in an iterative approach to obtain a practical error-free pattern.

4.4.2 Advantages and disadvantages

Advantages:
* Extraneous source detection is possible.
* Only a few iterations are necessary.
* Very well applicable when spherical measurement equipment is already available.

Disadvantages:
* Simulations seem well, but no experimental experience is available.
* Spherical probing requires extra equipment when normally other range positioners are applied such as a linear scanner.
* Spherical results have to be converted to linear results to get a meaningful display of the range-field amplitude and phase taper and ripple.
* Mutual coupling not taken into account.

4.5 Plane-wave synthesis

4.5.1 The technique

In chapter 2 attention has been paid to NF/FF-methods to predict the antenna far-field pattern from measurements in the near-field. An alternative approach for the NF/FF-methods is the plane-wave synthesis technique [16]. The idea is to generate a plane

wave in the test zone by means of an array of radiators as illustrated in figure 4.8a.
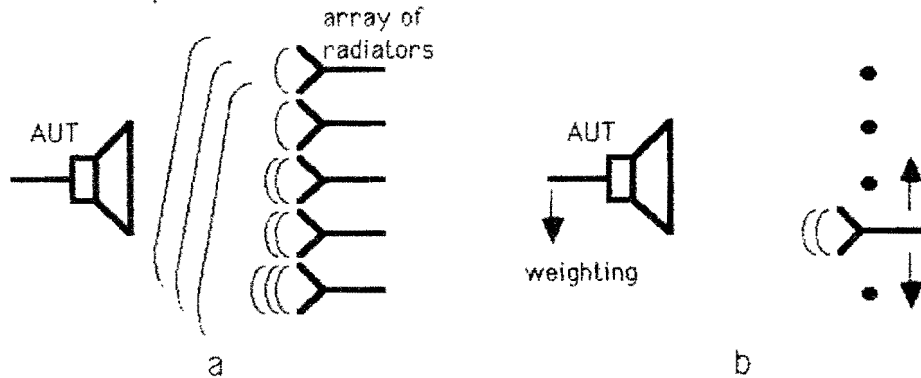
Figure 4.8   *Plane-wave synthesis.*
a) Principle
b) Implementation

More preferable is a single-scanning probe as shown in figure 4.8b, which is fed with appropriate excitation coefficient so that the array is synthesized. Instead of using a variably fed probe a unit probe can be substituted and the antenna response is subsequently multiplied by the appropriate weighting coefficient. After this the actual radiation pattern can be computed by summing these responses multiplied by the weighting function. This method to synthesize a plane wave might also be seen as a 'computer generated compact range'. An extension to this technique is a combination of a planar probe scan and antenna positioner scan. Its purpose is more versatility and flexibility in controlling the extent and the direction of the plane wave flow at the antenna, and the production of negligibly low-field regions in the environment. Fundamentally, the reason that errors of spatial origin cannot be segregated from the pattern data is because a fixed probe is used which has only one view of the environment. The probe-scan/antenna-scan method is able to distinguish "noise of spatial origin" [11,27]. The method of generating synthesized array functions consists in propagating backwards towards the probe the desired field distribution at the antenna. The situation is illustrated in figure 4.9, where the surface S represents the array and the surface Σ represents the AUT.
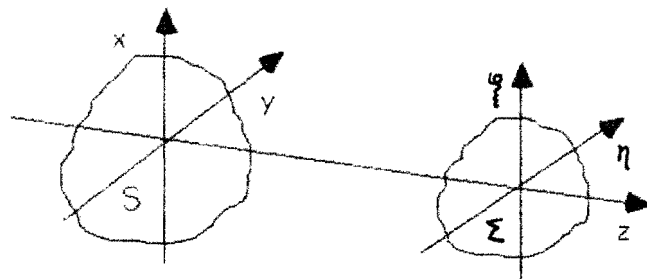
Figure 4.9   *Schematic configuration.*

The operation may be carried out using the Rayleigh-Sommerfeld diffraction formula for scalar fields.

$$g(x,y,z) = -\frac{j}{\lambda} \int\int_{\Sigma} E(\zeta,\eta)\frac{e^{-jkr}}{r}COS(\overline{n \cdot r})ds \tag{4.29}$$

where
* $g(x,y,z)=$ field at any general point on S
* $\overline{r}=$ position vector pointing from a general point on S to a general point on Σ
* $\overline{n}=$ normal to Σ

Conversely the field at Σ can be determined from the field distribution over S so that

$$E(\zeta,\eta) = \frac{j}{\lambda} \int\int_{S} g(x,y,z)\frac{e^{jkr}}{r}COS(\overline{n \cdot r})ds \tag{4.30}$$

Ideally the desired field distribution $E(\zeta,\eta)$ at the antenna should have uniform field-amplitude and -phase on the surface Σ and should be zero elsewhere. Physically this distribution cannot be obtained, for the array is finite. Since the similarity of this requirement with a bandpass filter problem is apparent it is appropriate to use a Butterworth type of distribution. This distribution can be applied in eqn. (4.29) for the determination of the weighting function g(x,y). Next the real field distribution resulting from g(x,y) is obtained by eqn. (4.30). It will have some ripple that results from the edges of the Butterworth distribution.

The overall response of the AUT is the sum of its response to each probe position after suitable weighting by the predetermined array function. The prediction process may therefore be expressed as follows:

$$P(\theta_{FF},\phi_{FF}) = \sum_{n=1}^{N} \sum_{m=1}^{M} g(m\Delta x, n\Delta y) f(m\Delta x, n\Delta y) \tag{4.31}$$

where $P(\theta_{FF},\phi_{FF})$ is the predicted value of the far-field pattern in the angular direction (θ_{FF},ϕ_{FF}), $f(m\Delta x, n\Delta y)$ is the antenna response to the field radiated by the probe located at the point $(m\Delta x, n\Delta y)$ and $g(m\Delta x, n\Delta y)$ is the function at the point $(m\Delta x, n\Delta y)$.

In summary the PSAS-technique has additional degrees of freedom over the original planar scan method. These are the combination of the antenna scan with the probe scan, together with the especially configured weighting function, producing a more effective flow of energy at the test antenna leading to more environment suppressive predictions over all space [27].

4.5.2 Advantages and disadvantages

Advantages:
* The spatially concentrated wavefront avoids partly the illumination of unwanted scatterers.

Disadvantages:
* Increased data requirement, measurement time and computation time due to the PSAS-technique (double scanning).
* The inevitable ripple in both amplitude and phase still introduces errors.
* The experimental results of this method are not very accurate.
* Mutual coupling not taken into account.

4.6 Non-plane-wave synthesis

4.6.1 The technique

By means of plane-wave synthesis it is possible to produce an effective flow of energy with appropriate amplitude and phase to the test antenna, but with very low field strength elsewhere, see section 4.5. However a non-plane wave, synthesized from a more tapered weighting function, even more efficiently suppresses environmental effects [12]. Figure 4.10 schematically shows the configuration of the situation to be analyzed.
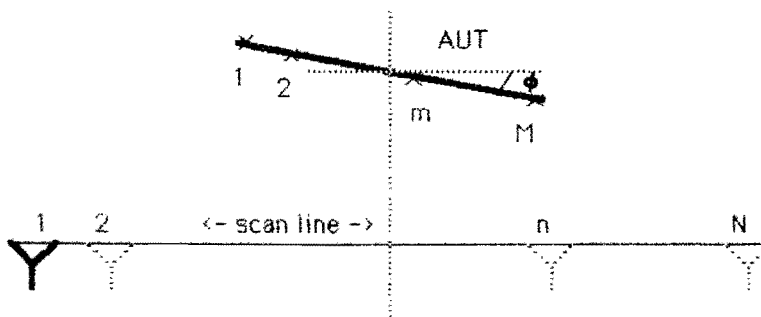
Figure 4.10 Schematic of the test setup.

For each angle ϕ of the AUT, the probe samples the radiated field along the scan-line. Let A_m denote the excitation coefficient at the m'th point of the AUT; $[W_n]$ a weighting function used on the scan-line during data processing, B_m the field at the m'th point on the aperture of the AUT produced by the weighting function $[W_n]$, and S_n the response of the AUT to the wavefront transmitted by the probe at the n'th position of the scan-line. For a given ϕ, it can be shown [12] that

$$\sum_{}^{M} A_m \cdot B_m = \sum_{}^{N} W_n \cdot S_n \qquad (4.32)$$

If the weighting function produces a plane wave (so that B_m is uniform), then eqn. (4.32) shows that the summation of the measured data weighted by the weighting function, $\sum^N W_n \cdot S_n$, is itself the predicted far-field value belonging to the angle ϕ. For non-plane-wave synthesis the summation is not the required far-field value. Since both B_m and S_n are functions of ϕ a second subscript can be introduced to denote this. For M different values of ϕ the following set of complex linear equations can be established.

$$\left\{ \begin{array}{l} \sum_{}^{M} A_m \cdot B_{m,1} = \sum_{}^{N} W_n \cdot S_{n,1} \\[2ex] \sum_{}^{M} A_m \cdot B_{m,2} = \sum_{}^{N} W_n \cdot S_{n,2} \\[2ex] \qquad \cdot \\[-1ex] \qquad \cdot \\[2ex] \sum_{}^{M} A_m \cdot B_{m,M} = \sum_{}^{N} W_n \cdot S_{n,M} \end{array} \right. \qquad (4.33)$$

Clearly A_m can be solved and hence the predicted far-field pattern of the AUT is obtained. According to this theory it would be possible to create a 'computer anechoic chamber' provided that a proper weighting function has been found.

4.6.2 Advantages and disadvantages

Advantages:
* In theory NPWAS provides a more powerful capability for suppressing environmental effects by using a weighting function that doesn't produce a plane wave. In this way the energy-flow can be more confined to the test antenna's aperture, avoiding the illumination of unwanted scatterers.

Disadvantages:
* No experimental verifications available.
* Mutual coupling not taken into account.

4.7 Time-gating

4.7.1 The technique

The principal of time-gated antenna measurements is differentiation of signals by time-of-arrival. As illustrated in figure 3.1 extraneous signals travel another path as the direct signal coming from the range antenna. This means that these unwanted signals can potentially be removed by time-gating.

One way to perform time-gated measurements is sending a pulse-modulated waveform. Figure 4.11 shows a typical response of the AUT in time domain.
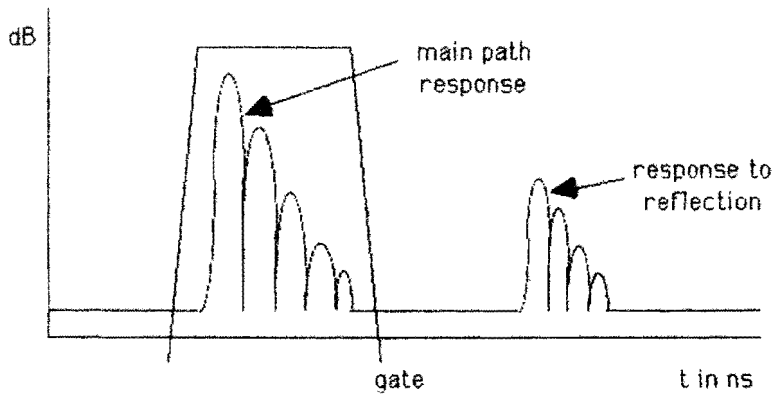
Figure 4.11   Impulse response.

Placing an appropriate time filter, the gate, around the main path response, removes the effects of responses outside this gate. All of these functions for pulse excitation and gating in time-domain can be accomplished by specialized hardware [13]. However this is quite expensive. A cheaper method is time-gating based on pulse compression using swept frequency techniques to overcome the problems of producing and detecting short pulses and the attendant loss in signal-to-noise ratio. The HP8510 network analyzer is capable of using pulse compression software. The software operates by sweeping the frequency source over a bandwidth and reading the receiver. The swept frequency receiver measurements are compressed into an equivalent pulse response by Fourier transform techniques. The pulse response can be analyzed to determine the location of reflections, or gated to eliminate the reflections.

The required frequency span and the number of frequency steps can be determined from basic radar concepts [28]. The path-length resolution, R_r, is a direct function of the frequency span, F_s:

$$R_r = \frac{c}{F_s} \tag{4.34}$$

where c= propagation velocity.

The number of frequency steps, n, determines the alias-free path-length, R_a. The division by two is to convert the total unaliased path-length into the allowable path-length differential:

$$R_a = \frac{n \cdot R_r}{2} \qquad (4.35)$$

The geometry of the test range plays an important role in the ability to use time domain to remove extraneous signals. In addition, antenna bandwidth is also an important parameter in determining whether time gating can be used on the test range. The wider the measurement bandwidth, the narrower will be the impulse width. To be able to apply gating in antenna measurements the difference between the main path and the extraneous path must be greater than the main-path impulse response of the antenna to allow both responses to be resolved. This means it is the duration of the antenna impulse response that determines whether gating is effective, for no overlap may occur between the response to the direct signal and the extraneous signal. The impulse response of the antenna is often determined by the multiple paths in the antenna itself. For example a parabolic reflector antenna will have internal reflections between the feed and the reflector. This is an antenna property and its response must not be removed by time-gating. From the above we may conclude that the window to be applied for time-gating may not be to large or to small. However extraneous signals travelling approximately the same path-length as the direct signal cannot be removed.

4.7.2 Advantages and disadvantages

Advantages:
* When sufficient bandwidth and frequencies are available wide-angle incident fields and mutual coupling are removed reliably.
* Improvement of the signal-to-noise ratio due to processing advantage.

Disadvantages:
* Not applicable when only small bandwidth is available.
* Need for expensive hardware and software.
* Reflections having approximately the same path-length as the direct signal can't be distinguished.
* Software gating implies increased measurement time due to frequency sweeping.

Chapter 5

Novel APC-methods

5.1 Introduction

Several methods have been developed recently in order to correct antenna pattern measurements for the presence of extraneous fields. These were presented in chapter 4. None of them is perfect and the only one frequently used is time-gating. To overcome the problems accompanying time-gating a new technique has been developed. It has been called "novel APC-methods" because the way measurements are performed is exactly the same as in "Antenna Pattern Comparison"-measurements, see section 3.2.1. It consists of making pattern cuts on a few positions in the test zone. In the classic APC-method, the recorded amplitude variations indicate the presence of extraneous signals disturbing the measurements. In the "novel APC-methods" both amplitude- and phase-data are used to correct pattern measurements for environmental effects and mutual coupling. The aim of this chapter is to present the new technique. The theory is explained first. Then the implementation inclusive the algorithm for processing the measurement data is outlined. For verification purposes extensive measurements have been performed under different conditions. Part of the experiments is an investigation to error sources. The results will be presented here. Finally a discussion follows with a comparison between the "novel APC-methods" and time-gating.

5.2 Theory

A fast and simple way to recognize problems in antenna pattern measurements provides the APC-method. The deviations in the amplitude data of the radiation pattern give an indication for the magnitude of the interfering signal and reflectivity levels can be calculated. On the other hand, for accurate reflectivity level determination a considerable number of measurement positions are necessary. The "novel APC-

47

methods" employ both amplitude- and phase-data to provide a means for correction of the measured pattern. This way only three different measurement positions are sufficient. A comparison between conventional and novel APC is given in figure 5.0.
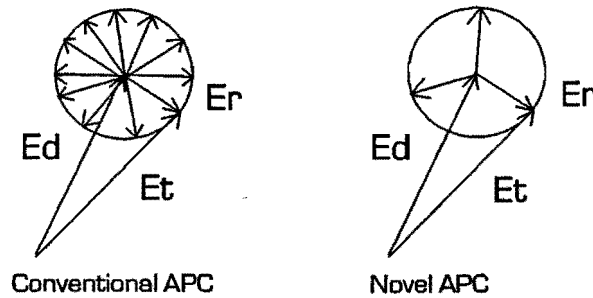
Figure 5.0   Comparison between conventional and novel APC.

The "novel APC-methods" are based on the property that the phase-relation between the direct signal E_d and the extraneous signal E_r changes along a certain trajectory. This is easily seen from a geometrical point of view, figure 5.1.
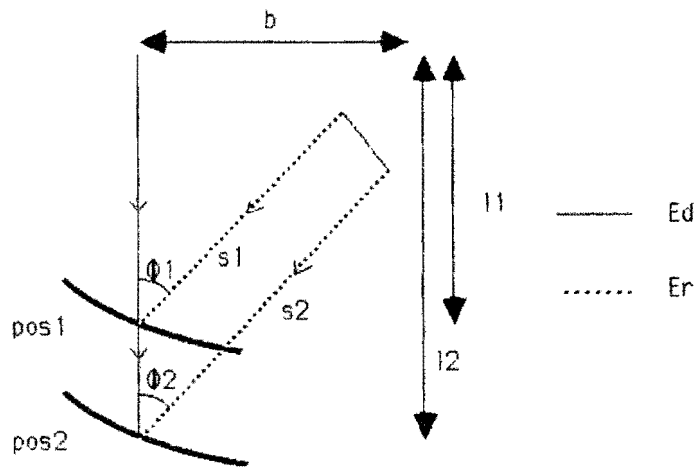
Figure 5.1   Different change in phase of E_d and E_r.

In figure 5.1 the assumption is made that only one extraneous source is present and that both incident fields behave like plane-waves. From eqn. (4.1) it is seen that the change in phase of a plane wave is proportional to the covered distance. Now referring to figure 5.1, the phase-shift of E_d and E_r is proportional to respectively l_2-l_1 and s_2-s_1. This means that the phase of E_r relative to E_d will change between the positions 1 and 2. So it must be possible to separate two interfering signals from pattern data belonging to different positions. However in the practical situation with arbitrary incident fields the distance between the two positions must be kept small enough so that E_r will not change in amplitude.

The question is how to make corrections for an extraneous field on this principle. The answer is easy if we refer to figure 5.2.
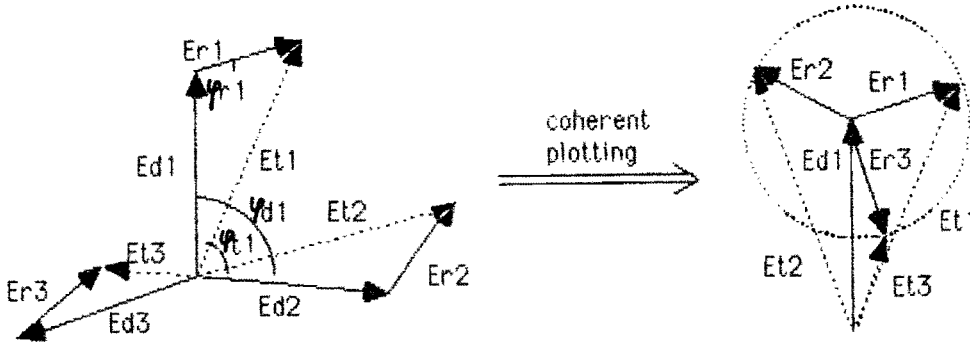
Figure 5.2 *Vector representation of correction process.*

In the plot left the results of measurements made on three different positions are depicted. Each measured vector, E_{t1}, E_{t2}, and E_{t3}, can be thought to be composed of two vectors representing the direct and the extraneous signal. Expressing these relations in formula:

$$E_{tx} \cdot \sin\varphi_{tx} = E_{dx} \cdot \sin\varphi_{dx} + E_{rx} \cdot \sin\varphi_{rx}$$
$$E_{tx} \cdot \cos\varphi_{tx} = E_{dx} \cdot \cos\varphi_{dx} + E_{rx} \cdot \cos\varphi_{rx}$$

(5.1)

where:
* $x = 1,2,...$ for position $1,2,...$
* E_{tx} and φ_{tx} are the measured amplitude and phase on position x
* E_{dx} and φ_{dx} are the unknown amplitude and phase of the direct signal on position x
* E_{rx} and φ_{rx} are the unknown amplitude and phase of the extraneous signal on position x

A single measurement delivers a set of 2 equations and 4 unknown variables. Going on this way it is seen that n measurements deliver 2n equations and 2n+2 unknown variables. However calculating the phase-shift of E_d between positions brings a solution to this problem. Then it is possible to express φ_{dx} for instance as:

$$\varphi_{dx} = \varphi_{d1} + \Delta\varphi_{1,x}$$

(5.2)

where $\Delta\varphi_{1,x}$ is the phase-shift of the direct signal between position 1 and x. An exact knowledge of the distance between position 1 and x is the only requirement. Three measurements are sufficient for a solution with a combination of the equations (5.1) and (5.2).

Figure 5.2 shows the same solution by coherently plotting the measurements. Coherently plotting is achieved by phase-shifting the measurements 2 and 3 proportional to the distance between position 1 and 2 resp. 1 and 3. As a result every measurement vector will end on a circle. The vector E_{d1}, ending on the circle centre is the corrected measurement on position 1 and the vector E_{r1} is the extraneous signal that disturbs the measurement on position 1. In this case the first position is taken as reference plane, but in principle every position could have been taken as reference plane.

It is concluded that measurements can be corrected for a single disturbing component. When more components are present the interference pattern becomes very complicated. Then it is impossible to perform corrections because even with a lot of measurements the number of unknown variables never equals the number of equations. In CATR's several extraneous fields are incident upon the AUT. Therefore the "novel APC-methods" can't be applied for correcting measurements on omnidirectional antennas. The success of the new technique depends on the directivity of the AUT to distinguish disturbing components. In other words the antenna must act as some kind of a spatial filter. The "novel APC-methods" are especially appropriate for high-gain antennas. And it is just this group of low-sidelobe antennas that suffer the most from disturbing signals.

5.3 Implementation

In the implementation several steps can be distinguished. In the first place it is necessary to accurately determine the distance between two positions of the antenna. Further it will seem that due to extra complications the removal of mutual coupling from the measurements differs from the removal of extraneous fields. Therefore two different "novel APC-methods" have been developed.

5.3.1 Accurate distance determination

In section 5.2 the principle of the "novel APC-methods" has been explained. It is clear that an accurate determination of the distance between the positions where pattern cuts have been made is inevitable. The accuracy of the measured length should be at least in the order equivalent to $\pm 1°$ in phase. So the higher the frequency, the more stringent becomes the accuracy of the distance. For instance at 11.5 GHz an uncertainty of $\pm 1°$ in phase corresponds to an accuracy of $\pm 0,07mm$ in length.

Four options are available:

1) Buying a high-precision measurement system based on digital or optical principles. However this would raise costs.

2) Employing a cheaper method to physically measure the distance. An attempt has been made to produce iron measuring-staffs. These measuring staffs have been gauged and expansion due to temperature was taken into account. However it was impossible to achieve the accuracy requirements, because small dents in the metal arose after use.

3) Avoiding the need for distance determination. To understand this one must be familiar with the way antenna measurements are performed. For it is possible to take calibrated or uncalibrated pattern cuts. In case the pattern cut is uncalibrated, the measured levels will be relative to the standard gain horn. However calibration means that the radiation pattern will be measured relative to the boresight signal of the antenna. Consequently a calibrated pattern will have its boresight amplitude and phase normalized to resp. 0 dB and 0°. Performing calibrated pattern cuts on different positions offers an accurate feature to avoid distance measurements if disturbances were absent on the boresight signal. The effect is comparable to coherent plotting as illustrated in figure 5.2. But in practice the boresight signal is affected by mutual coupling so that variations occur in distance. Therefore no stable reference signal is available to uniformly normalize each pattern. The corresponding inaccuracy in distance has its largest impact on the removal of mutual coupling itself.

4) Calculating the distance from boresight phase-data that has been corrected for mutual coupling. This is preferable over the previous methods, for no extra equipment is necessary, the influence of mutual coupling is removed and the accuracy requirement of ±1° will always be achieved independent of the frequency. The method behaves well as compact ranges produce very low phase-taper in the test zone. Yet another benefit of relying on phase-data is that the movement of the AUT doesn't necessarily have to be perpendicular to the plane-wavefront of the range field. In figure 5.3 the rail system carrying the antenna support is oblique to the incident field.
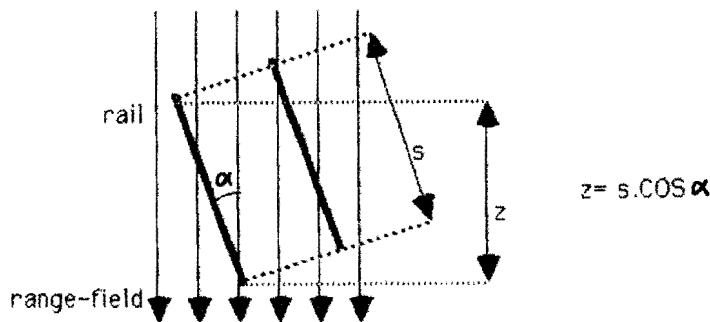
Figure 5.3 Rail oblique to incident field.

It is observed that the displacement along the rail s is not suitable to calculate the phase-shift of E_d unless $\alpha = 0°$. In general the phase-shift of E_d will be proportional to $z = s\cos\alpha$. So one should be careful in applying method 1 or 2 when there is uncertainty about the position of the rail relative to the incident field.

The procedure to calculate the displacement z in the field from phase-data is as follows. First the phase-error in the measured signal on boresight must be eliminated. The boresight signal of high-gain antennas is mostly influenced by mutual coupling. For the antenna is less sensitive to radiation from the outer directions due to its directivity. Further most reradiated energy from the AUT to the range antenna is confined to a small angular region resulting in an increased mutual coupling. Figure 5.4 depicts the situation.
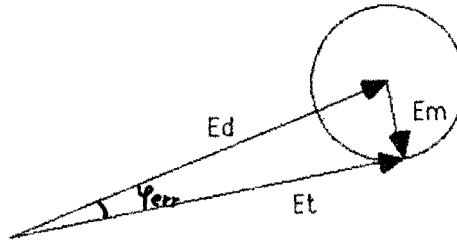
Figure 5.4 Interference between the direct signal and mutual coupling.

The phase-error is equivalent to φ_{err} and is determined when E_d and E_m are known. But with the AUT on an arbitrary position we don't know anything about the mutual coupling. Therefore an extra measurement is introduced preceding the actual pattern cuts. The measurement simply consists of recording the interference pattern in the boresight direction along the rail. In figure 5.5 the result of such a measurement is shown.
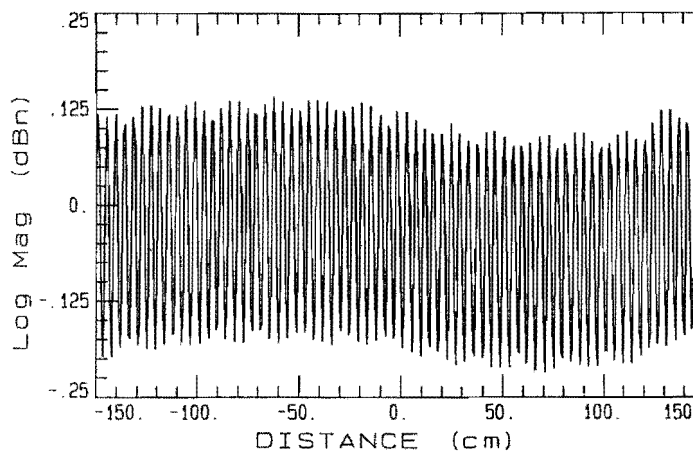
Figure 5.5 Longitudinal scan (2m parabola, 11.5 GHz, H-plane).
(1cm on plot= 3mm in reality)

Mutual coupling causes a ripple in amplitude (E_m) and phase with a period of $\lambda/2$. At 11.5 GHz is $\lambda \simeq 26mm$ so that the ripple period $\simeq 13mm$, see figure 5.5. Experiments on error sources in section 5.4.1 show that the ripple in amplitude is quite stable, but the phase may suffer from phase noise. Therefore locking on amplitude is applied to determine φ_{err}. E_d and E_m are easily derived from figure 5.5 as resp. the mean value and amplitude of the ripple. Substituting these values together with the measured boresight amplitude E_t from a pattern cut on a particular position in eqn. (5.3) gives the phase-error:

$$\varphi_{err} = ARCCOS \frac{E_d^2 + E_t^2 - E_m^2}{2 E_d E_t} \qquad (5.3)$$

This equation for the magnitude of φ_{err} has been derived from the vector diagram in figure 5.4. Still the sign of φ_{err} is unknown. A useful tool is slope detection. A rough estimation of the position, by using a ruler, gives adequate information to detect whether E_t belongs to a raising or a falling slope of the ripple. On raising or falling slopes the phase-error should be subtracted resp. added to the measured phase to obtain the true phase. This rule holds in case the AUT is moved backwards for then the rotation of the vector E_m is clockwise, see figure 5.4. Now we are ready to calculate the exact distance between two positions. The rough estimation indicates the distance with an accuracy of a single wavelength. The accuracy is further improved within this period be means of the corrected phase-data. Thus the exact position is calculated according to eqn. (5.4).

$$exact\ distance = (number\ of\ \lambda's + \frac{phase\text{-}shift}{2\pi}) * \lambda \qquad (5.4)$$

where:

* *"number of $\lambda's$"* is determined from the rough estimation and rounding off down to an integer value
* "phase-shift" is the relative difference in the corrected phase between two positions

In table 5.1 it is demonstrated that compensation for the phase-ripple caused by mutual coupling indeed improves the accuracy in distance determination. The measurement has been performed with a 1.2m parabola on boresight, in the E-plane for f= 11.5 GHz. As a reference the distance was measured with a marking gauge. The improvement in accuracy is obvious when the second and third columns are compared with the first one.

distance measured with marking gauge	distance calculated without compensation for mutual coupling	distance calculated with compensation for mutual coupling
0.00	0.00	0.00
2.33	2.28	2.33
4.94	5.03	4.95
7.36	7.58	7.39
9.98	10.20	10.01
12.38	12.48	12.45

Table 5.1 The positive effect of compensating phase-data for mutual coupling.

Summarizing all ingredients for application of method 4:

a) longitudinal scan-data with antenna on boresight

b) pattern cuts on different positions, including the boresight

c) rough estimations of the distance between the positions

In method 3 and 4 the boresight signal is used for distance determination. Normally this will be the strongest signal available and so is the less affected by noise. A further reduction of the influence of especially phase-noise is achieved by averaging the calculated distances for all frequencies that were measured.

5.3.2 Extraneous fields

The extraneous fields cause errors in the measured sidelobe levels. The impact on the mainlobe of high-gain antennas is negligible for two reasons:

* The signal levels belonging to the mainlobe are much higher than the levels of the extraneous signals, especially if the latter are incident upon the low-sidelobes.

* During the measurement of the mainlobe the antenna boresight is directly pointing towards the flat surface of the main reflector where no sources of extraneous fields exist.

A high-gain antenna is most sensitive to an incident field in the same direction as the antenna boresight. If we consider the incident field to be a plane wave, a simple relation can be derived for the interference periods in transversal and longitudinal directions, see eqns. (3.7) and (3.8). Based on eqn. (3.8) a utility program has been written with the name "Distance". The aim of the program is to generate a table that can be used for the development of a measurement procedure. For each azimuth angle the next items are calculated:

1) At which part of the room is pointing the antenna boresight. For this a simulation model of the range has been developed.

2) Period of the interference pattern in longitudinal direction according to

$$P = \frac{\lambda}{1 - COS\alpha} \tag{5.5}$$

3) The maximal movement along the rail to keep the change in view-angle within the required value. This is demonstrated in figure 5.6.
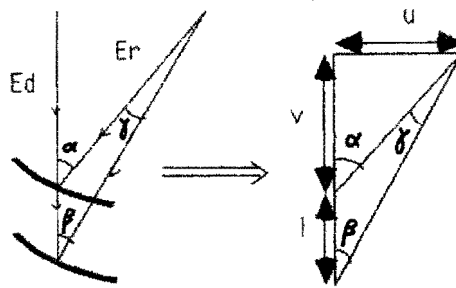
Figure 5.6 *Change in view-angle between positions.*

The maximal allowable distance between the two positions to keep γ small can be calculated using eqn. 5.6.

$$l = \frac{u}{TAN(\alpha - \gamma)} - v \tag{5.6}$$

Here u and v are determined by range-dimensions.

4) The resulting phase-shift of E_r relative to E_d. The formula used is:

$$phase\text{-}shift = \frac{l}{P} * 360° \tag{5.7}$$

5) The perpendicular shift in the antenna boresight as a result of the distance l. This is demonstrated in figure 5.7.
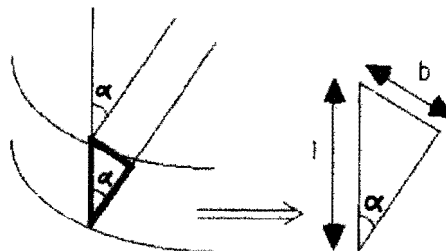
Figure 5.7 *Shift in boresight between positions.*

The shift in boresight expressed in wavelengths is calculated from eqn. (5.8).

$$b = \frac{l \cdot SIN\alpha}{\lambda} \quad [in \ \lambda] \tag{5.8}$$

The criteria 3 and 5 might seem arbitrary, but it is important to get feeling for the maximal distance that can be allowed between positions without affecting the E_r-component to much. The output of the program is listed in table 5.2, with $\gamma = 2°$ and $f = 11.5$ GHz.

az.ang. deg.	viewpnt.	int.per. mm	dis.sft. mm	phs.sft. deg.	bore.sft. lambda
45.0	leftwall,rail	89.00	180.92	731.78	4.91
40.0	leftwall,rail	111.43	220.47	712.30	5.44
35.0	wing feed	144.15	265.96	664.23	5.85
30.0	wing feed	194.58	291.85	539.96	5.60
25.0	output feed	278.24	338.15	437.52	5.48
20.0	leftwall,corn.	432.27	825.52	687.50	10.83
15.0	mainrefl.	765.06	758.58	356.95	7.53
10.0	mainrefl.	1715.93	1268.35	266.10	8.45
5.0	mainrefl.	6850.72	3520.87	185.02	11.77
4.0	mainrefl.	10701.86	5331.71	179.35	14.27
3.0	mainrefl.	19021.60	10770.60	203.84	21.62
-3.0	mainrefl.	19021.60	11550.48	218.60	23.19
-4.0	mainrefl.	10701.86	5853.12	196.89	15.66
-5.0	mainrefl.	6850.72	3957.03	207.94	13.23
-10.0	backwall rgt.	1715.93	1833.35	384.63	12.21
-15.0	backwall rgt.	765.06	1156.43	544.16	11.48
-20.0	rightwall,corn.	432.27	825.52	687.50	10.83
-25.0	subrefl.	278.24	422.46	546.59	6.85
-30.0	subrefl.	194.58	285.25	527.74	5.47
-35.0	wing subrefl.	144.15	242.50	605.62	5.34
-40.0	rightwall,rail	111.43	220.47	712.30	5.44
-45.0	rightwall,rail	89.00	180.92	731.78	4.91

Explanation of the abbreviations used in the table:
az.ang.= azimuth angle
viewpnt.= part of the room at which antenna boresight is pointing
int.per.= period of interference pattern
dis.sft.= maximal movement along rail to keep angle-variation $\gamma \le 2°$
phs.sft.= resulting phase-shift of Er relative to Ed
bore.sft.= resulting distance between the antenna boresight

Table 5.2   Interference period as a function of the azimuth-angle for f= 11.5 GHz.

Table 5.2 shows that the near-axis incident fields cause very slow variations in the range field. The fourth column indicates a movement over a total length of $\pm 10m$ is necessary in order to measure an interference pattern of $\pm 20m$ at 3°. Of course this displacement is not reasonable because no test zone has such large dimensions. This

means that corrections near the mainlobe become critical. The interference period for the larger azimuth-angles are acceptable.

In section 5.2 it has been explained that by coherent data-plotting a circle can be constructed which is used to extract E_d and E_r. Coherent plotting is achieved by phase-shifting each measurement proportional to the distance between the corresponding positions. At least three measurements on different positions are needed to construct the circle. However for verification purposes four measurements were applied. It is of great importance that an appropriate sampling space between the four successive positions is chosen within the interference pattern. A distance to large causes that E_r changes to much. On the other hand the interference can't be accurately distinguished with a sampling space to small. The result is a small phase-shift of E_r relative to E_d, so that it is impossible to reconstruct a reliable circle. As observed from table 5.2 the interference period strongly depends on the azimuth-angle. An optimal choice is dividing the entire azimuth-range in subranges. For each subrange the best sampling spacing can be determined from the table. In our particular case the range between $\pm 45°$ has been divided in two subranges:

* $-15° \leftrightarrow +15° \Rightarrow 3 \times 30cm$ displacement
* $-45° \leftrightarrow -15°$, $+15° \leftrightarrow +45° \Rightarrow 3 \times 4cm$ displacement

The displacements are sufficient to accurately reconstruct circles.

In the algorithm Käsa's least squares circle fitting procedure [29] was implemented. Let (x_i, y_i) represent the xy-coordinate of the ith data-point, N the number of data-points, (A,B) the centre-coordinates, and R the radius of the circle (figure 5.8).
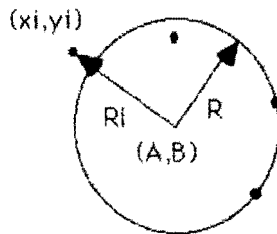
Figure 5.8 *The measured points and the parameters of the fitted circle.*

A least squares error criterion for circle fitting is

$$\sum_{i=1}^{N} (R_i - R)^2 = min$$

$$R_i = \sqrt{(x_i - A)^2 + (y_i - B)^2}$$

(5.9)

Unfortunately, this expression is hard to handle analytically and consequently a modified least squares error criterion is used, eqn. (5.10).

$$\sum_{i=1}^{N} (R_i^2 - R^2)^2 = min \qquad (5.10)$$

For a small error, i.e. $R_i \simeq R$, eqn. (5.10) gives a result close to eqn. (5.9) because of the factorizing of eqn. (5.10),

$$\sum_{i=1}^{N} (R_i + R)^2 (R_i - R)^2 = min \qquad (5.11)$$

and the fact that $R_i + R \simeq 2R$ is nearly constant.
Eqn. (5.10) can be rewritten as

$$u = \sum_{i=1}^{N} [(x_i - A)^2 + (y_i - B)^2 - R^2]^2 = min \qquad (5.12)$$

where (A,B) and R are to be determined. The extremum can be simple evaluated by making the derivates equal to zero.

$$\frac{\delta u}{\delta A} = \frac{\delta u}{\delta B} = \frac{\delta u}{\delta R} = 0 \qquad (5.13)$$

A simple relation can be derived from eqn. (5.13) for the best-fit circle parameters (A,B) and R:

$$Q = D^{-1} \cdot E \qquad (5.14)$$

where:

$$D = \begin{bmatrix} 2\sum x_i & 2\sum y_i & N \\ 2\sum x_i^2 & 2\sum x_i y_i & \sum x_i \\ 2\sum x_i y_i & 2\sum y_i^2 & \sum y_i \end{bmatrix} \qquad (5.15)$$

$$E = \begin{bmatrix} \sum (x_i^2 + y_i^2) \\ \sum (x_i^3 + x_i y_i^2) \\ \sum (x_i^2 y_i + y_i^3) \end{bmatrix} \qquad (5.16)$$

$$Q = \begin{bmatrix} A \\ B \\ C \end{bmatrix}$$

(5.17)

$$C = R^2 - A^2 - B^2$$

(5.18)

After the determination of the best-fit circle, the following checks should be performed:

1) How well does the circle fit, or in other words is the deviation of each data-point relative to the circle acceptable. A useful criterion for shaping an error-bound around the circle is:

$$\frac{|R_{vec} - R_{cir}|}{R_{cir}} < max. \ deviation$$

(5.19)

Figure 5.9 illustrates the use of an error-bound.
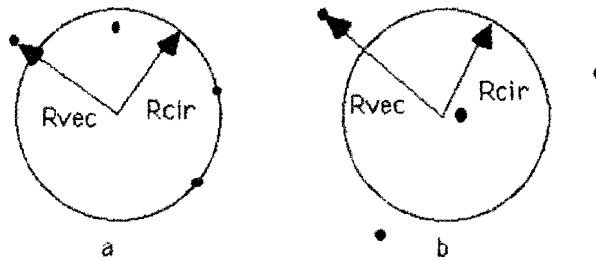
Figure 5.9 *Circle fitting.*
a) Circle accepted
b) Circle rejected

In case a the deviations are acceptable, whereas in case b some data-points far exceed the error-bound. Deviations may for example be caused by measurement inaccuracies. The circle in case b is doubtful and will be rejected.

2) An accepted best-fit circle on the basis of eqn. (5.19) still doesn't have to be reliable. In some cases ambiguous circles are found, see figure 5.10.
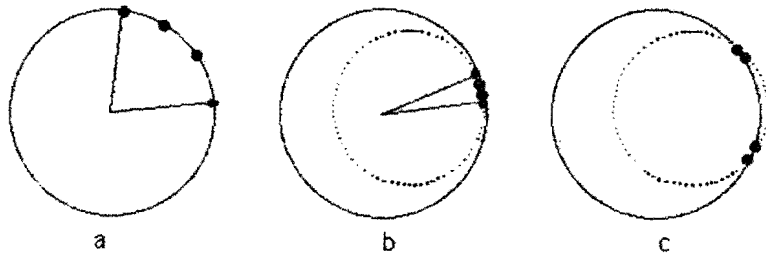
Figure 5.10 *Reliability of best-fit circles.*
a) Circle reliable
b and c) Ambiguous circles

It is obvious that circle a is reliable. In the cases b and c there is uncertainty because as well the solid as the dotted circles are possible. Therefore the algorithm checks the distribution of data-points around the circle. Whenever the data-points are concentrated in one or two small areas relative to the circle, it will be rejected.

3) By coincidence it might be possible that the data-points are well distributed within the error-bound. These random circles are approved on the basis of criterion 1 and 2. The randomness is easy determined if no extraneous fields are detected on the adjacent measurement data in the azimuth-domain. The algorithm employs this correlation of measurement data for the detection and removal of spurious corrections. In the same way the correlation is used in an interpolation routine to restore measurement data having errors, see section 5.3.4.

5.3.3 Mutual coupling

Multiple reflections contribute to mutual coupling between the range antenna and the AUT. The multiple reflections can be reduced by matching the AUT well. We consider the antenna-boresight is pointing directly into the range main reflector. The multiple reflections is composed of different components that have travelled the main path of the range field in multiple. The first reflection component is dominant over the other ones and the travelled path is three times the main path. Therefore the period of interference in longitudinal direction is $\lambda/2$ as can be deduced from figure 5.11.
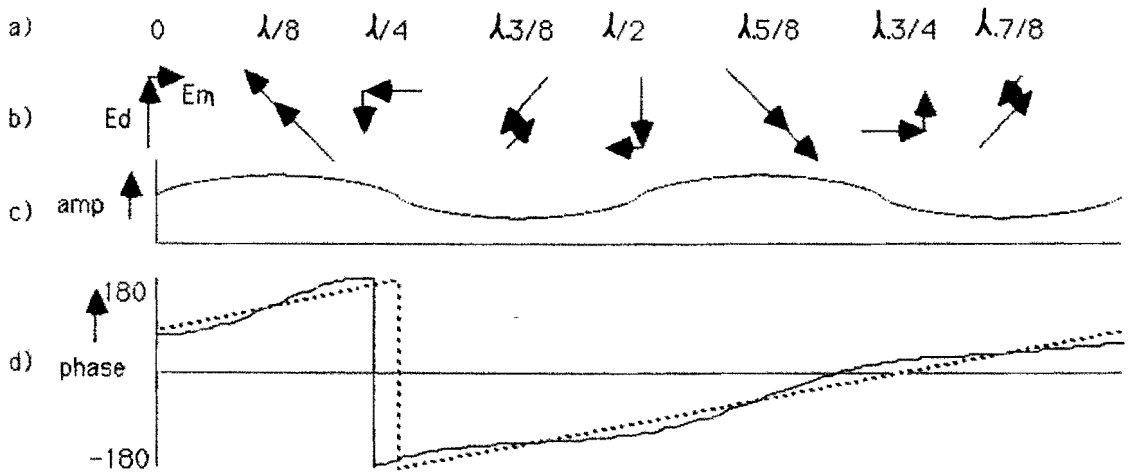
Figure 5.11 *Mutual coupling.*
a) Distance in longitudinal direction
b) Interaction of vector components
c) Amplitude-ripple
d) Phase-ripple

A combination of an extraneous field and mutual coupling leads to a more complicated interference pattern. This is illustrated in figure 5.12.
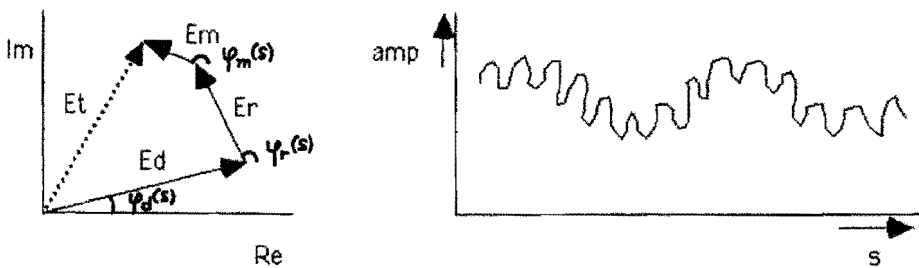
Figure 5.12 *Complicated interference patterns by three field components.*

The vector model in figure 5.12 was used to derive an expression for the amplitude and the phase-ripple. It is assumed that $E_d = 10$, $E_r = 3$, $E_m = 1$ and $\lambda_{Er} = 5 \times \lambda_{Em}$. The resulting graphs are depicted in figure 5.13.
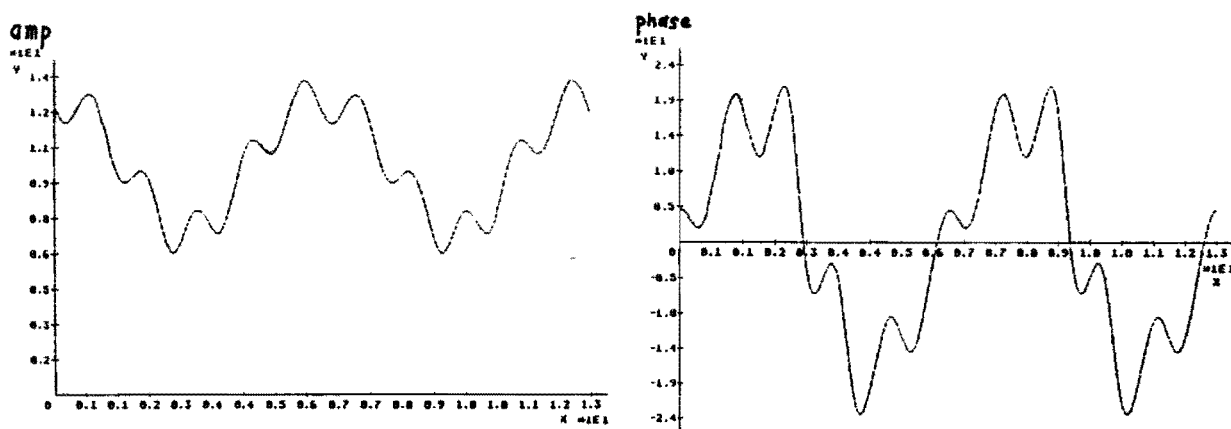
Figure 5.13 *Simulation results of mutual coupling.*
a) Amplitude
b) Phase-ripple

The expression for figure a is:

$$y = \sqrt{[10+3COSx+COS(5x+2)]^2 + [3SINx+SIN(5x+2)]^2}$$

(5.20)

The expression for figure b is:

$$y = ARCTAN \frac{3SINx+SIN(5x+2)}{10+3COSx+SIN(5x+2)}$$

(5.21)

Even three vectors depending differently in phase on the distance create complicated interference patterns. Figure 5.13 proves that it is impossible to separate the vector components form only four measurements. The mutual coupling causes deviations around the circle if the method in the previous section is applied. When the magnitude of E_m falls below the error-bound, it might be possible to approximate E_r.

In general the influence of mutual coupling in pattern measurements of high-gain antennas decreases significantly for wider azimuth-angles. Only the mainlobe and near-in sidelobes are affected, see figure 5.14.
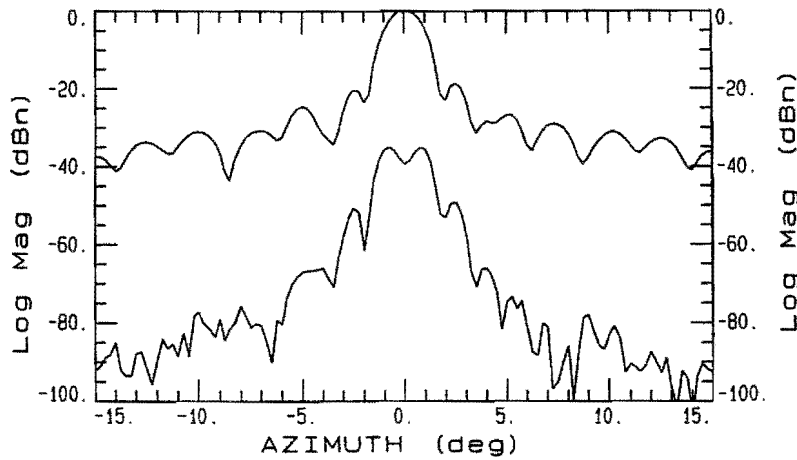
Figure 5.14 *Magnitude of mutual coupling relative to pattern data.*
(1.2m parabola, 10.6 GHz, H-plane)

Thus the correction process for wider angles doesn't have to account for mutual coupling. It is justified to use the algorithm described in the previous section. But the reflectivity level of mutual coupling in the mainlobe region can't be neglected. Some kind of correction process must be applied there. In the previous section it has already been noticed that the interference pattern for small angles of incidence is slowly varying. On the other hand the interference period of mutual coupling is in the order of $\lambda/2$. Now if the distance between successive measurement positions is kept small the vector $\vec{E}_d + \vec{E}_r$ will be almost constant. So the total variation in $\vec{E}_d + \vec{E}_r + \vec{E}_m$ is charged for $\vec{E}_m$. On the mainlobe itself $\vec{E}_r$ can even be considered zero.

An existing technique to correct for mutual coupling is the staggered z-scan technique [28]. Two measurements are performed along the range axis with a separation of $\lambda/4$. In figure 5.15a E_{t1} and E_{t2} represent the complex data that is composed of the vectors E_d and E_m.
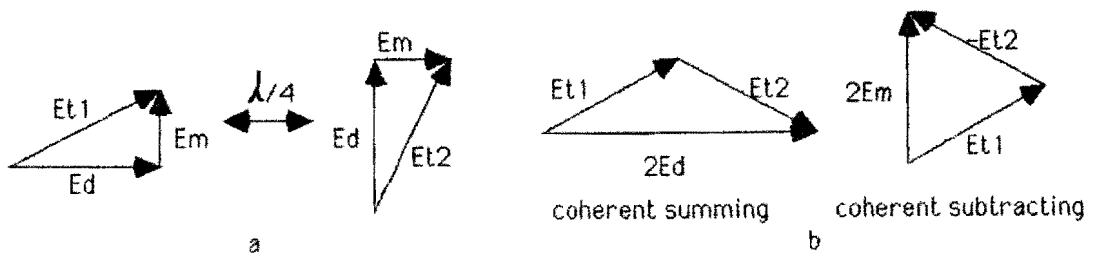
Figure 5.15 *Staggered z-scan technique.*
a) Measurement data
b) Coherent plotting

The phase-shift of E_d and E_m is 90° and 270° respectively as shown in figure 5.15a. Accounting for the 90° phase-shift E_{t1} and E_{t2} can be coherently summed or subtracted to derive E_d and E_m resp. according to figure 5.15b. With the staggered z-scan technique the mainlobe region can be corrected for mutual coupling. Disadvantages are the need for accurate positioning equipment and only one frequency at a time can be measured.

A more versatile method is preferable. In the absence of any error sources mutual coupling could be extracted from the measurement data in the same way as extraneous fields. However in practice an extra complication is phase-noise. The "novel APC-methods" in section 5.3.2 relies on accurate amplitude and phase data. When the disturbing component is large in comparison to the direct component the phase-ripple will be significant. But the phase-ripple due to mutual coupling is in the order of the phase uncertainty (a few degrees). In table 5.3 the maximal variation in phase due to mutual coupling is calculated.

top-top amplitude variation due to mutual coupling in dB	maximal phase-ripple top-top in degrees
0.1	0.66
0.2	1.32
0.3	1.98
0.4	2.64
0.6	3.96
0.8	5.28
1.0	6.59
2.0	13.16

Table 5.3 Phase-ripple in relation to magnitude of mutual coupling.

The circle-algorithm cannot be successfully applied for corrections on mutual coupling. A measurement example of the distorted phase-ripple is given in figure 5.16.
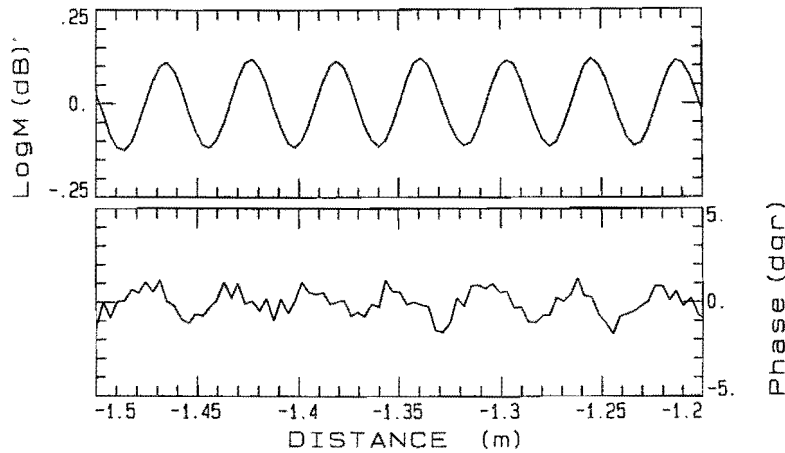
Figure 5.16 *Amplitude- and phase-ripple due to mutual coupling.*
(1.2m parabola, 11.8 GHz , H-plane)

On the contrary the amplitude data is quite stable. For this reason another procedure for the extraction of mutual coupling has been developed, which solely relies on amplitude-data. First azimuth-scans are made on six positions with spacings of only 2.5mm. Now the samples in the azimuth-range $\pm 5°$ are used to determine the best-fit sine in the amplitude data. This is illustrated in figure 5.17.
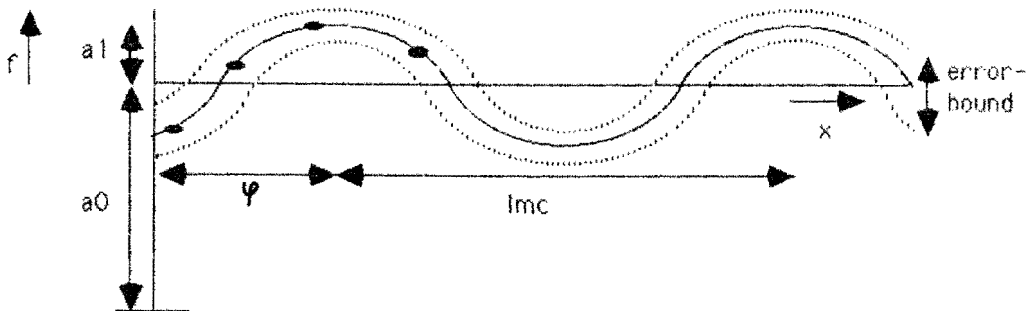
Figure 5.17 *Determination of a best-fit sine.*

The parameters a_0, a_1, *and* φ of eqn. (5.22) must be derived from sine-fitting.

$$f= a_0 \quad a_1 \cdot COS(kx+\varphi) \tag{5.22}$$

where:
* $k= 2\pi/lmc$
* $lmc= \lambda/2$
* $E_d= a_0$
* $E_m= a_1$

Just like the circle-algorithm the sine fitting method is based on a least squares method. The variables a_0 *and* a_1 are derived from eqn. (5.23).

$$a_0 \cdot m + a_1 \cdot \sum COS(kx_i + \varphi) = \sum y_i$$
$$a_0 \cdot \sum COS(kx_i + \varphi) + a_1 \cdot \sum [COS(kx_i + \varphi)]^2 = \sum y_i \cdot COS(kx_i + \varphi)$$

(5.23)

where:
* m is the number of samples
* x_i = sampling position i
* y_i = measured amplitude

The variable φ is iteratively determined by minimizing the least squares error. An error bound around the sine is based on the following criterion:

$$\frac{|y_i - f|}{a_1} < max. \ deviation$$

(5.24)

At this stage the amplitude of E_d *and* E_r are known. Next the correction of the phase-data is implemented in the same way as in figure 5.4, section 5.3.1.

5.3.4   Measurement procedure and algorithm

As described in the previous section two techniques were developed to correct the mainlobe for mutual coupling and the sidelobes for extraneous fields. Because of the resemblance with the well-known APC-method these are referred to as the "novel APC-methods". Both techniques can be implemented in a single measurement procedure. A schedule of the scan-trajectory is given in figure 5.18.
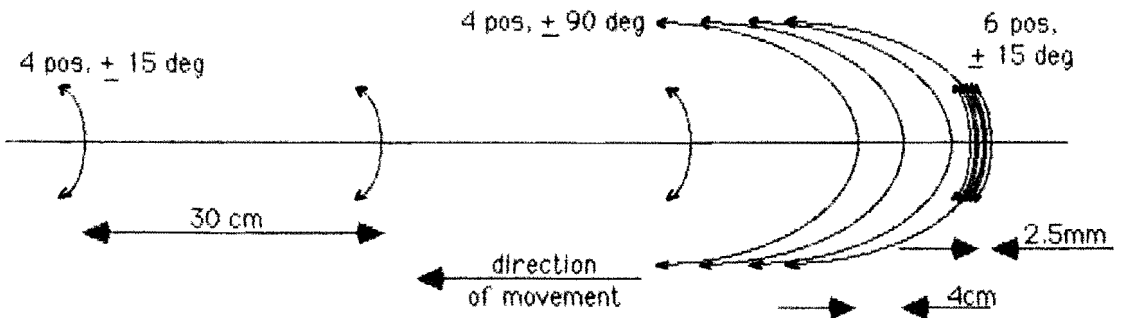
Figure 5.18 Scan-trajectory.

Starting-point in the determination of the most convenient scan-trajectory is a frequency of 11.5 GHz. The first position is chosen as the reference plane, i.e. all phase-shifts are determined relative to this plane. The movement is backwards, in a direction

opposite to the range reflectors. First pattern cuts are made in the azimuth range $\pm 15°$. Measurements are performed on 6 positions with small spacings of only 2.5mm and next on 3 positions with spacings of 30cm. The combination of six measurements is used for the mutual coupling extraction, whereas the combination of the 3 measurements joined with the measurement in the reference plane is used for extraneous field extraction. Then 4 measurements are performed in the azimuth-range $\pm 45°$ with spacings of 4cm for extraneous field extraction. In the latter case only data above $\pm 15°$ is used for corrections. But because boresight data is needed for distance determination it is the easiest way to measure the range between $\pm 45°$ as a whole. An indication of the measurement time is about 3 hours under the conditions:

* step in azimuth $0.25°$
* 11 frequencies measured simultaneously
* 64 averages

After this a longitudinal scan should be made for distance determination. An indication of the measurement time is 1 hour under the conditions:

* 5 samples per $\lambda/2$ at 11.5 GHz
* 11 frequencies measured simultaneously
* 32 averages

To process the acquired data an algorithm has been developed. The programming language is Fortran and the program is ARCS-compatible. (ARCS is the name of the data-acquisition program at the antenna-lab of EUT.)

The algorithm for distance determination, mutual coupling and extraneous fields has already been dealt with in a bird's-eye view in the previous sections. The exact structure will not be treated in this report for not boring the reader. The software is well-documented and consists of a main program with the name "Correct". "Correct" calls a number of subroutines that are contained in the library "Janlib". The global structure is given on the next page.
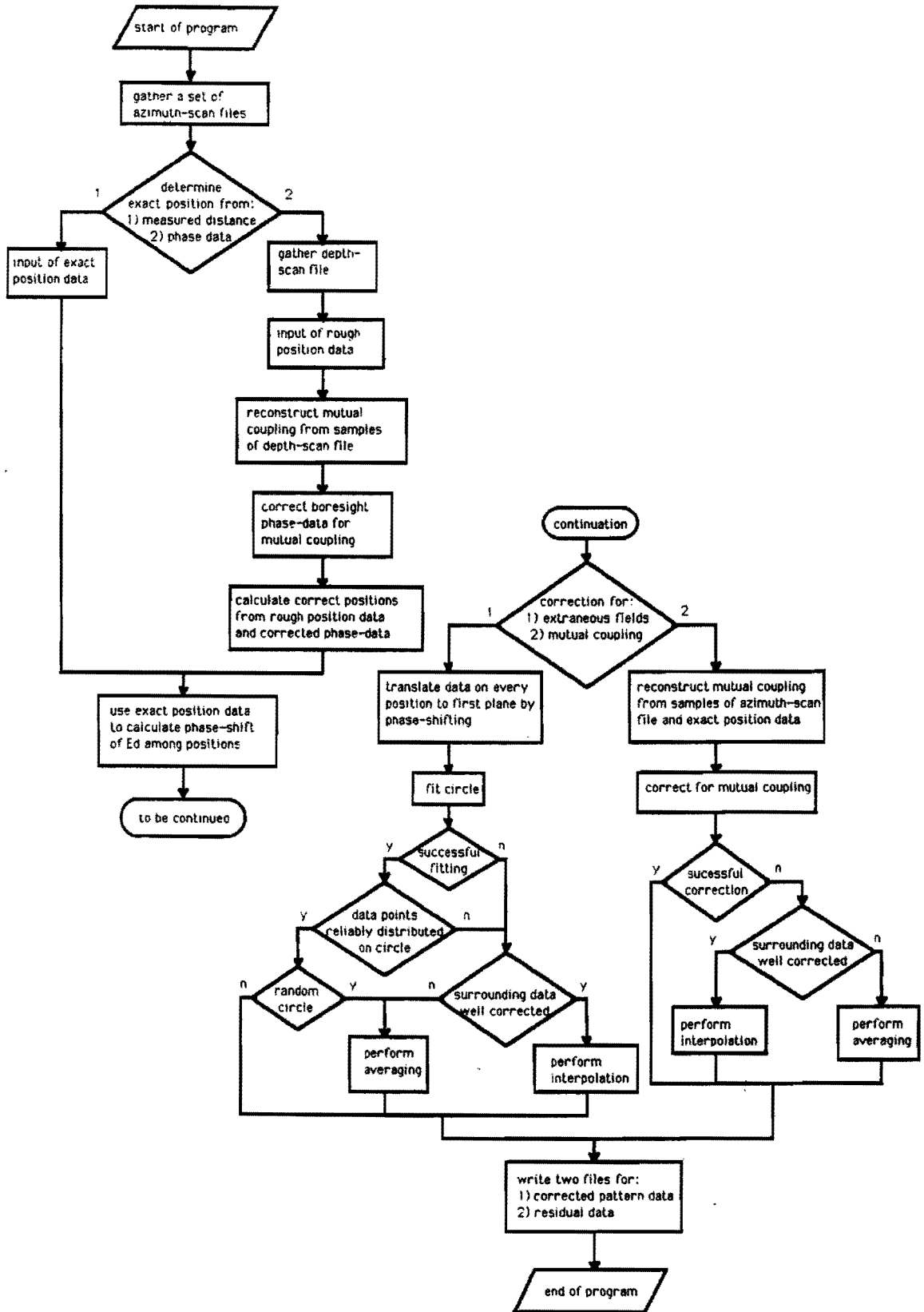
Figure 5.19 *Block diagram of the correction-algorithm.*

The block diagram speaks for itself. After the program-start the exact distances between positions are determined. Next the phase-shifts are calculated for further processing. A choice must be made between a correction for mutual coupling or extraneous fields. In both cases the correlation of the data is used to interpolate measurement data that cause problems during the correction process. The interpolation is based on a quadratic polynomial for the local correction of a single data-point. The program produces the following output:

* A radiation pattern that is partially corrected (E_d).
* An angular pattern of the extracted extraneous field component (E_r) or mutual coupling component (E_m).

The results of processing all scan-data are three partially corrected patterns for respectively:

1) mainlobe region
2) sidelobe region $-15°\leftrightarrow+15°$
3) sidelobe regions $-45°\leftrightarrow-15°$ *and* $+15°\leftrightarrow+45°$

The program "Join" joins these three regions into a single file. So the entire true radiation pattern is obtained.

5.4 Experimental investigations

The first experiments were not very successful because the distance determination wasn't accurate enough and due to the presence of other error sources. Therefore the most apparent error sources were investigated. This was very clarifying so that afterwards successful measurements have been made. The results prove the validity of the "novel APC-methods".

5.4.1 Error sources

Chapter 3 was devoted to all error sources possible in antenna measurements. It was concluded that quantitative information about the errors is difficult to get. For the error sources are hard to isolate from each other. In fact the measurement system should be considered as a whole. A layout of the measurement system at EUT is given in figure 5.20.
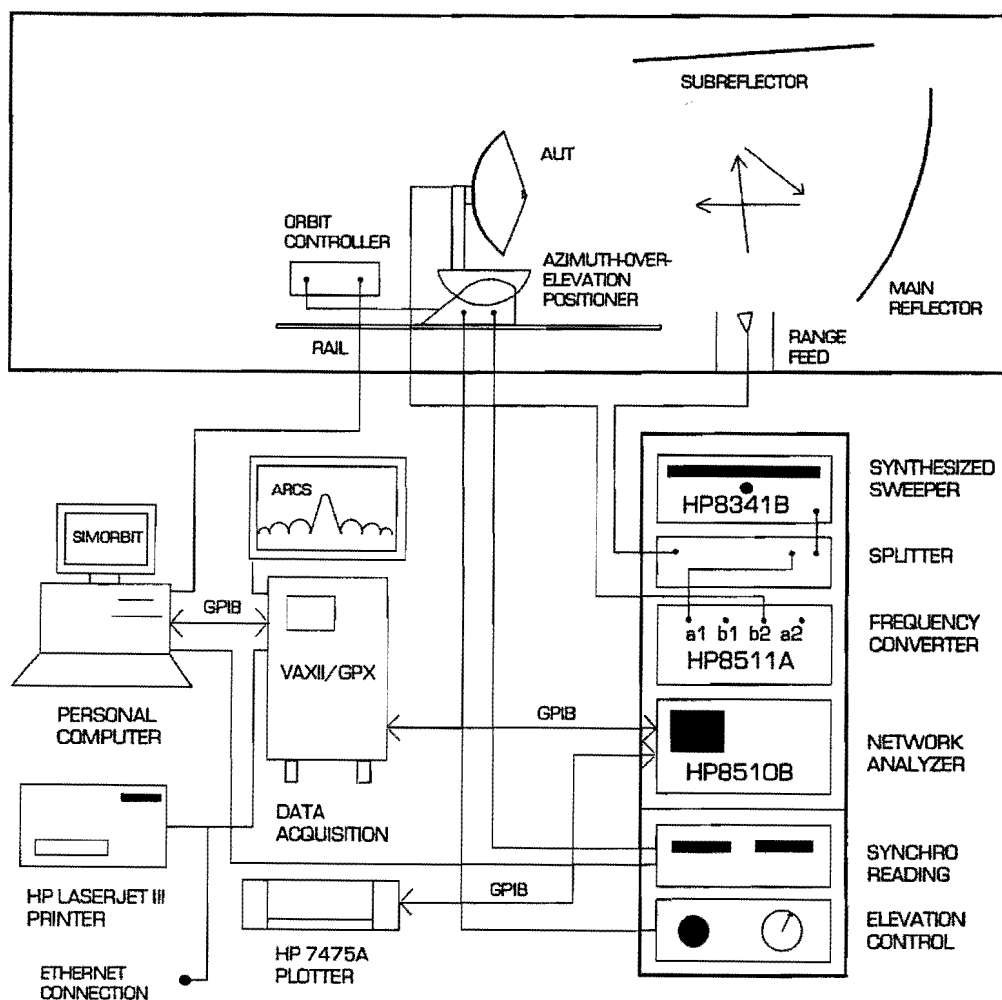
Figure 5.20 Layout of the measurement system at EUT.

The following experiments with a 1.2m parabola in the H-plane were established:

1) A comparison between continuous frequency-sweeping and synthesized frequency-sweeping. These features of the HP8510 network-analyzer are also referred to as ramp-mode and step-mode respectively. In both modes 5 calibrated measurements were performed within 5 minutes, succeeding each other without any modifications to the system. The total frequency range is 10-13 GHz, 801 frequencies, 64 averages (for noise-reduction) and the antenna on boresight. The frequency range 11.45-11.55 GHz has been outlined in figure A1.1 and A1.2 of the appendix. The differences in amplitude ($\pm$ 0.025 dB) are small in both cases. But opposite to the step-mode, the phase in the ramp-mode is not stable. The first verifications of the "novel APC-methods" performed in the ramp-mode, became a disaster due to the

phase unstability. Therefore after this experience only the synthesized mode was used. The HP8510 network-analyzer is specified to have a RMS magnitude error of $\pm$ 0.05 dB and phase-error of $\pm$ 0.3° at 10 dB above the reference level for the HP8510.

2) The optimal number of averages and signal-drift in the step-mode.
The HP8510 offers the feature of averaging measurements in order to improve the SNR. The maximal number of averages possible is 4096. However one should be modest because the duration of data acquisition increases rapidly with the number of averages. An error source often overlooked, that accompanies large measurement times is signal-drift. Plots have been made on the HP8510 with the antenna on boresight, in a narrow frequency range at 11.5 GHz in step-mode, see figures A1.3, A1.4. A comparison between figure A1.3 and A1.4 shows the effect of noise-reduction by averaging. It seems that the most optimal number of averages is 64. Enlarging the number of averages leads to only slight visible improvements in the SNR and so is a waste of time. Moreover this would cause the drift-error to increase. To study the effect of signal-drift two plots were made with an interval of 15 minutes in figure A1.4. The amplitude remains quite stable ($\pm$ 0.01 dB), but there is a significant drift in phase about $\pm$ 0.4°.

3) Cable-bending and -torsion.
Modern phase-stable RF-cables are employed in the measurement system at EUT. The type of RF-cable is Sucoflex 104P, and important specifications for the phase-stability are:
* vs. bending $\Rightarrow$ $0.2°/GHz{\cdot}turn$
* vs. torsion $\Rightarrow$ $0.5°/GHz{\cdot}turn$
* vs. temperature-change between $10°C$ *and* $30°C$ $\Rightarrow$ $0.6°/GHz$
During the measurement of the "novel APC-methods" it is very important to be careful with cable-motion. Figure A1.5 illustrate the effects that only small cable-motions may have on the signal-stability. The total frequency range is 10-13 GHz, 401 frequencies, step-mode, 64 averages and the antenna on boresight. The time between successive measurements was in the order of one minute in order to minimize the effects of signal-drift.

4) Shocks and vibrations of the antenna support.
The range-positioners as well for azimuthal scanning as longitudinal scanning should employ appropriate accelerations and decelerations in order not to cause shocks an vibrations of the antenna support. Figure A1.6 illustrates the effects of pushing the antenna a little. The total frequency range is 10-13 GHz, 401 frequencies, step-mode, 64 averages and the antenna on boresight. The time between successive measurements was in the order of one minute so that the effect of signal-drift was

minimized. Also care was taken to reduce cable-motions.

5) Successive mainlobe-measurements.

A combination of the previous effects in 1, 2, 3 and 4 has been investigated by means of measuring the mainlobe. Four measurements were performed in the azimuth-range $-5°\leftrightarrow+5°$, $0.1°$ azimuth-step, CW-frequency$=$ 11.5 GHz, 64 averages, single position. The range $-0.25°\leftrightarrow+0.25°$ is outlined in figure A1.7. The measurements 1, 2 and 3 are performed immediately after each other. The time-interval between measurement 3 and 4 is 15 minutes. As observed from the figure A1.7 the deviations in amplitude are negligible. However significant deviations in phase occur as one would suspect. An important factor that musn't be forgotten is also the inaccuracy of the positioning equipment.

To summarize, an attempt for an error budget is made:
* Accuracy in the synthesized mode according to the specification of the HP8510 $\Rightarrow$ $\pm$ 0.05 *dB*, $\pm$ 0.3° at 10 dB above the reference level of the HP8510.
* Signal-drift in the synthesized mode over 15 minutes and 64 averages $\Rightarrow$ $\leq$ 0.01 *dB*, $\leq$ 0.5°.
* Cable-motion $\Rightarrow$ $\leq$ 0.1 *dB*, $\leq$ 0.5 °.
* Shocks/vibrations of the antenna support $\Rightarrow$ $\leq$ 0.1 *dB*, $\leq$ 5°.
* Positioning inaccuracy $\Rightarrow$ $\leq$0.05° in azimuth.
* Inaccuracy in distance determination $\Rightarrow$ $\leq$ 0.1*mm*, equivalent to $\leq$ 1.4° phase-error at f= 11.5 GHz.

5.4.2 Results

In this section the measurement results belonging to the "novel APC-methods" will be presented. Preliminary measurements were a few longitudinal scans to investigate the interference patterns and sidelobe measurements. Thereafter measurements were performed to verify the validity of the "novel APC-methods". Antennas under test were:
* 1.2m-parabola
* 2m-parabola
* horn

Both parabolic antennas are highly directive so the "novel APC-methods" are very suitable for correcting their radiation patterns. On the contrary problems might be expected in correcting the measurements of the horn. A benefit of the 2m-parabola over the 1.2m-parabola is that it doesn't suffer from backlash. Therefore two measurements can be performed in the same plane of polarization by rotating the antenna 180°. After correcting both measurements the patterns should be the same.

Another way to verify the new technique is comparing the corrected pattern with the results achieved by time-gating. For not getting long-winded descriptions only the most striking results will be treated. All measurement results are presented in the appendix and the comments to the plots will be sufficient.

5.4.2.1 Preliminary measurements

Experiments in the past have shown that extraneous field sources are present in the CATR at EUT. The situation is depicted in figure 5.21.
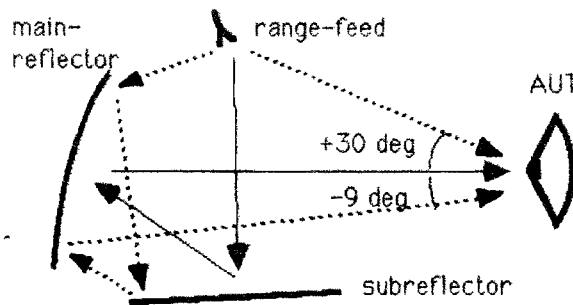
Figure 5.21   Two dominant field sources disturbing the plane wave.

Problems in the pattern data may therefore be expected in the azimuth-range around +30° and around -9°. Besides these sources, mutual coupling decreases the accuracy of the mainlobe measurement. A picture in time domain helps to distinguish these signals, figure 5.22.
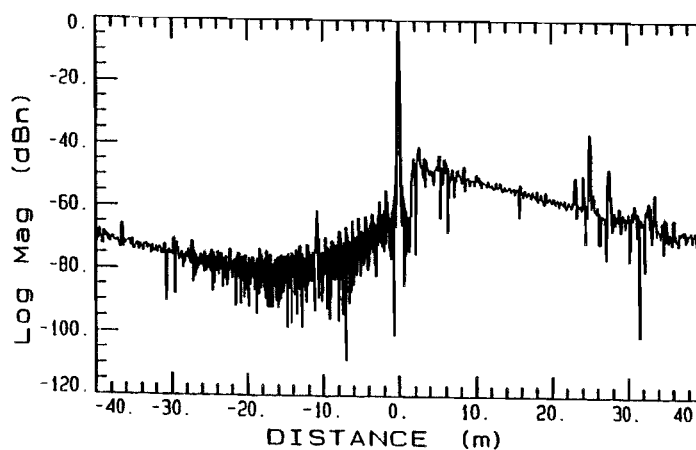
Figure 5.22   Time-domain response. (2m parabola, 11.5 GHz, H-plane, azi= 0°.)

Figure 5.22 clearly shows the leaking signal from the feed arrives before the main-response (-10m), whereas the first component of the mutual coupling arrives 25m afterwards. These distances are in accordance with the physical path lengths and coaxial delays.

An investigation was made to the interference patterns in longitudinal directions as a result of the aforementioned field sources. The scans made for different azimuth-angles are depicted in appendix A.2. In the mainlobe region $-3°\leftrightarrow+3°$ mutual coupling is the dominant interfering source, see figures A2.1-A2.4. The ripple period is about $\lambda/2$ as expected. For larger azimuth angles the influence of extraneous fields becomes visible, see figures A2.5-A2.12. Normally mutual coupling is negligible on the sidelobes according to section 5.3.3. However under certain conditions even for larger azimuth-angles there might be exceptions to this rule. Figures A2.7-A2.9 show the combined effects of mutual coupling and extraneous fields for the angles $+20°$ and $+30°$. In these cases measurements were performed while the antenna boresight was pointing to the feed. However no absorber was used to prevent leakage and even a metal plate near the feed was visible. The first omission caused an increased leakage signal from the feed to the AUT. The second omission resulted in a disastrous mutual coupling between the AUT and the metal plate. It also seems that the ripple of the mutual coupling isn't $\lambda/2$. For instance in figure A2.8 62 periods are counted over 900mm. Thus the ripple period= 900/62= 14.52mm, whereas $\lambda/2=$ 13.04mm at 11.5 GHz. This indicates that the multiple reflections don't travel the same path as the main wave. Probably most reflected/reradiated energy will be directed to the antenna boresight. The ripple due to mutual coupling disturbs the correction process as described in section 5.3.3. For this reason care must be taken that no uncovered metal plates, other than the range reflectors, are present in the anechoic chamber. Covering the metal plate with absorber gives a mutual-coupling free interference pattern, see figures A2.10,A2.11. Further improvements are achieved by masking the range feed to prevent leakage. These simple measures almost entirely suppress all disturbances as shown in figure A2.12

Also the coherence between extraneous fields in the azimuth domain and the frequency domain has been investigated. Concerning the azimuth domain 4 pattern cuts were made with an interval of 5cm in the range $15°\leftrightarrow30°$. These are plotted in dots in figure A2.13, A2.14. The corrected pattern is presented in continuous line. Comparing these results with the gated measurements in figure A2.15, A2.16, shows that both corrected patterns are identical. Thus the corrections seem reliable. Finally the residual component has been plotted in figure A2.17. The amplitude- (cont.) and phase-curves (dot.) are quite smooth. This indicates that in the residual source distributions no abrupt changes occur. In fact diffraction effects are observed. Concerning the frequency domain 4 measurements were performed with the antenna boresight at $-9°$. Figure A2.18, A2.19 show the measured pattern on the first position (dot.) and the correction (cont.) in the range 10-13 GHz. Figure A2.20 shows that also in the

frequency domain the amplitude (cont.) and phase (dot.) behave coherent.

5.4.2.2 1.2m-parabola

To fully characterize the antenna measurements have been performed in the co-polar H-, E-, and 45°-planes and in the cross-polar 45°-plane. 11 frequencies were measured in the range 10-13 GHz with an interval of 300 MHz. The number of averages is 64. The maximal step in azimuth is calculated from eqn. (5.25).

$$\frac{1}{n} * 2\pi/(\frac{\pi D}{\lambda/2}) = \frac{\lambda}{nD} \quad [rad] \tag{5.25}$$

where D is the diameter of the antenna and n determines the oversampling. Substitution leads to a step in azimuth of 0.25° in the range $-45°\leftrightarrow+45°$.
The results are depicted in the appendix. Figures A3.1-A3.3 show the mutual coupling on the mainlobe. The amplitude of the mutual coupling is about ±0.1 dB at 0 dB level. This seems to be not very large although one has to realize that this is the variation on the mainlobe. According to figure 3.7 this is equivalent to a reflectivity level of -45 dB and thus cannot be neglected. For instance a typical accuracy in gain specified for testing satellite antennas is ±0.25 dB [1]. Figure A3.1 shows the presence of a slow variation in the range field besides the ripple due to mutual coupling. However cable-motion may also cause variations.
In the H-plane, the antenna is situated symmetrically relative to the scan axis. In addition figure A3.4 shows that the corrected pattern is almost symmetrical. This is a good indication for the validity of the "novel APC-methods".
The new technique is also compared to time-gating. The fact that both curves in figure A3.3 coincide means that the mainlobe is well corrected for mutual coupling. It can be concluded too from the figures A3.7-A3.10 that the low-sidelobes are well corrected for extraneous fields. Deviations occur in the near-in sidelobes of the two techniques. The explanation is that extraneous signals with a small angle of incidence cannot be distinguished in the time-domain because the difference in path-length between the main signal is to small. Therefore near-in sidelobes are not corrected by time-gating whereas the new technique is still effective.
It is observed from the figures A3.8-A3.10 that the magnitude of the disturbances doesn't depend on the frequency very much. The problems of the CATR illustrated in figure 5.21 are clearly visible.
The description above for the H-plane also applies to the other co-polar measurements in the 45°-plane and the E-plane. In figure A3.12 the interference pattern with the antenna directed to the range feed is shown. Large deviations occur but the pattern is quite smooth as expected. A longitudinal scan to survey the interference pattern on boresight in the 45° cross-polar plane is depicted in figure A3.19. The ripple deviates

from a sine-wave that is usual to mutual coupling. There is no explanation for this phenomenon. In figure A3.20-A3.23 it is seen that large deviations occur in the cross-polar pattern. The corrections seem to be well.

5.4.2.3 2m-parabola

To fully characterize the antenna measurements have been performed in the co-polar H-, E-, and 45°-planes and in the cross-polar 45°-plane. 11 frequencies were measured in the range 10-13 GHz with an interval of 300 MHz. The number of averages is 64. The maximal step in azimuth is calculated from eqn. (5.25).
Substitution leads to a step in azimuth of 0.2° in the range $-45°\leftrightarrow+45°$.
To be short the same description applies as to the 1.2m-parabola. The results are depicted in the appendix. Just like the 1.2m-parabola, corrections for mutual coupling and extraneous fields seem to be well. Besides time-gating another verification was made. Pattern cuts were made with the antenna in the up-position and after 180° rotation around the mechanical axis in the down-position. The 2m-parabola doesn't suffer any backlash. This way measurements are performed under different conditions in the same polar plane. The measurement results in the H- and 45°-plane are depicted in figure A4.20, A4.21 and A4.29, A4.30 respectively. The corrected pattern in the down-position has been plotted inversely over the corrected pattern in the up-position. The resemblance is excellent. The differences on the sidelobes in terms of reflectivity level can be neglected. However striking are the differences in the first sidelobe left and right from the mainlobe for both polarizations. Probably the antenna perceives an increased taper near the edges of the test zone due to its large dimensions. The non-plane-wave illumination causes errors in the first sidelobes.

5.4.2.4 Horn

Measurements have been performed in the co-polar H-, E-planes. 11 frequencies were measured in the range 10-13 GHz with an interval of 300 MHz. The number of averages is 64. The maximal step in azimuth is calculated from eqn. (5.25).
Substitution leads to a step in azimuth of 0.5° in the range $-45°\leftrightarrow+45°$.
It has already been mentioned that the success of the "novel APC-methods" depends on the directivity of the AUT. As a proof experiments on a horn were performed. Figure A5.1 and A5.7 show that mutual coupling is very small. On the other hand extra interferences occur from different angles of incidence disturbing the boresight pattern. The interference patterns in the figures A5.2, A5.3 are extra complicated due to a combination of several interfering components. However in figure A5.4 the patterns is normal because the leaking signal from the feed dominates over the other interfering

signals. The longitudinal patterns belonging to the E-plane, figure A5.8-A5.12, are not very complex. But as observed in the figure A5.9, A5.10, A5.12 the interference periods deviate from the one calculated in table 5.2. This is caused by dominant interfering signals that are incident from other directions than the horn's azimuth-angle. It can be concluded from the longitudinal scans that the horn is unable to distinguish different extraneous signals. As a result the "novel APC-methods" are not suited to correct measurements of low-gain antennas, see the figures A5.5, A5.6 and A5.13, A5.14.

5.5 Discussion

The results presented in this chapter show that reliable corrections can be made using the "novel-APC methods". In three different ways the validity was demonstrated:
* If the 1.2m-parabola is symmetrically positioned relative to the scan-axis, the pattern becomes almost symmetrical after correction.
* The corrected patterns are identical to the time-gated patterns for the low-sidelobes. In addition the extracted extraneous field components resemble exactly the time-gated disturbing field components for wider azimuth-angles. Also the extracted mutual coupling is the same for both methods.
* Upside/down-measurements using the 2m-parabola give identical patterns after correction.

It was also demonstrated that the technique is not suited for antennas having only modest directivity. As observed from longitudinal scans using a horn complicated interferences occur. However the longitudinal scans with the 1.2m and 2m parabola show a "clean" interference pattern. Thus the "novel APC-methods" rely on the directivity of the antenna, it must act as some kind of spatial filter.

The technique not only offers the ability to correct pattern data but also gives an indication of the quality of the quiet zone. For instance the influences on the test-zone field of both main interfering sources in the CATR at EUT, see figure 5.21, are clearly visible in the residual data around -9° and +30°. The most appropriate way to express the quality is by means of the PWS of the residual data. The 1-dimensional spectrum can be interpreted as a projection of the 2-dimensional spectrum on the k_x-axis when $y=0$ is the scan-plane (section 4.2.1). However the residual data doesn't contain the effects of non-plane-wave illumination such as amplitude- and/or phase-taper. For, the "novel APC-methods" only correct for extraneous fields and mutual coupling. As a consequence there might still be errors present in the first sidelobes.

A particular case are the cross-polar measurements. As observed from the longitudinal scan-data on the boresight the ripple often deviates from a pure sine-wave. There is no exact explanation for this behaviour at the moment of writing this report. Probably

there is more then one interfering signal. However concerning the corrections for extraneous fields the relation (4.23) should be kept in mind. It states that the measured cross-polar field is composed of the true cross-polar FF and the co-polar FF convolved by the co-polar residual.

Finally a comparison is made between the "novel APC-methods" in relation to time-gating.

Advantages:
* Reflections having approximately the same path-length as the direct signal can still be distinguished, i.e. near-in sidelobes can be repaired.
* The method doesn't depend on the available bandwidth.
* No need to perform measurements for a large number of frequencies.
* The method can be readily applied on existing compact ranges.
* Direct information is acquired about the magnitude and direction of reflections.

Disadvantages :
* In small regions close to the mainlobe there is doubt whether corrections are made.
* Amplitude- and phase-measurements must be accurate, especially phase.
* The movement of the antenna plus positioner to new positions requires special attention due to shocks/vibrations and cable-bending.
* The method is not suited for measuring non-directive antennas.

Chapter 6

Conclusion

The "novel APC-methods" consist of two parts: one to correct the mainlobe for mutual coupling and one to correct the sidelobes for extraneous fields. In popular words one can say that corrections are made by the creation of a synthetic aperture. The different points of view enable to distinguish extraneous fields and mutual coupling from the plane-wave. The technique not only can be used for pattern corrections but also provides a means to characterize the quality of the test-zone. The quality is well expressed by the plane-wave spectrum of the reflection-data. The PWS is derived from the reflection-data by a deconvolution with the true antenna pattern. It is important to realize that the effects of non-plane-wave illumination are not represented in this PWS. On the contrary scanning the test zone with a probe provides an entire picture of all field irregularities that degrade the quality of the test zone. This requires 2-dimensional scanning on a regular grid and is very time-consuming. Using the "novel APC-methods" and a large antenna comprising the test zone, just a single azimuth-scan on a few different positions is needed. The 1-dimensional PWS accounts for all extraneous fields that are incident upon the antennas aperture (compare section 4.2.1).

Besides the "novel APC-methods" there is another powerful technique that might be promising. This is plane-wave correction using a flat metal plate. The principle is the same as in empty-room measurements preceding RCS-measurements. During empty room measurements a sphere is used as a calibration model to characterize the scattering fields of the chamber. In the same manner the quality of the plane wave-front is characterized using a flat plate that comprises the entire test zone. It is known that ideally the response of a flat plate to a plane wave should be a sinc-function. Now every deviation of this sinc-function can be accounted for field irregularities that are used to correct the antenna measurement. Although the principle is simple extra complications occur.

Complications are:
* diffraction effects on the edges
* accurate alignment to the range field
* the flat plate should be perfectly shaped
* corrections are made after the actual pattern measurement

Therefore the "novel APC-methods" form a concurrent technique in comparison to corrections using a flat plate.

In chapter 3 a limited error budget is given for the measurement system of the antenna-lab at EUT. On the basis of this error budget and the knowledge obtained from pattern-errors due to extraneous fields and mutual coupling it is possible now to derive the overall accuracy in pattern determination. An error bound in conjunction to the application of "the novel APC-methods" is:
* mainlobe-region $\Rightarrow \pm 0.1$ *dB*, $\pm 1°$ resp. in amplitude and phase
* sidelobe-regions $\Rightarrow \pm 1$ *dB*, $\pm 5°$ resp. in amplitude and phase

This error bound depends on the following conditions:
* synthesized mode
* 64 averages
* limited cable-motions
* suppresion of shocks and vibrations

Finally the following recommendations can be made for further studies in future:
* An implementation of the "novel APC-methods" on other range-types. For instance on a SPCR, the cylindrical wavefront requires a slightly different approach.
* Expressing the wavefront quality of the test zone in a PWS. The true antenna pattern should be deconvolved from the reflection-data.
* Transversal scanning instead of longitudinal scanning. The benefit of transversal scanning is shorter interference periods than observed in longitudinal scanning. On the other hand the dimensions of the test zone should be large enough for this purpose.

Literature

[1]   Brumley, S.
"Characterizing compact range performance for space communication antenna applications.", AMTA 1992, pp. 4_9-4_14

[2]   Cuchanski, M. and S.S. Dhanjal
"Error-correction techniques in a scanning-probe near-field system.", AMTA 1990, pp. 6_25-6_29

[3]   Boyles, J.W.
"Determining measurement accuracy in antenna test.", AMTA 1990, pp. 6_43-6_46

[4]   Iigusa, K. and T. Teshirogi
"Estimation of errors due to imperfect alignment of a probe line in cylindrical near-field antenna measurement.", ICAP 1989, pp. 359-363

[5]   Joy, E.B.
"Maximum near-field measurement error specification.", Dig. Int. Symp. A&P, Stanford June 1977, pp. 390-393

[6]   Joy, E.B.
"Computer simulation of cylindrical surface near-field measurement system errors.", Dig. Int. Symp. A&P, Seattle June 1979, pp. 565-568

[7]   Bennett, J.C. and K.S. Farhat
"Wavefront quality in antenna pattern measurements: the use of residuals.", Proc. IEE, vol. 134, no. 1, Feb 1987, pp. 30-34

82

[8]   Beeckman, P.A.
      "High precision measurements on a compact antenna-test range.", Electr. Lett.,
      vol. 19, no. 19, Sep 1983, pp. 769-770

[9]   Black, D.N. et all.
      "Range field compensation.", AMTA 1991, pp 3B_19-3B_24

[10] Joffre, L. et all.
      "Antenna pattern correction for range reflections.", AMTA 1987, pp. 63-68

[11] Pereira, J.F.R. et all.
      "A procedure for near-field measurement of microwave antennas without
      anechoic environments.", ICAP 1983, pp. 219-223

[12] Q Sha et all.
      "Near-field/far-field transformation by non-plane-wave synthesis.", AMTA 1987,
      pp. 226-229

[13] Hess, D.W.
      "Time-gating of antenna measurements.", AMTA 1987, pp. 77-78

[14] Brown, J. and E.V. Jull
      "The prediction of aerial radiation patterns from near-field measurements.", Proc-
      H IEE, 1961, 108B, pp. 635-644

[15] Yaghjian, A.D.
      "An overview of near-field antenna measurements.", IEEE Trans. on Ant. and
      Prop., vol. AP-34, no. 1, Jan 1986, pp. 30-45

[16] Bennett, J.C. and E.P. Schoessow
      "Antenna near-field/far-field transformation using a plane-wave synthesis
      technique." Proc-H IEE, vol. 125, no. 3, Mar 1978, pp. 179-184

[17] Vokurka, V.J.
      "New compact range with cylindrical reflectors and high efficiency factor.",
      Proc. Electr. 1976 Conf. München, 1976

[18] Vokurka, V.J.
      "Advanced antenna measurements.", Proc. 14th European Micr. Conf., 1984, pp.
      60-70

[19] Birtcher, C.R., C.A. Balanis, V.J. Vokurka
"Quiet zone scan of the single-plane collimating range.", AMTA 1991, pp. 4_37-4_42

[20] Appel-Hansen, J.
"Reflectivity level of radio anechoic chambers.", IEEE Trans. on Ant. and Prop., vol. AP-21, no. 4, Jul 1973, pp. 490-498

[21] Crawford, M.L.
"Evaluation of reflectivity level of anechoic chambers using isotropic, 3-dimensional probing.", IEEE A&P, 1974, pp. 28-34

[22] Hess, D.W.
"Principle of the three-cable method for compensation of cable variations.", AMTA 1992, pp. 10_26-10_31

[23] Caldwell, O.M.
"An implementation of the three-cable method.", AMTA 1992, pp. 10_32-10_37

[24] Bennett, J.C. and A. Griziotis
"Removal of environmental effects from antenna radiation patterns by deconvolution processing.", ICAP 1983, pp. 224-228

[25] Griffiths, H.D . and F. Roosen
"Evaluation of anechoic chamber wavefront quality using superresolution techniques.", ICAP 1991, pp. 934-937

[26] Beeckman, P.A.
"Analysis and experiments concerning the performance and calibration of compact antenna-test ranges.", Ph.D. thesis, EM Group, Dep. of El. Eng., EUT, Sep 1987

[27] Pereira, J.F.R. et all.
"New procedure for near-field measurements of microwave antennas without anechoic environments.", Proc. IEE, vol. 131, no. 6, Dec 1984, pp. 351-358

[28] Slater, D.
"Near-field antenna measurements.", Artech House

[29] Käsa, J.
"A circle fitting procedure and its error analysis.", IEEE Trans. on Instr. and Meas., Mar 1976, pp. 8-14

Appendix A

Measurement results

A.1 Error sources

All measurements performed with the 1.2m parabola in the H-plane.
Antenna on boresight in figure A1.1-A1.6.
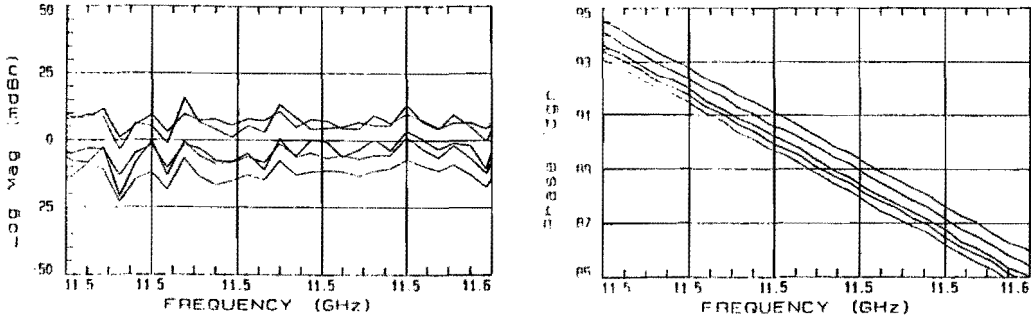
Figure A1.1 *Five successive amplitude- and phase-measurements in ramp-mode.*
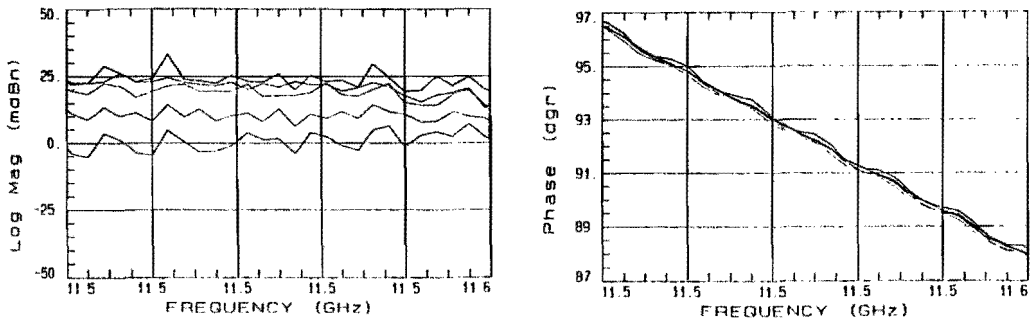
Figure A1.2 *Five successive amplitude- and phase-measurements in step-mode.*
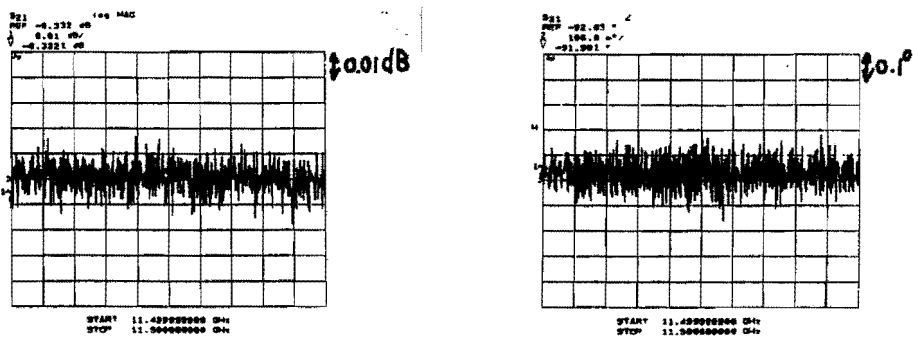
Figure A1.3 *Amplitude- and phase-measurement without averaging.*
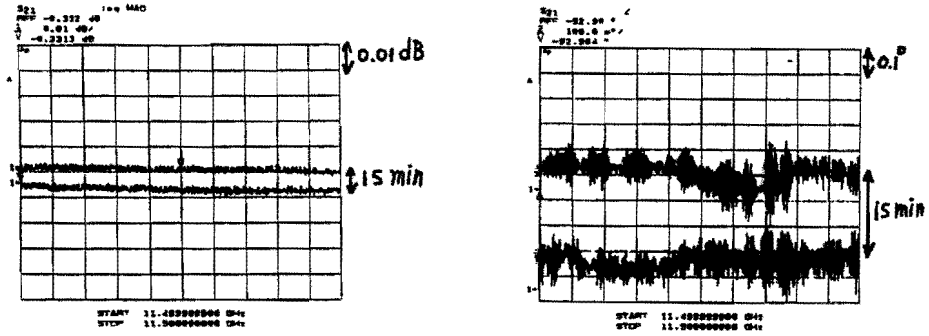
Figure A1.4 *Two amplitude- and phase-measurements using 64 averages and 15 minutes time-interval.*
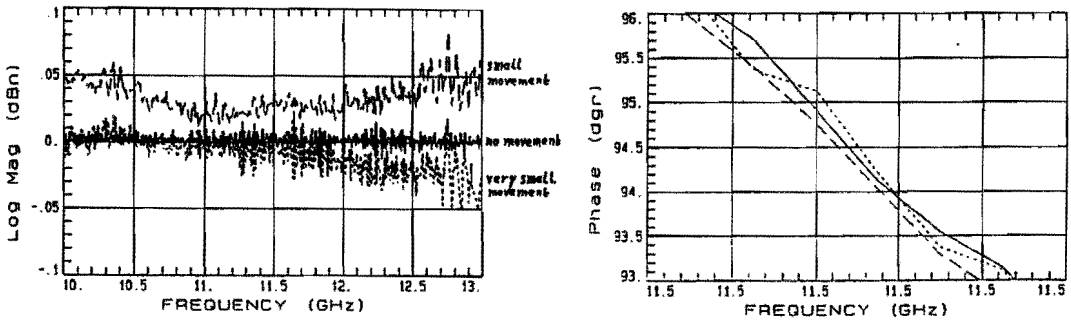
Figure A1.5 *Three amplitude- and phase-measurements illustrating the effect of small cable-movements.*
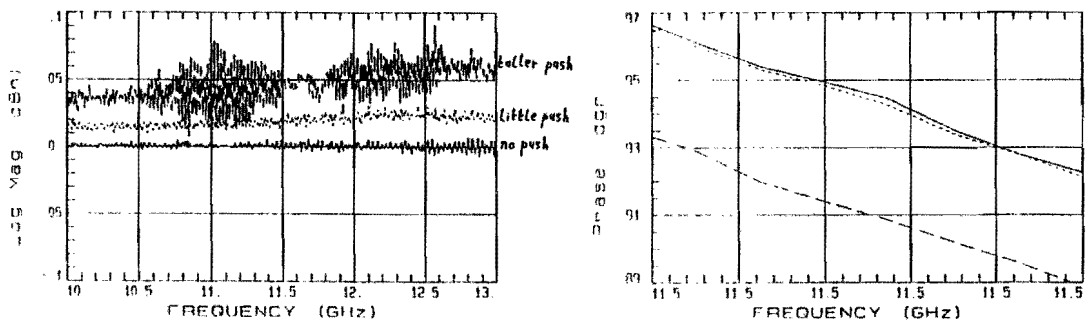
Figure A1.6 *Three amplitude- and phase-measurements illustrating the effect of shocks and vibrations.*
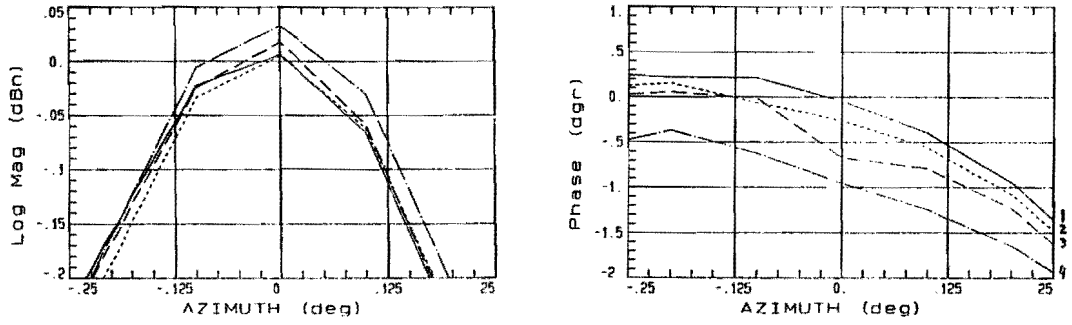
Figure A1.7 Amplitude- and phase-data of four azimuth-scans.

A.2 Preliminary measurements

All measurements performed with a 1.2m parabola in the H-plane.
On longitudinal distance scales: 1cm= 3mm in reality.
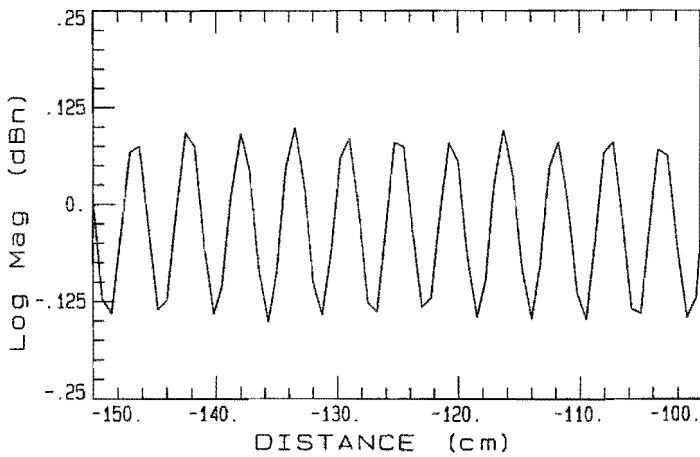
Figure A2.1 *Longitudinal scan, az= 0°, f=11.5 GHz.*
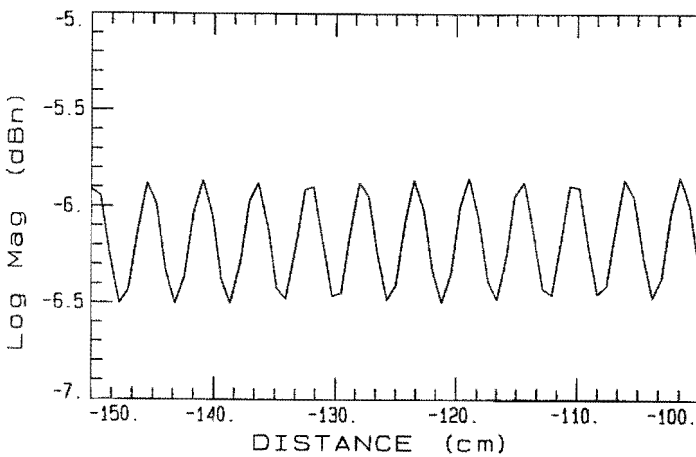
Figure A2.2 *Longitudinal scan, az= -1°, f=11.5 GHz.*
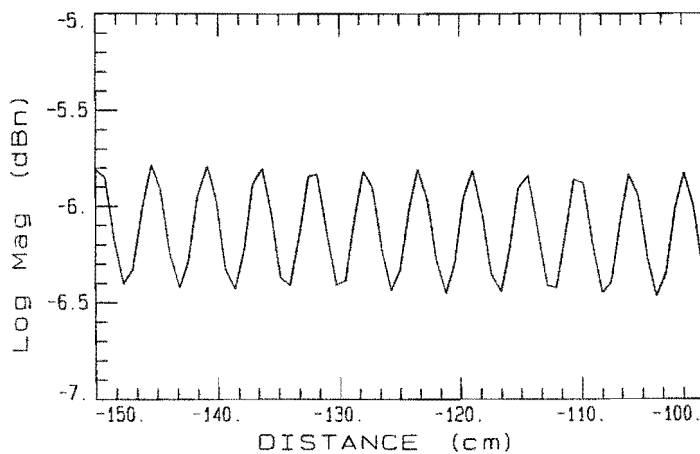
Figure A2.3 *Longitudinal scan, az= 1° , f=11.5 GHz.*
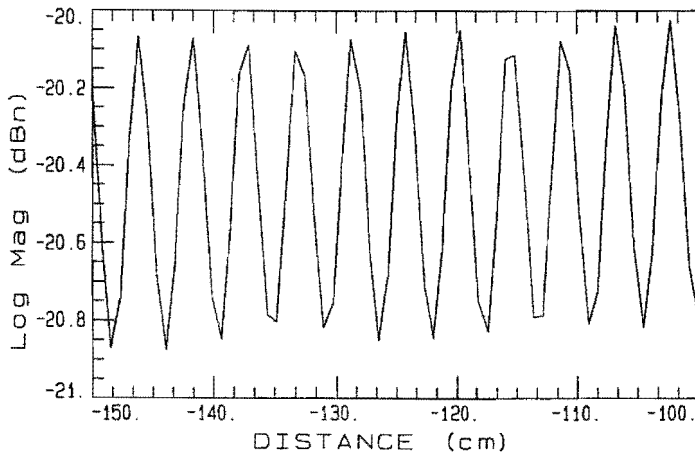
Figure A2.4 *Longitudinal scan, az= 2°, f=11.5 GHz.*
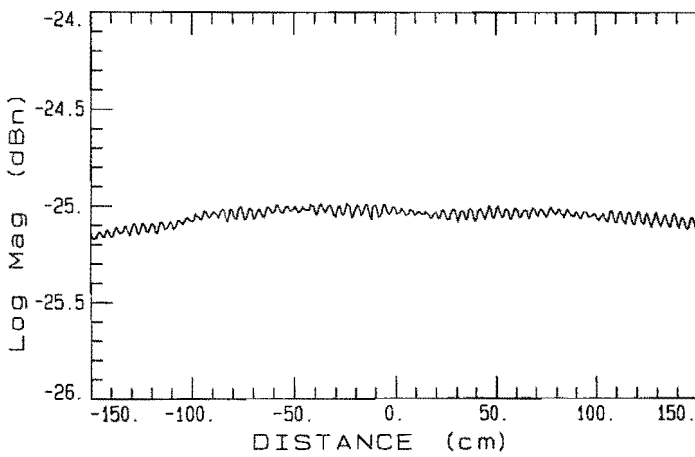
Figure A2.5 *Longitudinal scan, az= -4.5°, f=11.5 GHz.*
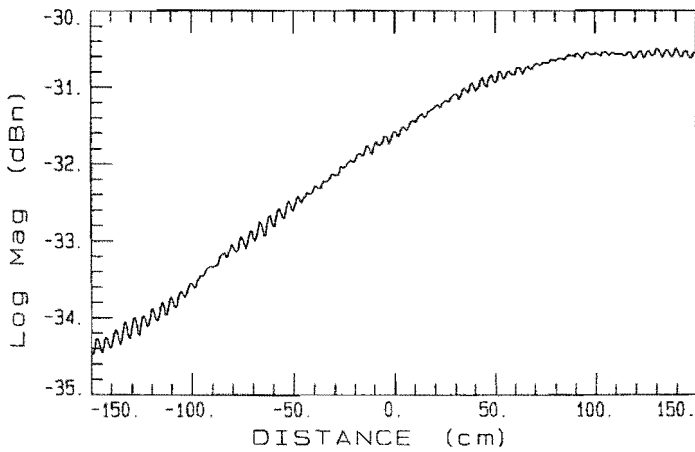
Figure A2.6 *Longitudinal scan, az= -9.5°, f=11.5 GHz.*
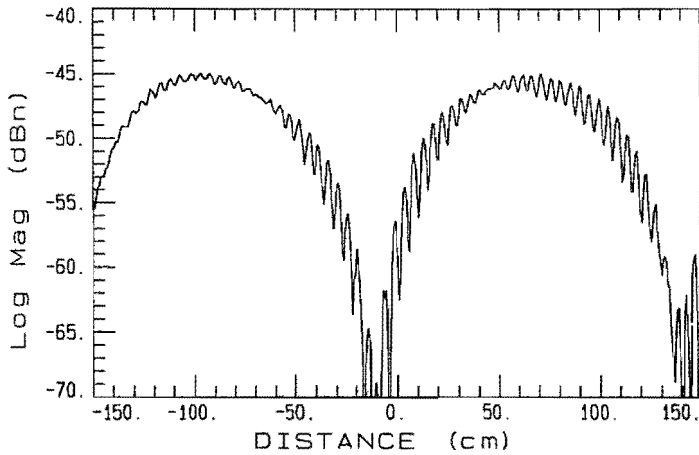
Figure A2.7 *Longitudinal scan, az= 20°, f=11.5 GHz.*
Range feed not masked, metal plate uncovered.
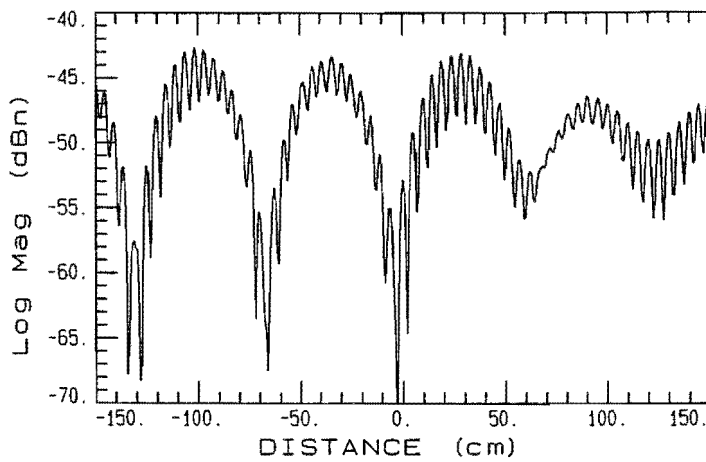
Figure A2.8 *Longitudinal scan, az= 30°, f=11.5 GHz.*
Range feed not masked, metal plate uncovered.
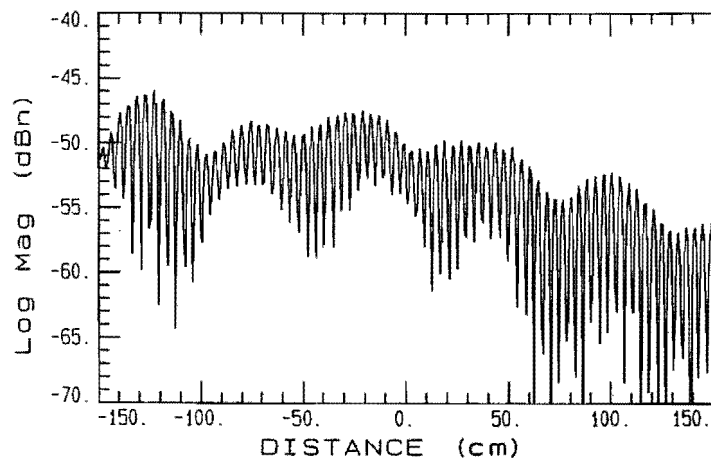
Figure A2.9 *Longitudinal scan, az= 30°, f=12.7 GHz.*
Range feed not masked, metal plate uncovered.
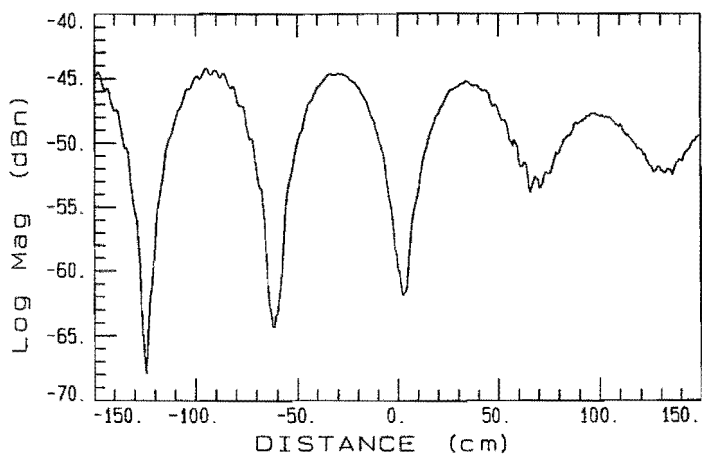
Figure A2.10 *Longitudinal scan, az= 30°, f=11.5 GHz.*
Range feed not masked, metal plate covered.
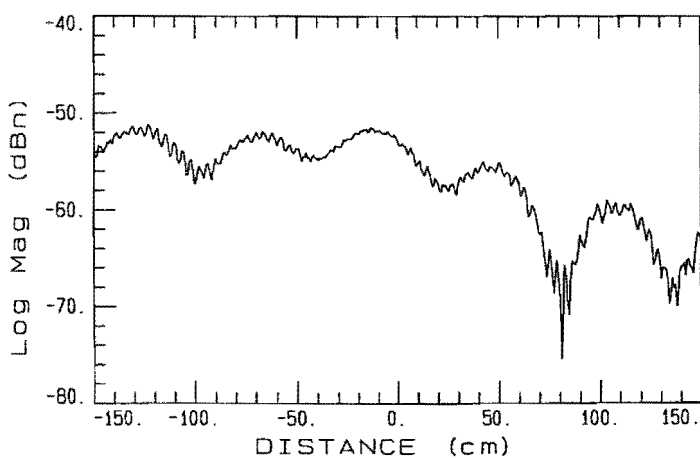
Figure A2.11 *Longitudinal scan, az= 30°, f=12.7 GHz.*
Range feed not masked, metal plate covered.
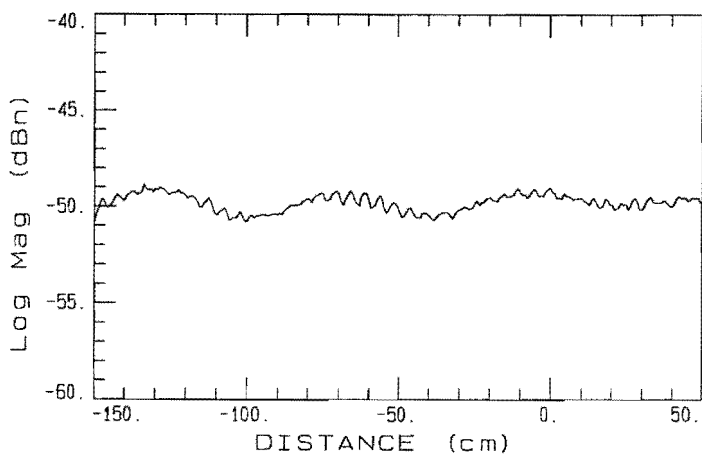
Figure A2.12 *Longitudinal scan, az= 30°, f=11.5 GHz.*
Range feed masked, metal plate covered.
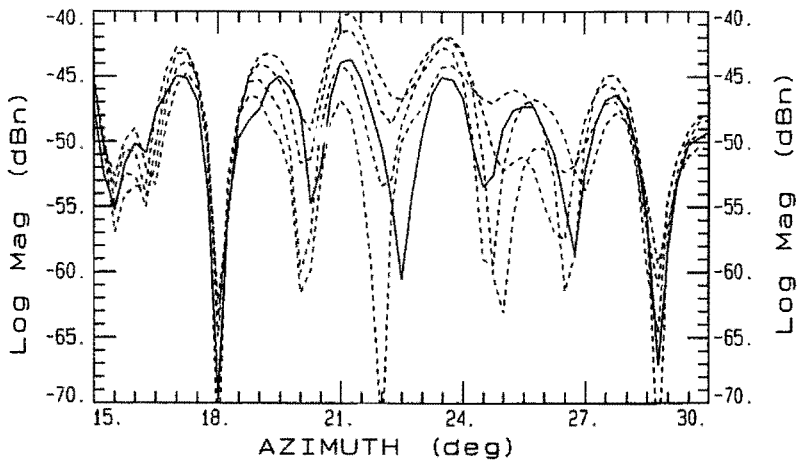
Figure A2.13 *Azimuth-scans, amplitude, f=11.5 GHz, cont.line: corrected, dot.line: measured.*
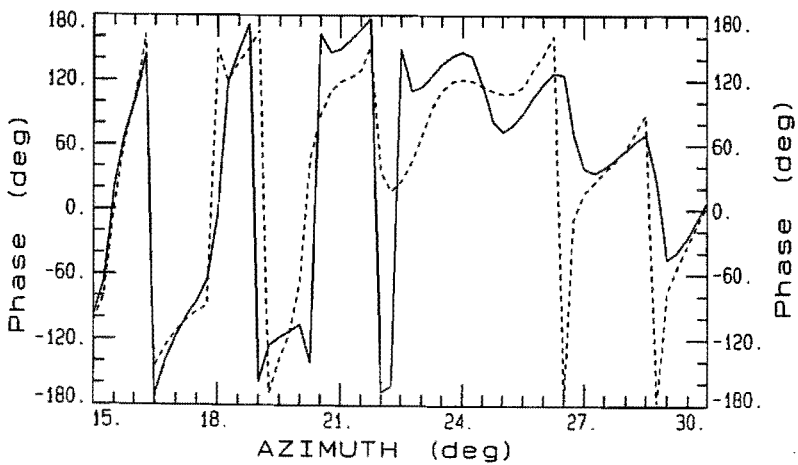
Figure A2.14 *Azimuth-scans, phase, f=11.5 GHz, cont.line: corrected, dot.line: measured.*
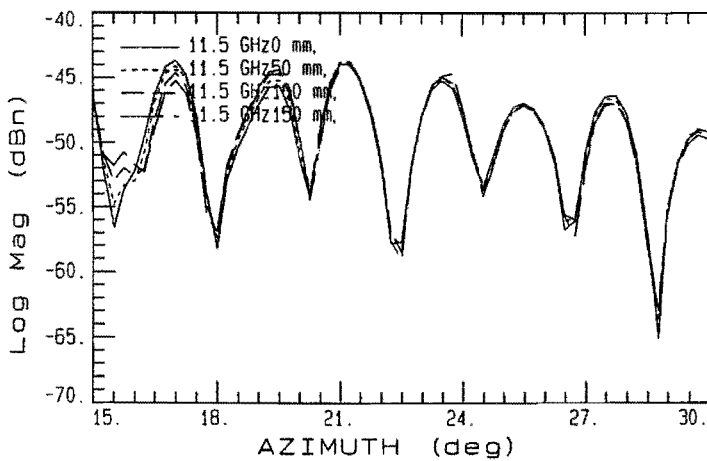
Figure A2.15 *Azimuth-scans, amplitude, f=11.5 GHz, 4 gated measurements.*
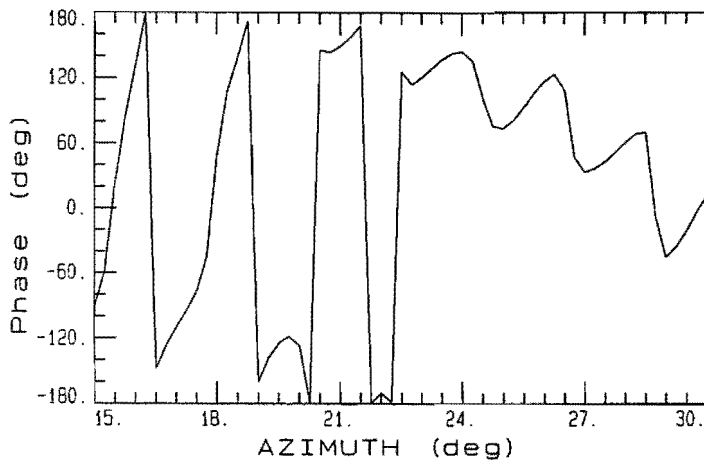
Figure A2.16 *Azimuth-scan, phase, f=11.5 GHz, gated measurement in first plane.*
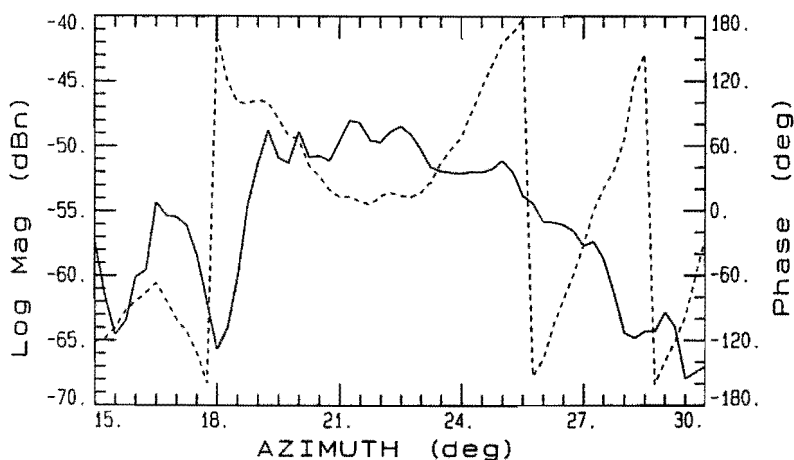
Figure A2.17 *Azimuth-scan, residual component, f=11.5GHz, cont.line: amplitude, dot.line: phase.*
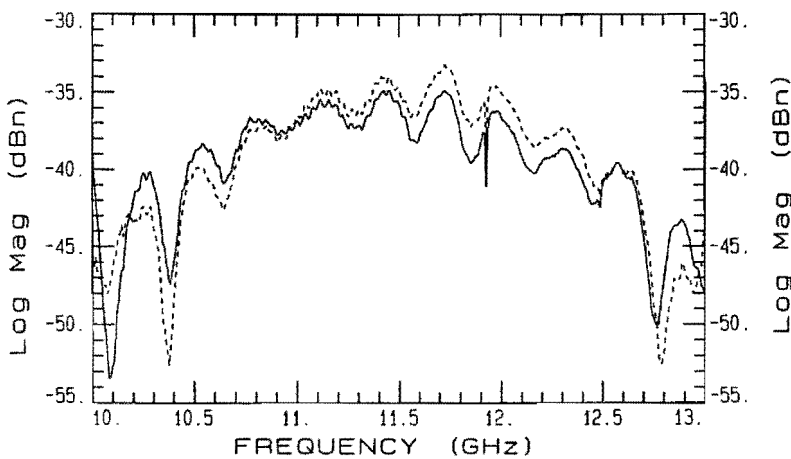
Figure A2.18 *Power vs. frequency, amplitude, az= -9°, cont.line: corrected, dot.line: first measurement.*
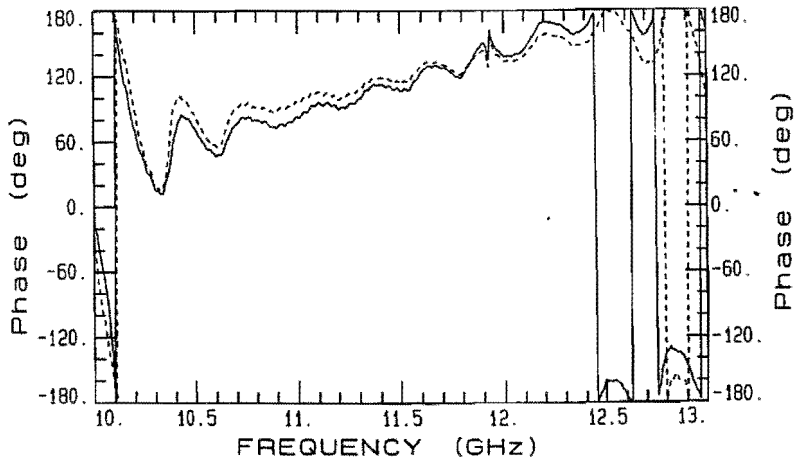
Figure A2.19 *Power vs. frequency, phase, az= -9°, cont.line: corrected, dot.line: first measurement.*
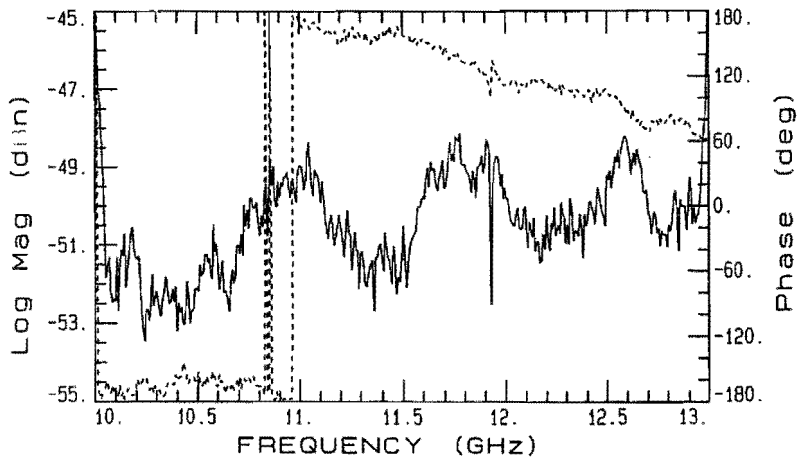
Figure A2.20 *Power vs. frequency, residual component, az= -9°, cont.line: amplitude, dot.line: phase.*

A.3 1.2m-parabola

On longitudinal distance scales: 1cm= 3mm in reality.
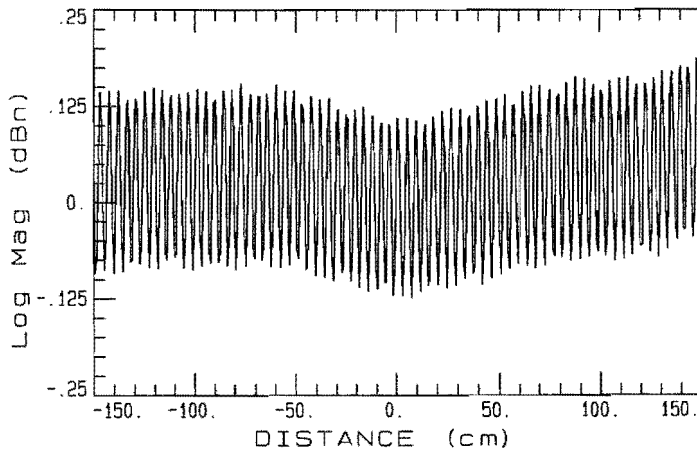
Figure A3.1 *Longitudinal scan, H-plane, az= 0°, f=11.5 GHz.*
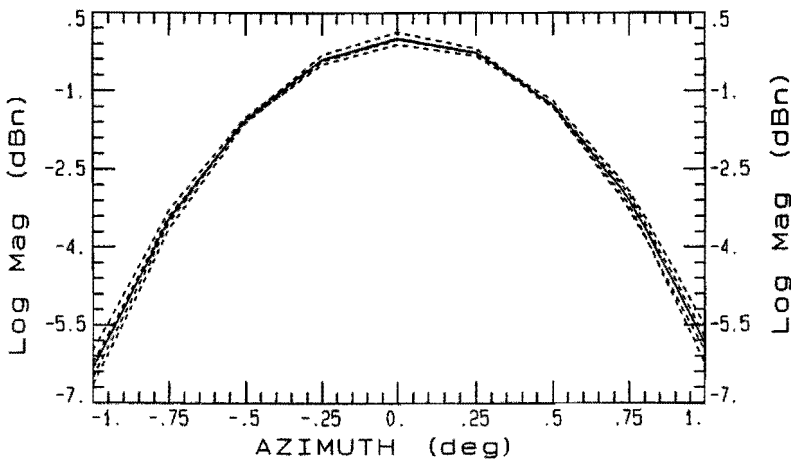
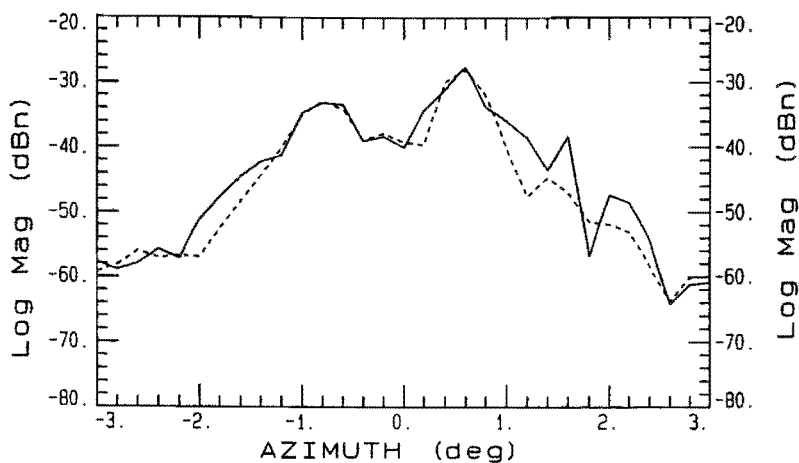**Figure A3.2** *Azimuth scan, amplitude, H-plane, f=11.5 GHz, cont.line: corrected, dot.line: measured.*
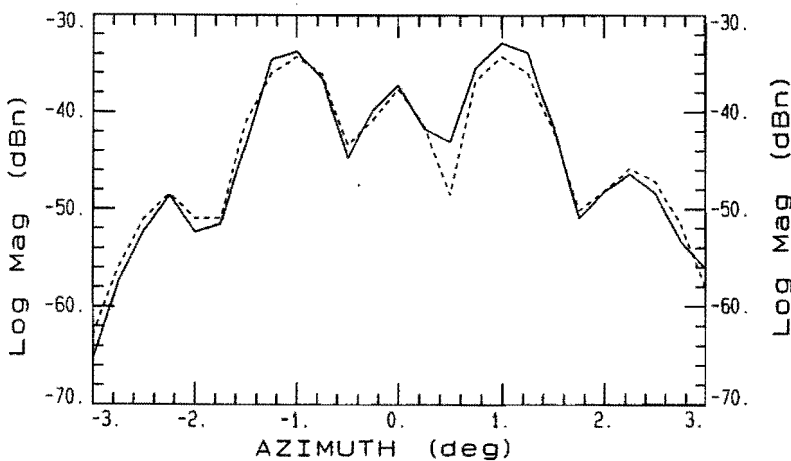
Figure A3.3 *Azimuth scan, mutual coupling component, H-plane, f=11.5 GHz, cont.line: novel APC, dot.line: gated.*
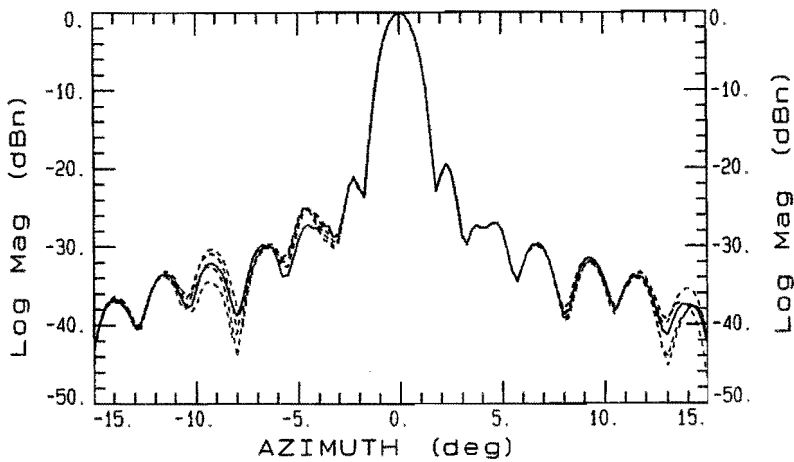
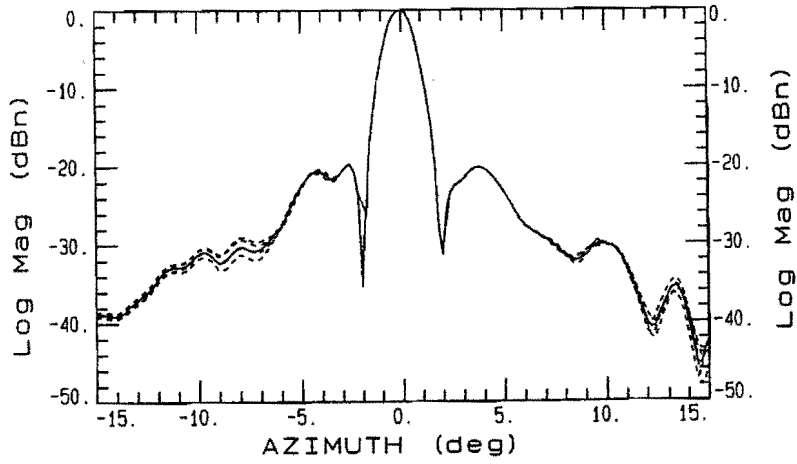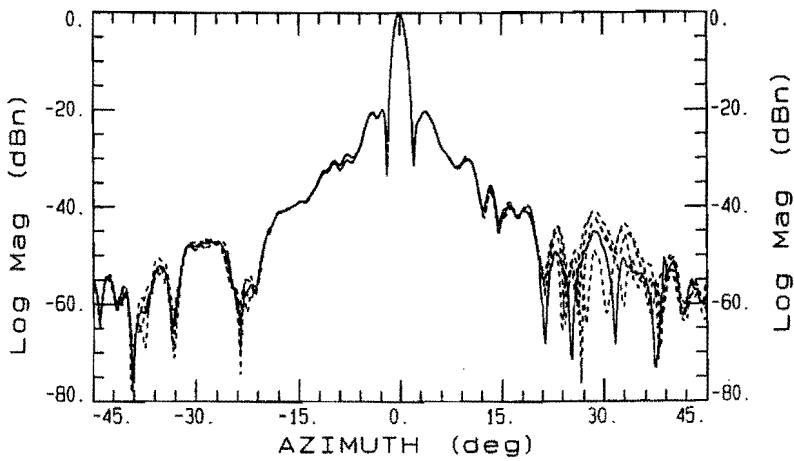**Figure A3.4** *Azimuth scan, amplitude, H-plane, f=11.5 GHz, cont.line: corrected, dot.line: measured.*
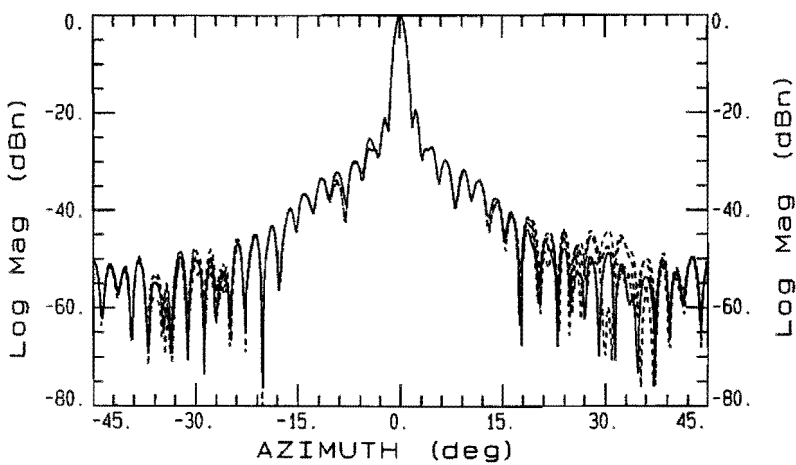
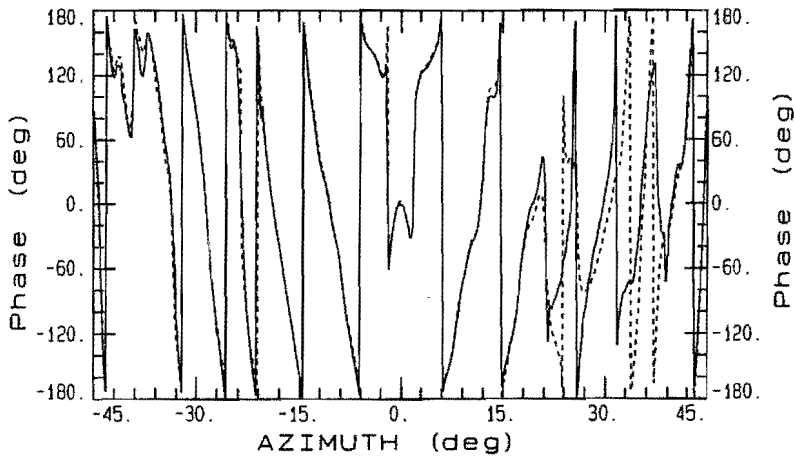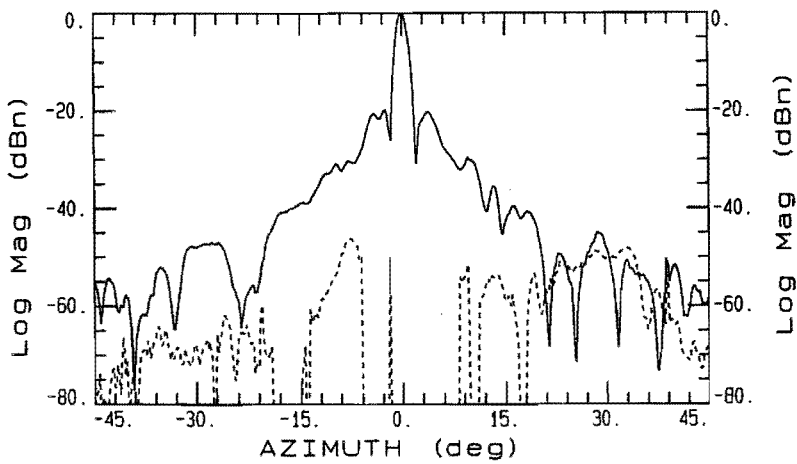**Figure A3.5** *Azimuth scan, amplitude, H-plane, f=11.5 GHz, cont.line: corrected, dot.line: measured.*
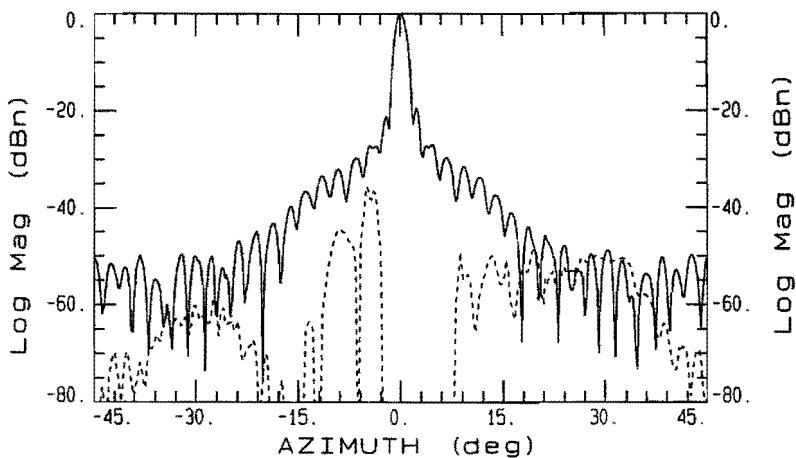
Figure A3.6 *Azimuth scan, amplitude, H-plane, f=11.5 GHz, cont.line: corrected, dot.line: residual component.*

98
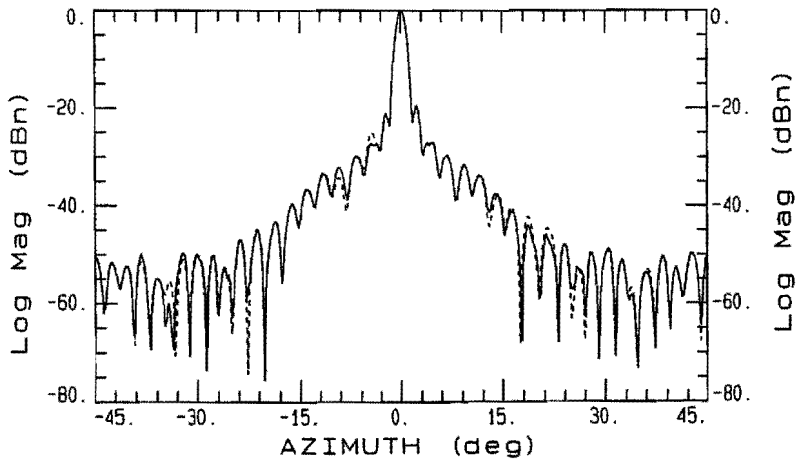
Figure A3.7 *Azimuth scan, amplitude, H-plane, f=11.5 GHz, cont.line: novel APC, dot.line: gated.*
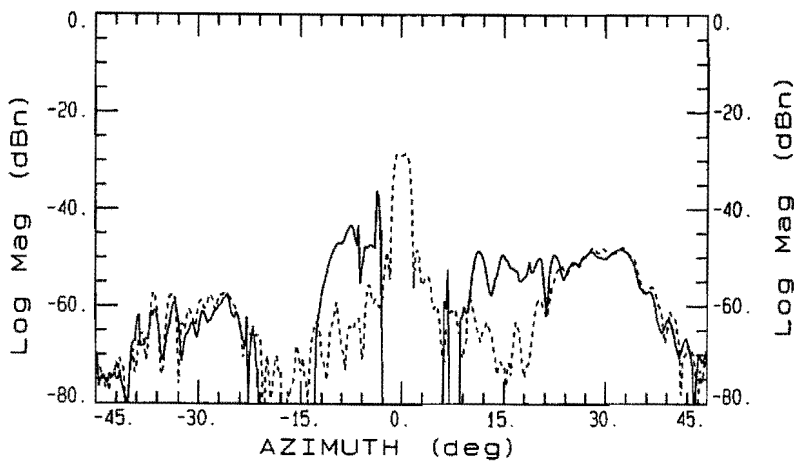
Figure A3.8 *Azimuth scan, residual component, H-plane, f=10.6 GHz, cont.line: novel APC, dot.line: gated.*
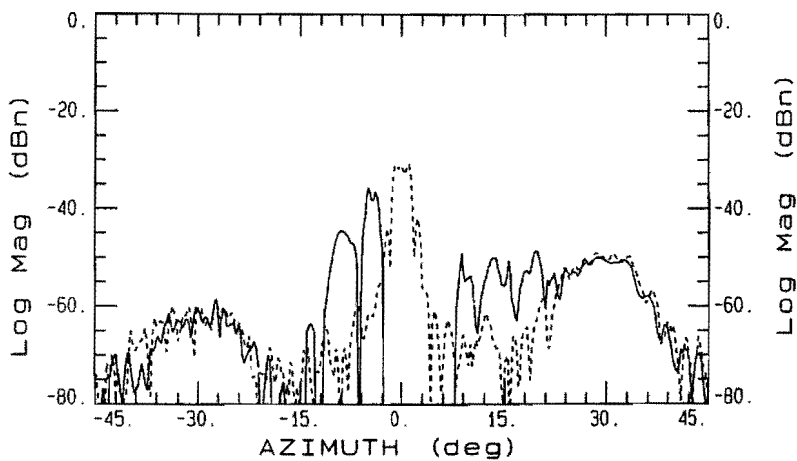
Figure A3.9 *Azimuth scan, residual component, H-plane, f=11.5 GHz, cont.line: novel APC, dot.line: gated.*
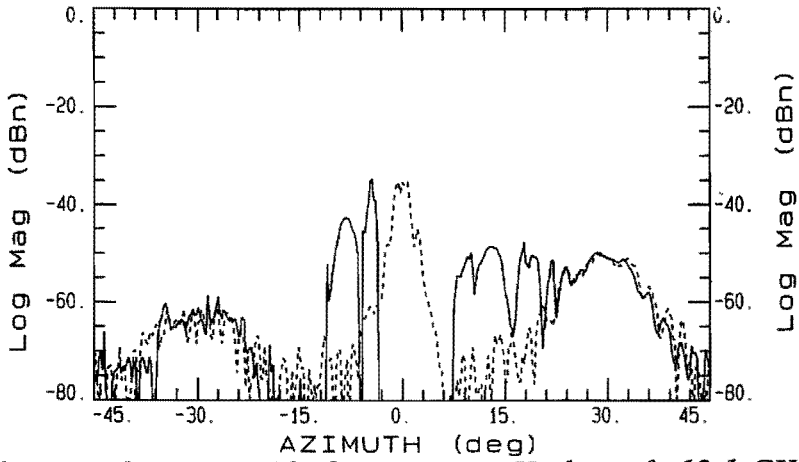
Figure A3.10 *Azimuth scan, residual component, H-plane, f=12.1 GHz, cont.line: novel APC, dot.line: gated.*
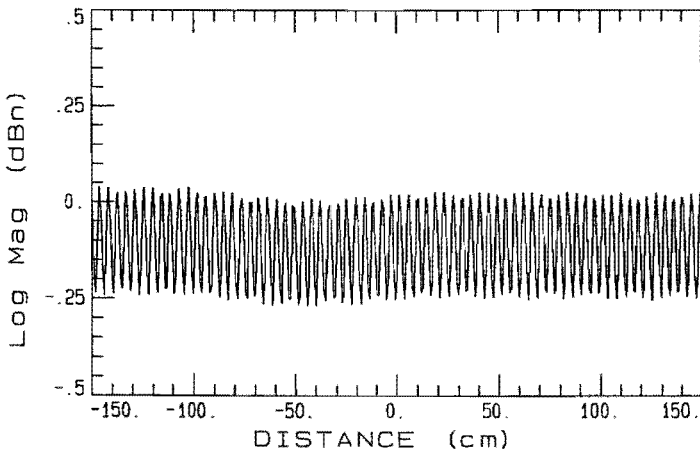
Figure A3.11 *Longitudinal scan, 45°-plane c, az= 0°, f=11.5 GHz.*
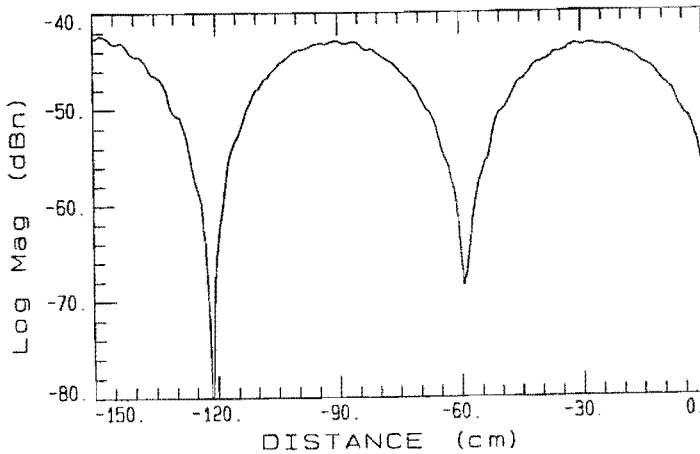
Figure A3.12 *Longitudinal scan, 45°-plane c, az= 30°, f=11.5 GHz.*
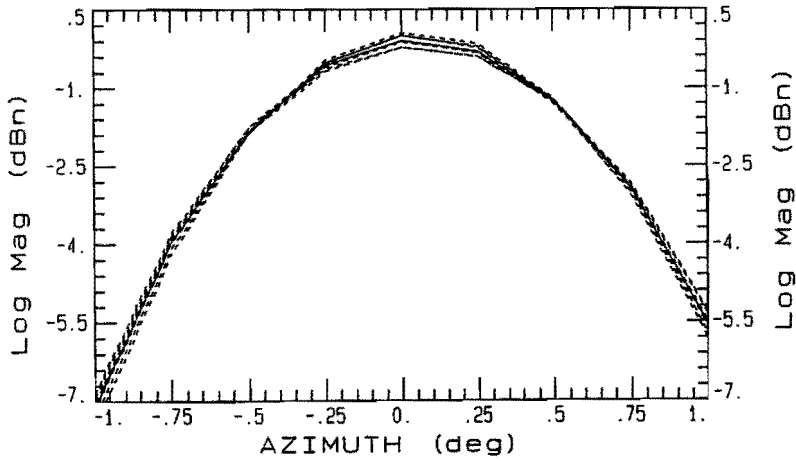
Figure A3.13 *Azimuth scan, amplitude, 45°-plane c, f=11.5 GHz, cont.line: corrected, dot.line: measured.*
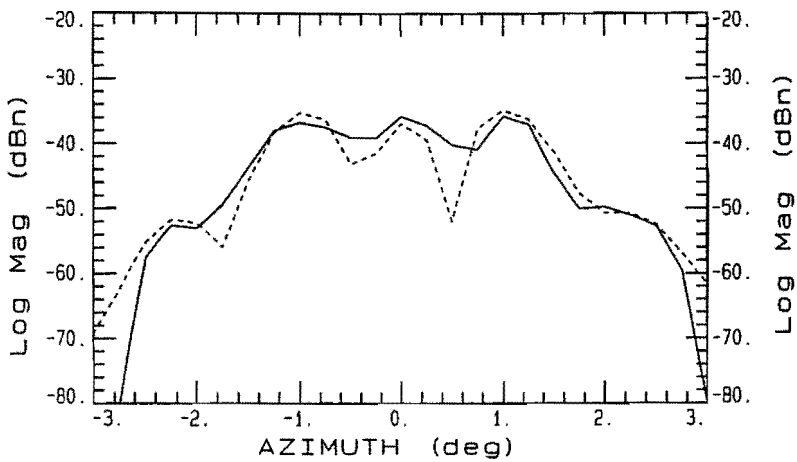
Figure A3.14 *Azimuth scan, mutual coupling component, 45°-plane c, f=11.5 GHz, cont.line: novel APC, dot.line: gated.*
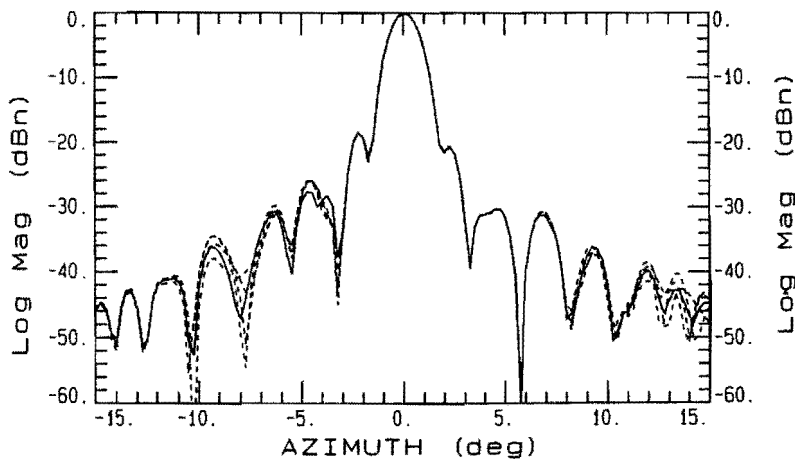
Figure A3.15 *Azimuth scan, amplitude, 45°-plane c, f=11.5 GHz, cont.line: corrected, dot.line: measured.*
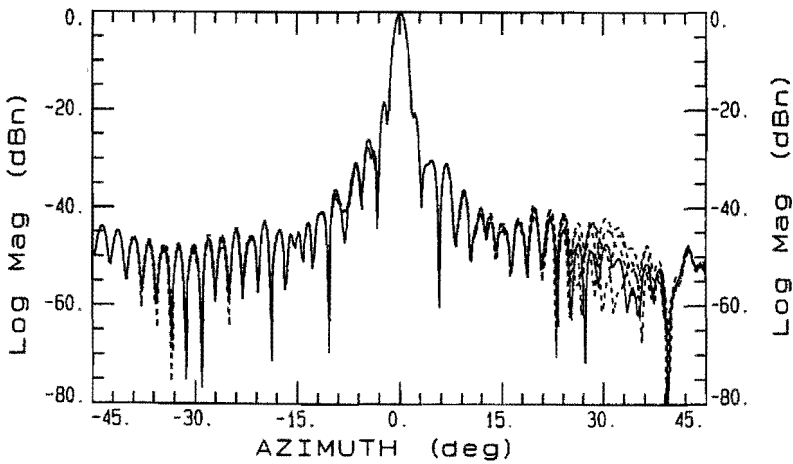
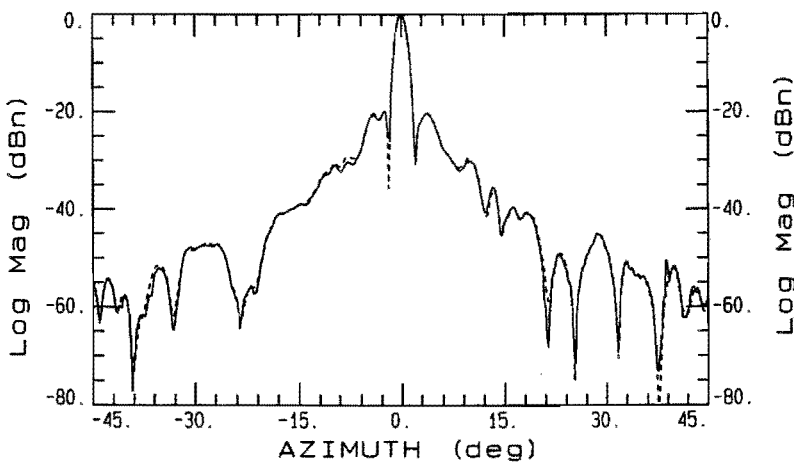**Figure A3.16** *Azimuth scan, amplitude, 45°-plane c, f=11.5 GHz, cont.line: corrected, dot.line: measured.*
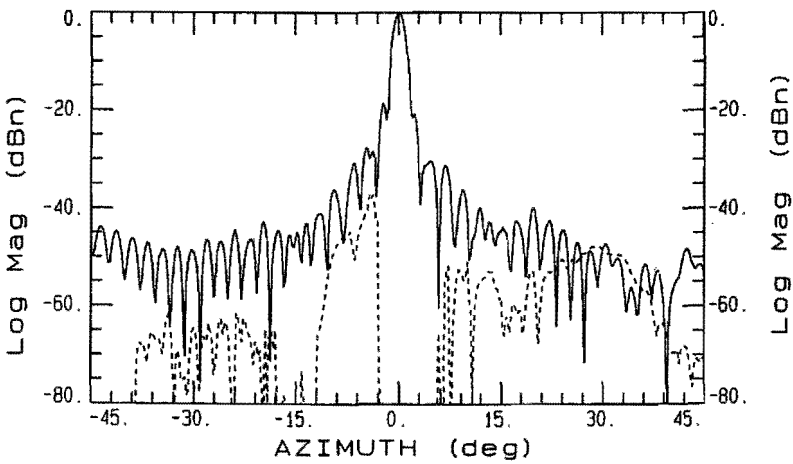
Figure A3.17 *Azimuth scan, amplitude, 45°-plane c, f=11.5 GHz, cont.line: corrected, dot.line: residual component.*
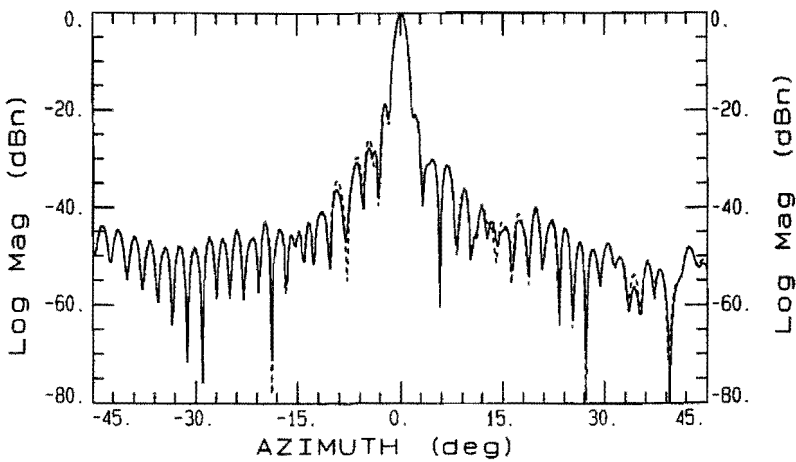
Figure A3.18 *Azimuth scan, amplitude, 45°-plane c, f=11.5 GHz, cont.line: novel APC, dot.line: gated.*
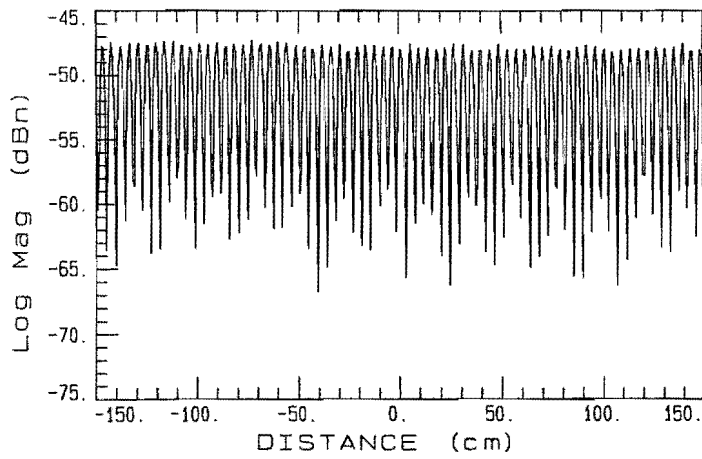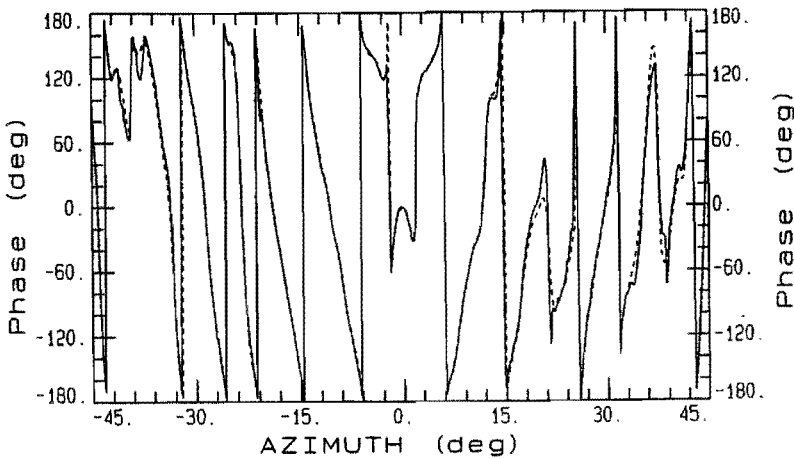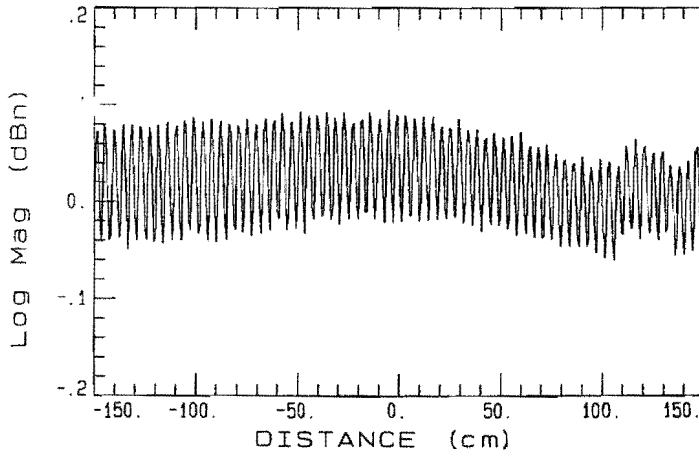
Figure A3.19 *Longitudinal scan, 45°-plane x, az= 0°, f=11.5 GHz.*
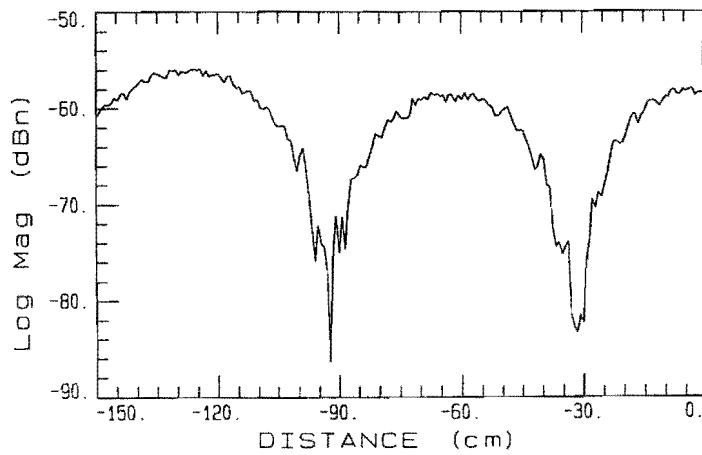
Figure A3.20 *Longitudinal scan, 45°-plane x, az= 30°, f=11.5 GHz.*
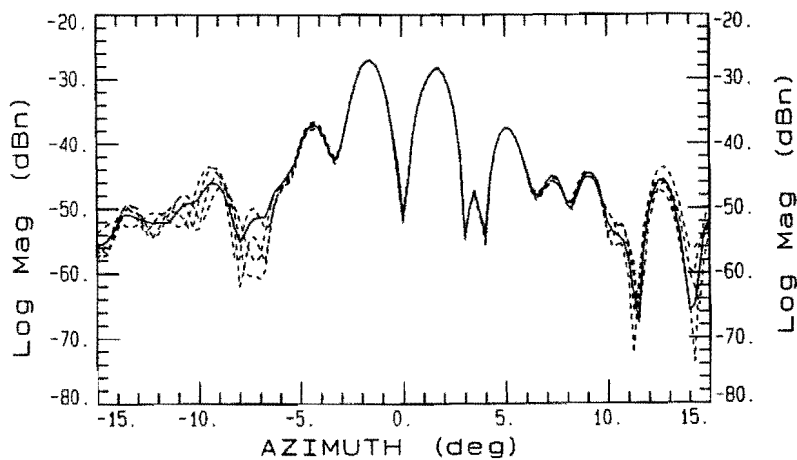
Figure A3.21 *Azimuth scan, amplitude, 45°-plane x, f=11.5 GHz, cont.line: corrected, dot.line: measured.*
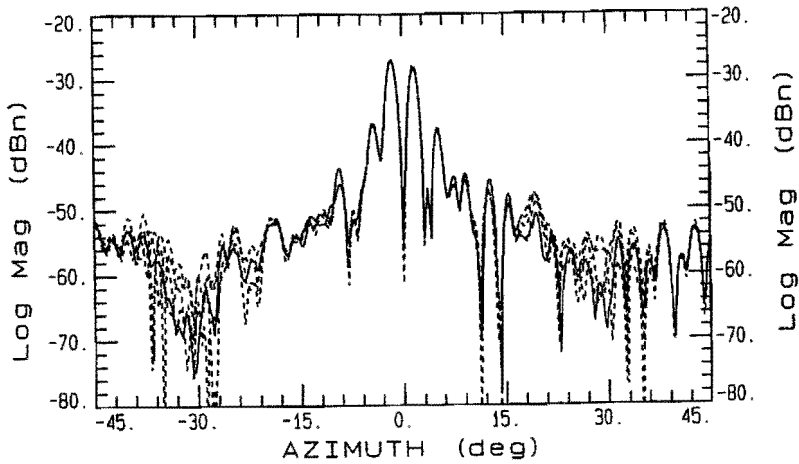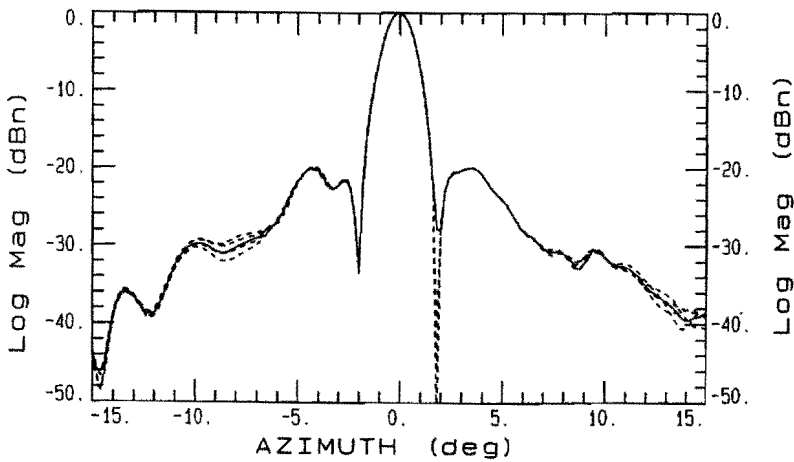
Figure A3.22 *Azimuth scan, amplitude, 45°-plane x, f=11.5 GHz, cont.line: corrected, dot.line: measured.*
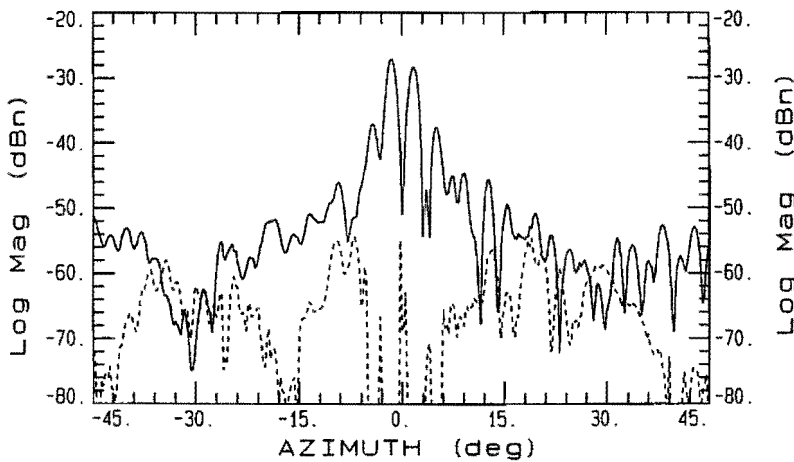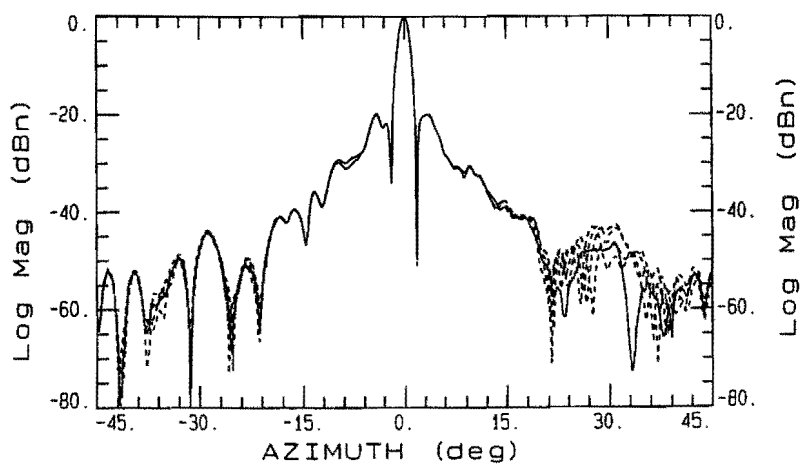

Figure A3.23 *Azimuth scan, amplitude, 45°-plane x, f=11.5 GHz, cont.line: corrected, dot.line: residual component.*
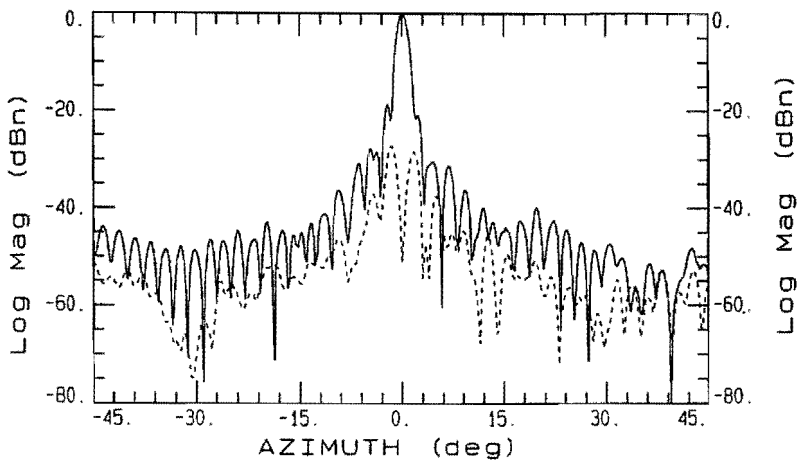
Figure A3.24 *Azimuth scan, corrected, f=11.5 GHz, cont.line: 45°-plane c, dot.line: 45°-plane x.*
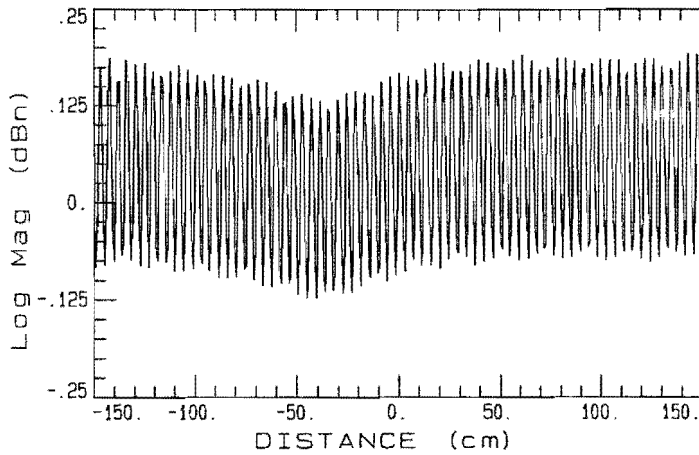
Figure A3.25 *Longitudinal scan, E-plane, az= 0°, f=11.5 GHz.*
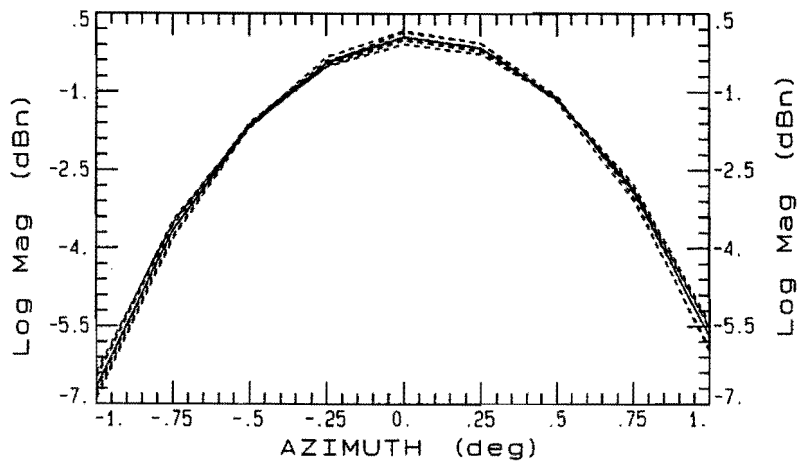
Figure A3.26 *Azimuth scan, amplitude, E-plane, f=11.5 GHz, cont.line: corrected, dot.line: measured.*
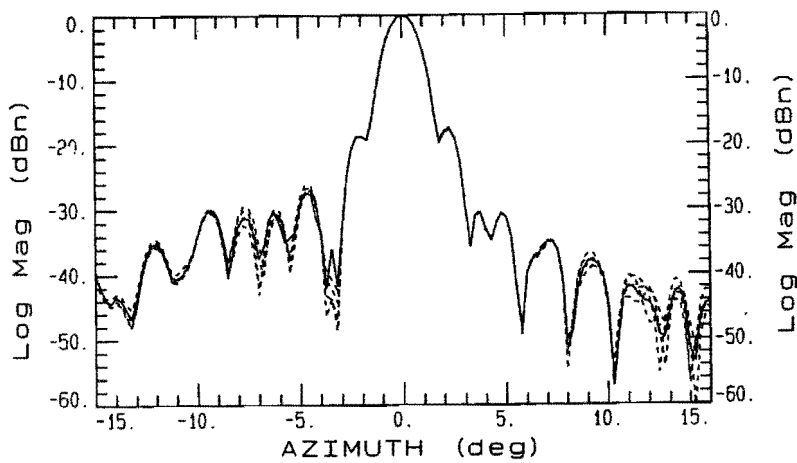
Figure A3.27 *Azimuth scan, amplitude, E-plane, f=11.5 GHz, cont.line: corrected, dot.line: measured.*
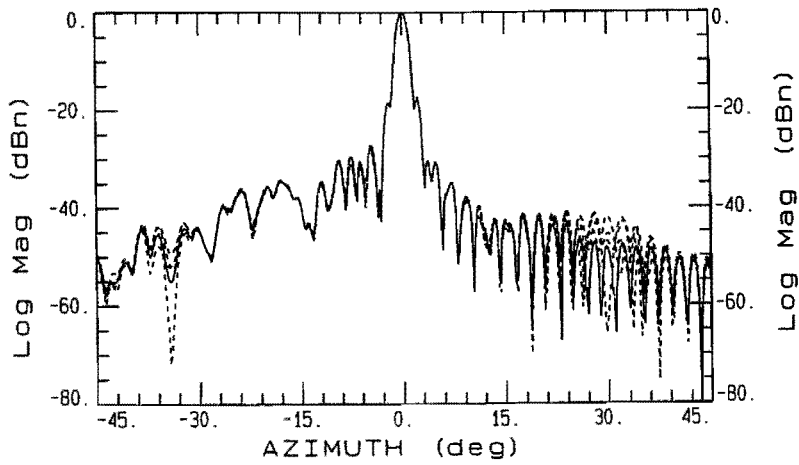
Figure A3.28 *Azimuth scan, amplitude, E-plane, f=11.5 GHz, cont.line: corrected, dot.line: measured.*
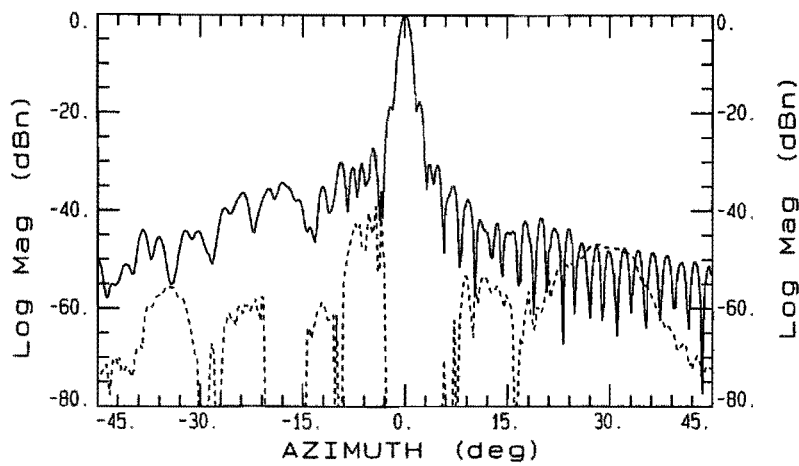
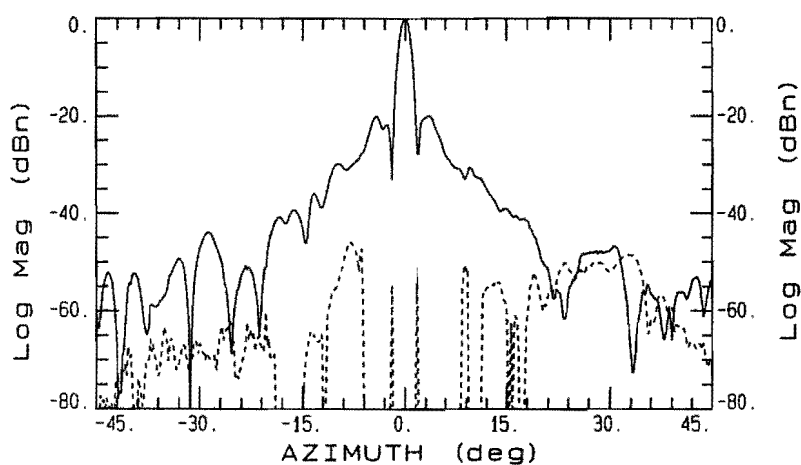**Figure A3.29** *Azimuth scan, amplitude, E-plane, f=11.5 GHz, cont.line: corrected, dot.line: residual component.*

A.4 2m-parabola

On longitudinal distance scales: 1cm= 3mm in reality.
up= antenna not rotated around its mechanical axis
down= antenna rotated 180° around its mechanical axis
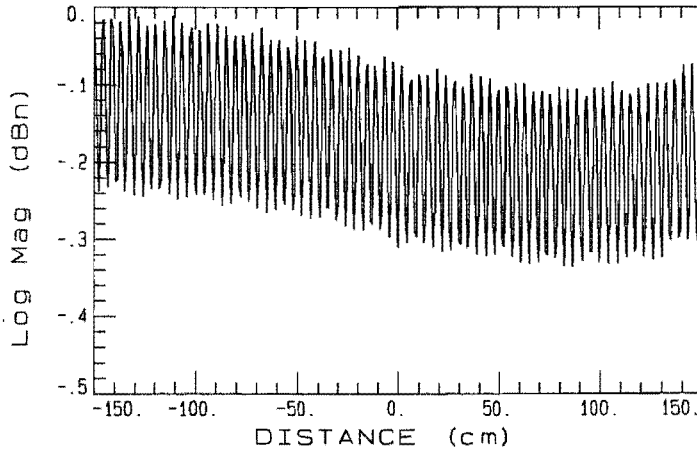
Figure A4.1 *Longitudinal scan, H-plane, up, az= 0°, f=11.5 GHz.*
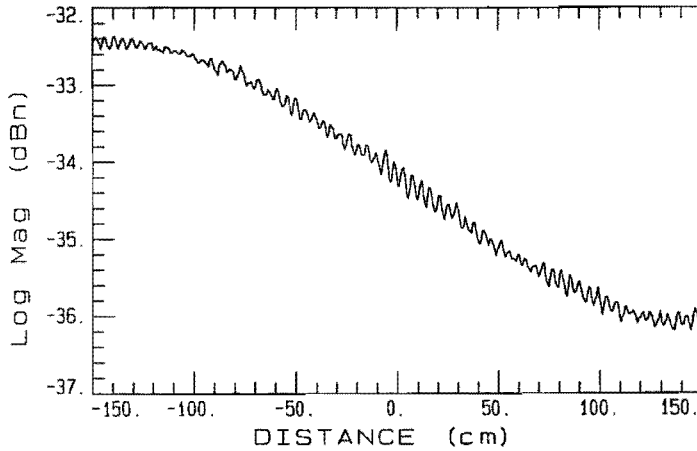
Figure A4.2 *Longitudinal scan, H-plane, up, az= -9.5°, f=11.5 GHz.*
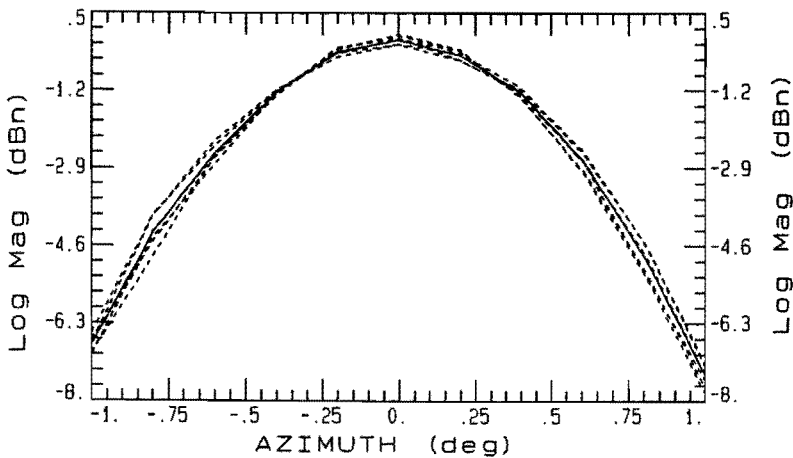
Figure A4.3 *Azimuth scan, amplitude, H-plane, up, f=11.5 GHz, cont.line: corrected, dot.line: measured.*
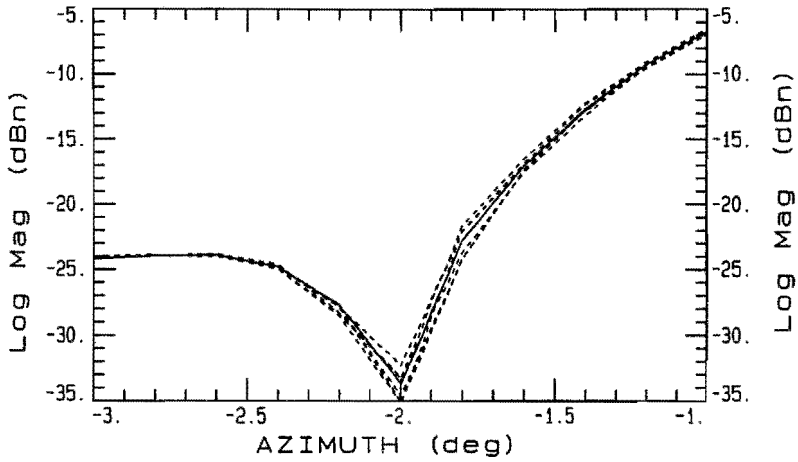
Figure A4.4 *Azimuth scan, amplitude, H-plane, up, f=11.5 GHz, cont.line: corrected, dot.line: measured.*
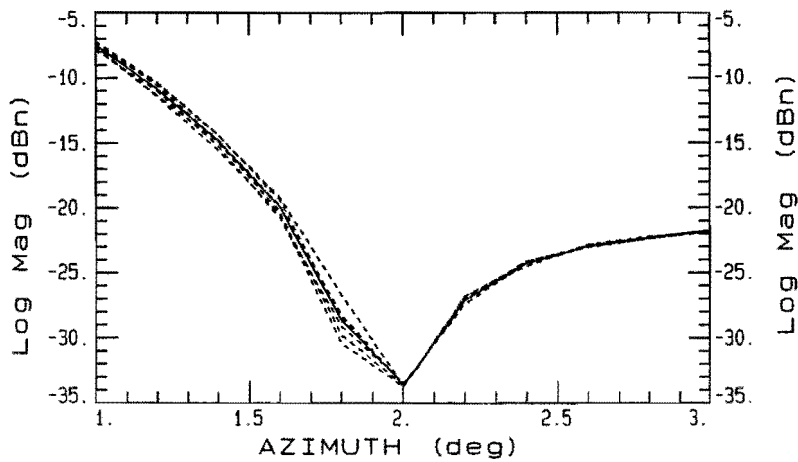
Figure A4.5 *Azimuth scan, amplitude, H-plane, up, f=11.5 GHz, cont.line: corrected, dot.line: measured.*
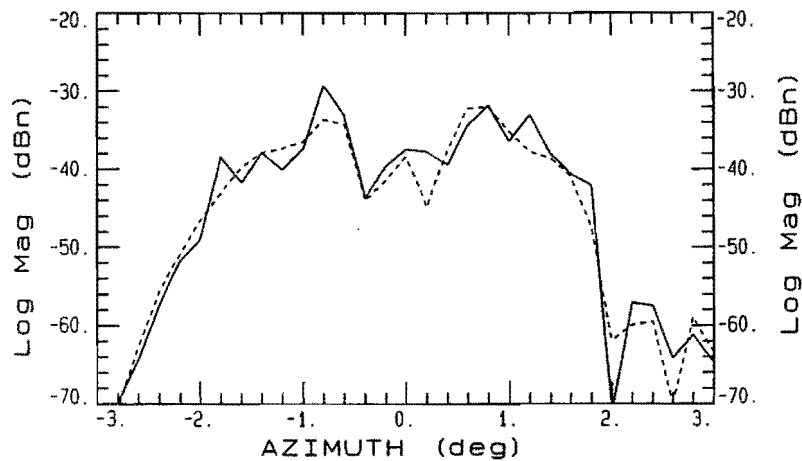
Figure A4.6 *Azimuth scan, mutual coupling component, H-plane, up, f=11.5 GHz, cont.line: novel APC, dot.line: gated.*
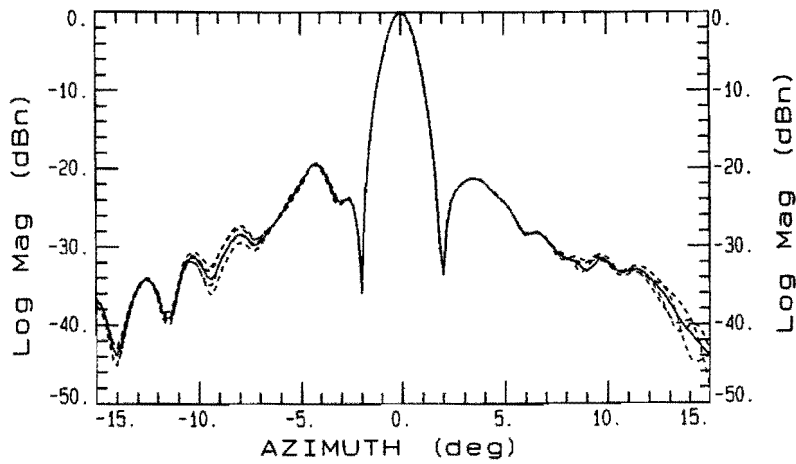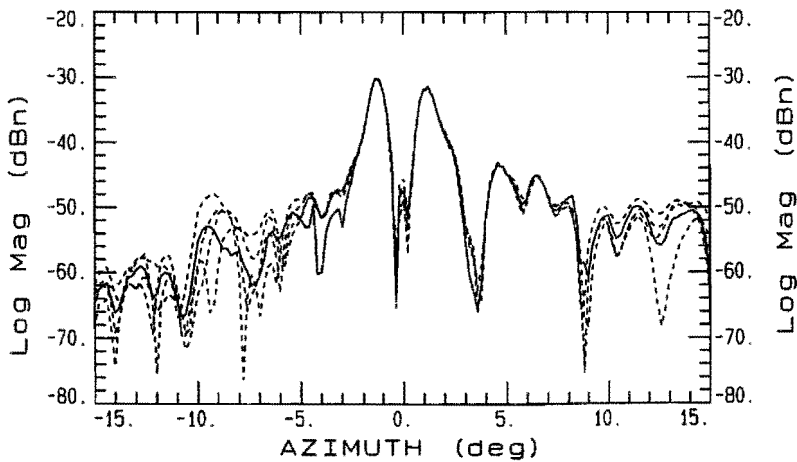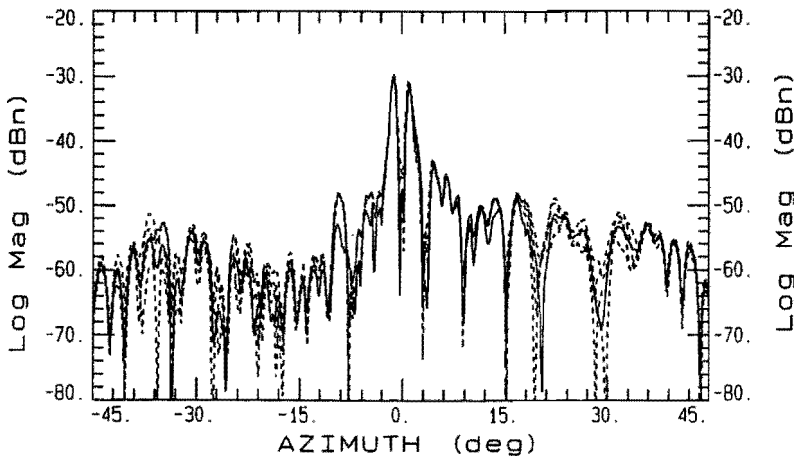
Figure A4.7 *Azimuth scan, amplitude, H-plane, up, f=11.5 GHz, cont.line: corrected, dot.line: measured.*
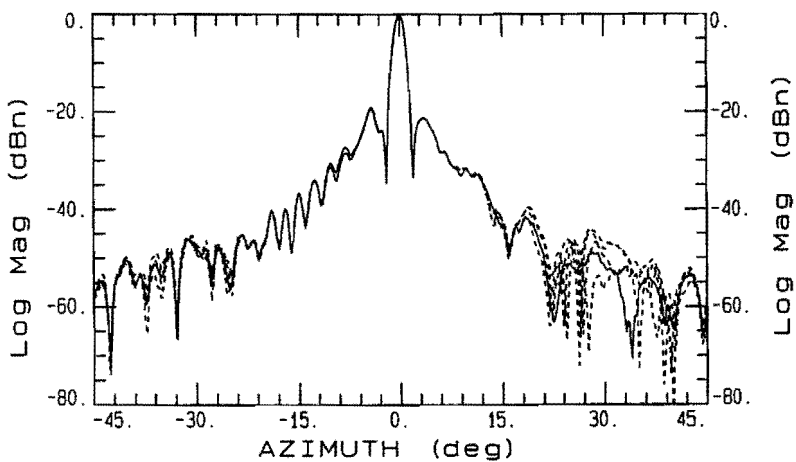
Figure A4.8 *Azimuth scan, amplitude, H-plane, up, f=11.5 GHz, cont.line: corrected, dot.line: measured.*
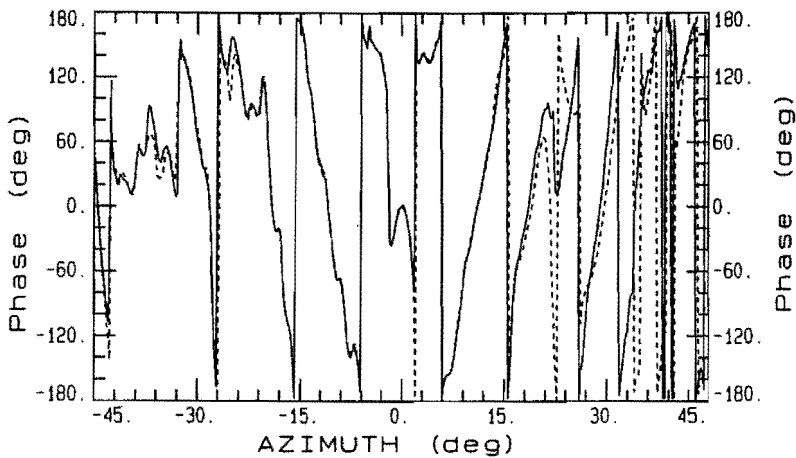
Figure A4.9 *Azimuth scan, phase, H-plane, up, f=11.5 GHz, cont.line: corrected, dot.line: measured.*
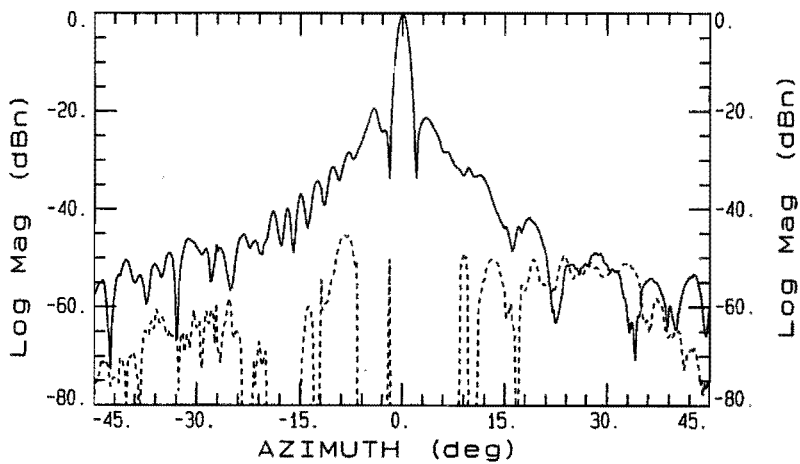
Figure A4.10 *Azimuth scan, amplitude, H-plane, up, f=11.5 GHz, cont.line: corrected, dot.line: residual component.*
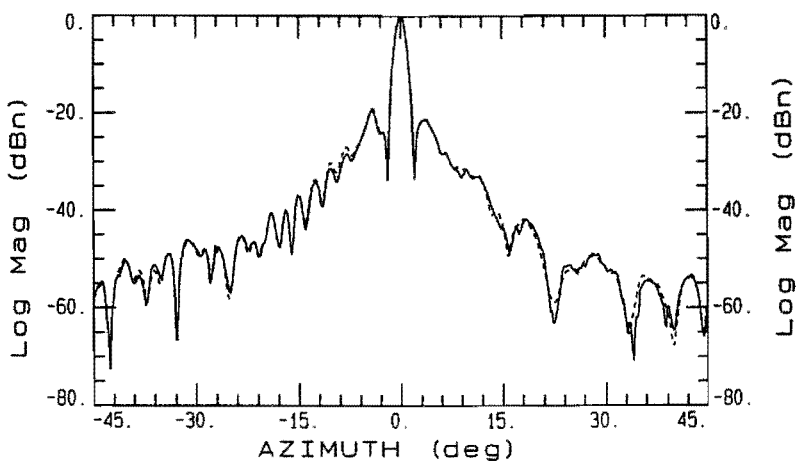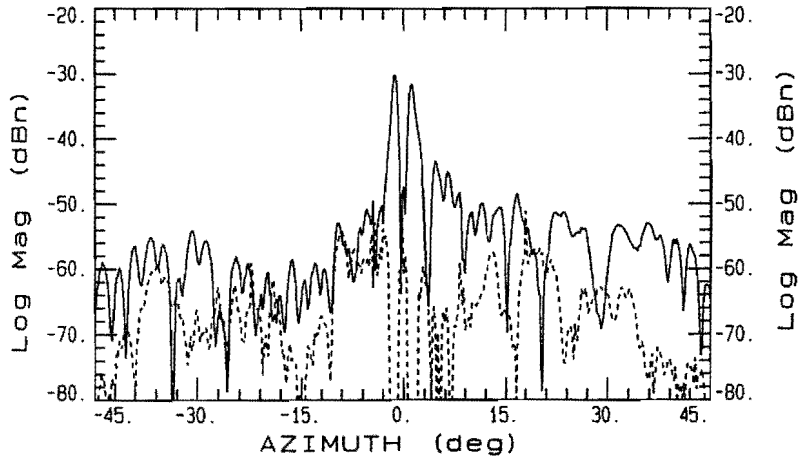

Figure A4.11 *Azimuth scan, amplitude, H-plane, up, f=11.5 GHz, cont.line: novel APC, dot.line: gated.*
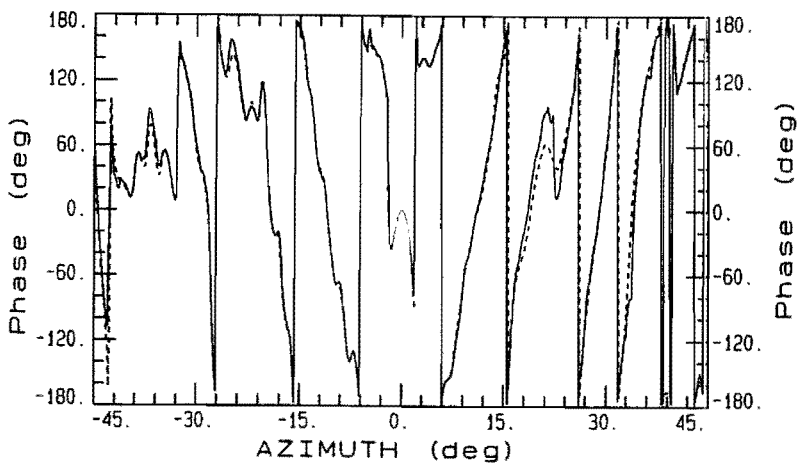
Figure A4.12 *Azimuth scan, phase, H-plane, up, f=11.5 GHz, cont.line: novel APC, dot.line: gated.*
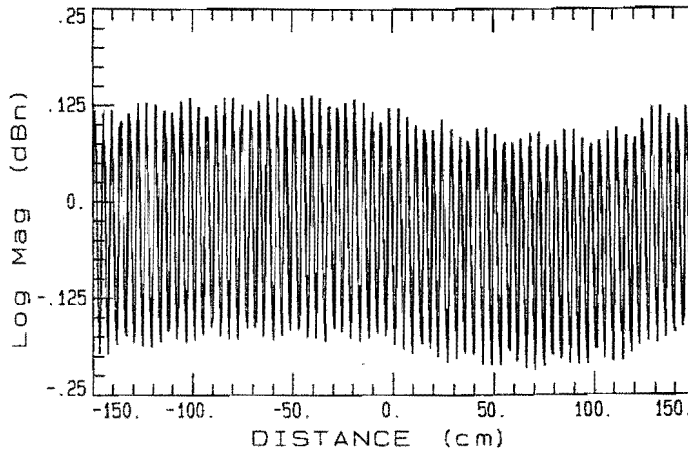
Figure A4.13 *Longitudinal scan, H-plane, down, az= 0°, f=11.5 GHz.*
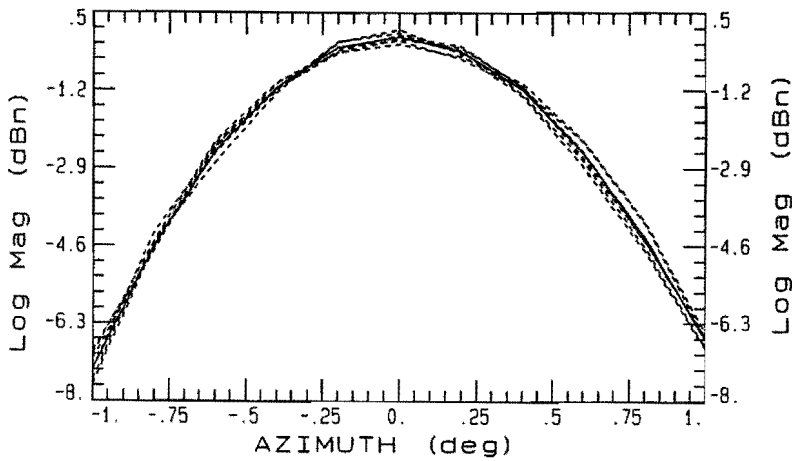
Figure A4.14 *Azimuth scan, amplitude, H-plane, down, f=11.5 GHz, cont.line: corrected, dot.line: measured.*
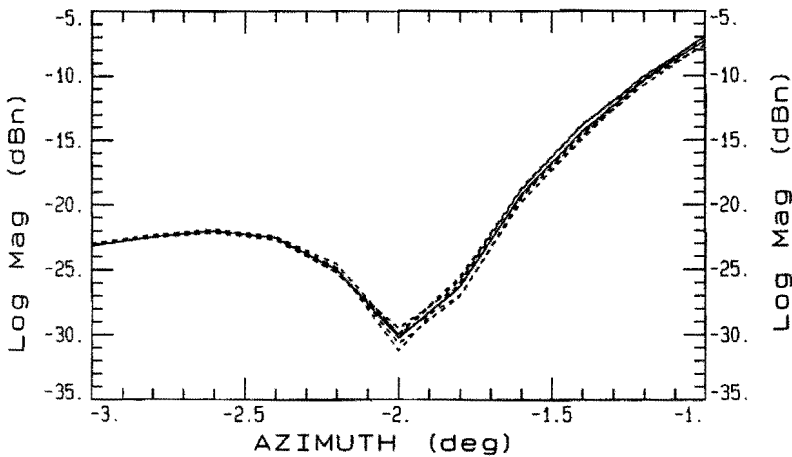
Figure A4.15 *Azimuth scan, amplitude, H-plane, down, f=11.5 GHz, cont.line: corrected, dot.line: measured.*
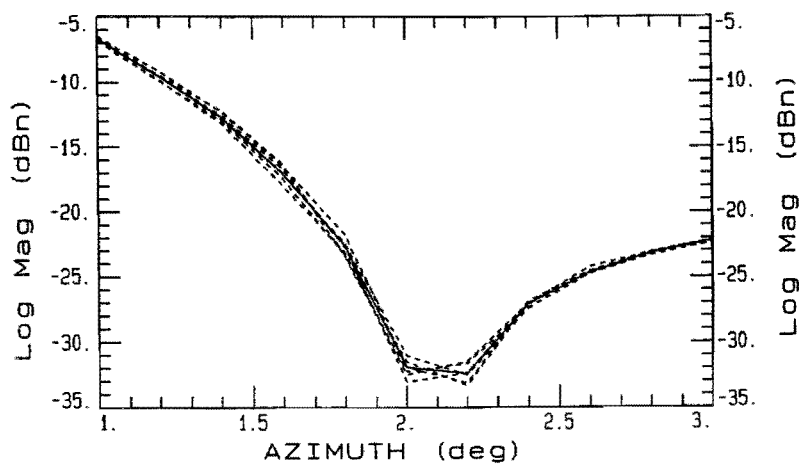
Figure A4.16 Azimuth scan, amplitude, H-plane, down, f=11.5 GHz, cont.line: corrected, dot.line: measured.
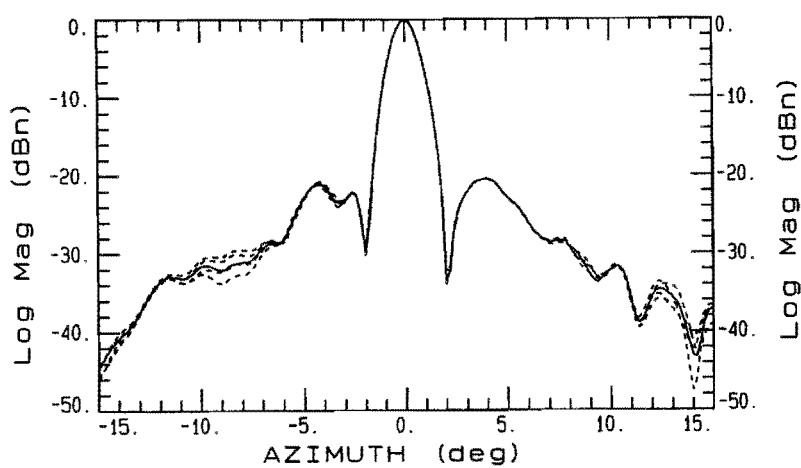
Figure A4.17 Azimuth scan, amplitude, H-plane, down, f=11.5 GHz, cont.line: corrected, dot.line: measured.
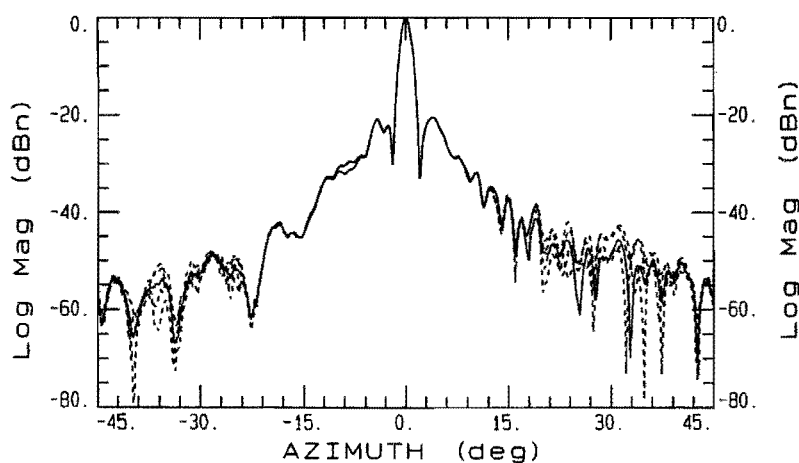
Figure A4.18 Azimuth scan, amplitude, H-plane, down, f=11.5 GHz, cont.line: corrected, dot.line: measured.
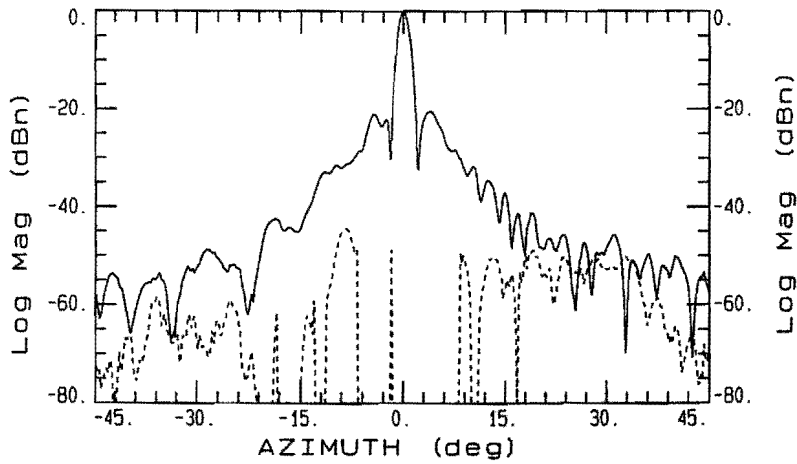
Figure A4.19 *Azimuth scan, amplitude, H-plane, down, f=11.5 GHz, cont.line: corrected, dot.line: residual component.*
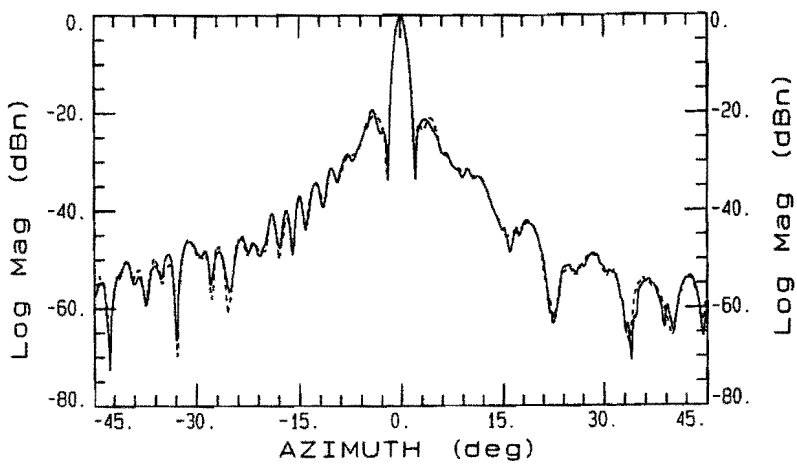
Figure A4.20 *Azimuth scan, corrected, amplitude, H-plane, f=11.5 GHz, cont.line: up, dot.line: down.*
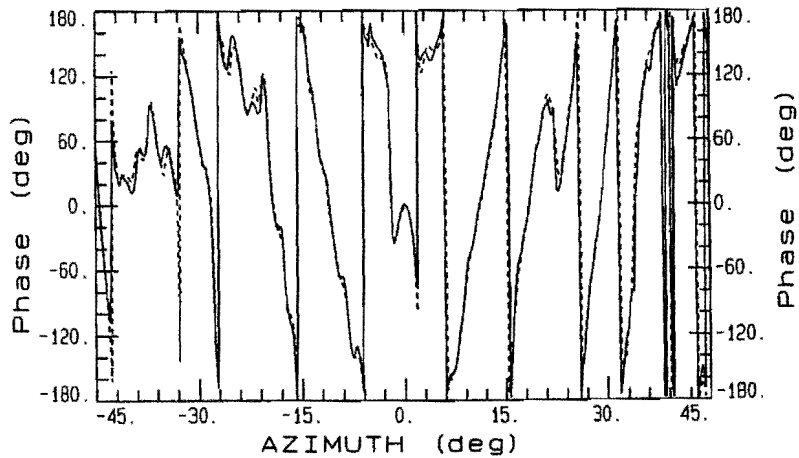
Figure A4.21 *Azimuth scan, corrected, phase, H-plane, f=11.5 GHz, cont.line: up, dot.line: down.*
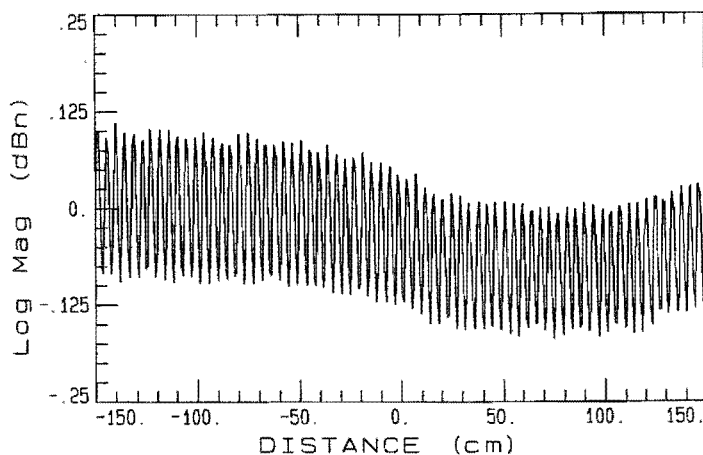
Figure A4.22 Longitudinal scan, 45°-plane c, up, az= 0°, f=11.5 GHz.
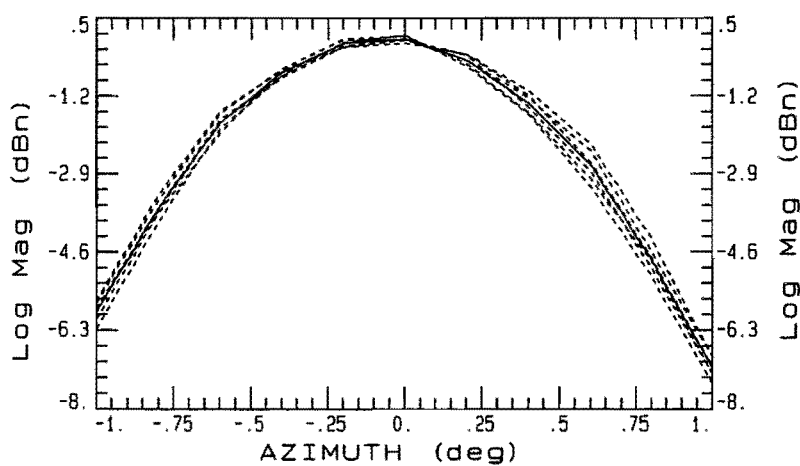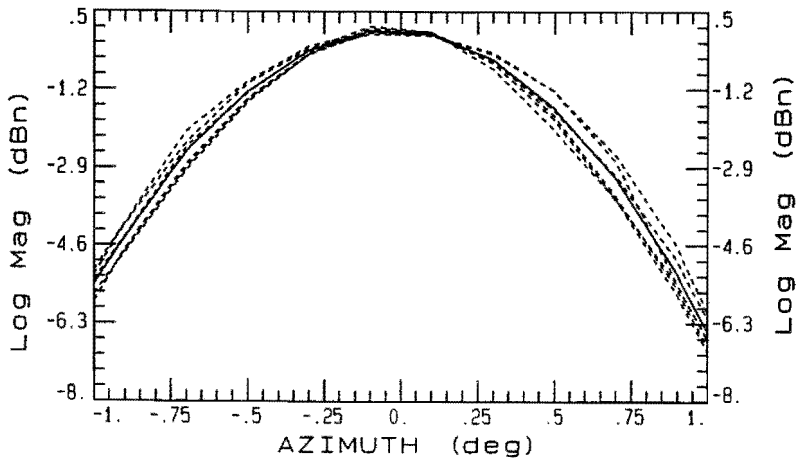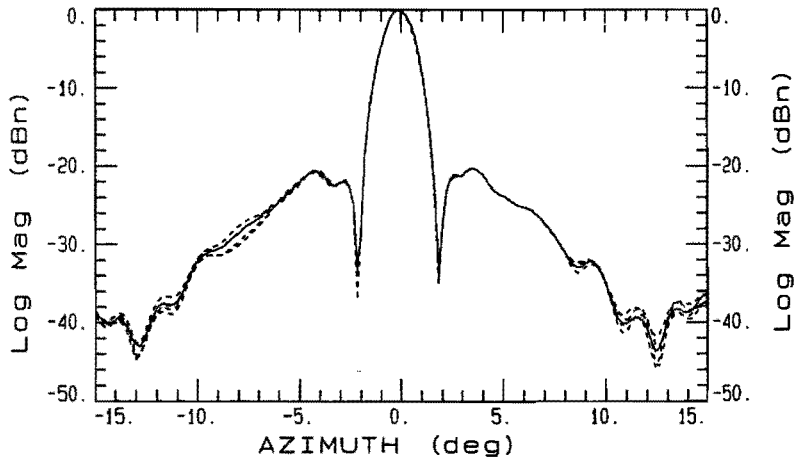

Figure A4.23 Azimuth scan, amplitude, 45°-plane c, up, f=11.5 GHz, cont.line: corrected, dot.line: measured.

Figure A4.24 Azimuth scan, mutual coupling component, 45°-plane c, up, f=11.5 GHz, cont.line: novel APC, dot.line: gated.

Figure A4.25 *Azimuth scan, amplitude, 45°-plane c, up, f=11.5 GHz, cont.line: corrected, dot.line: measured.*

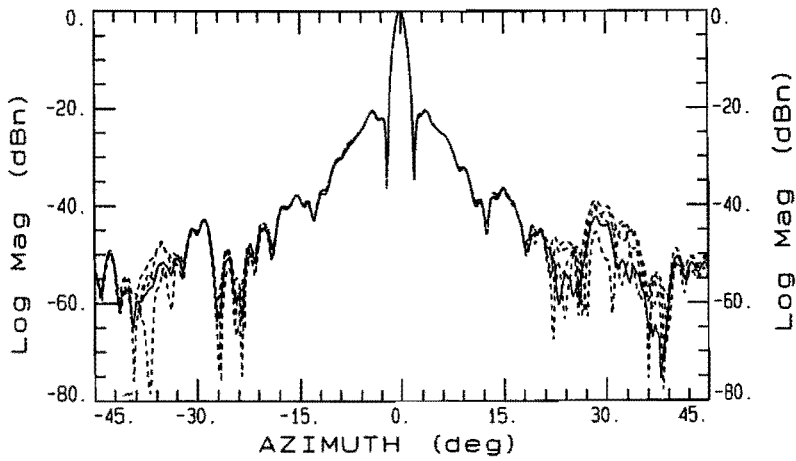**Figure A4.26** *Azimuth scan, amplitude, 45°-plane c, up, f=11.5 GHz, cont.line: corrected, dot.line: measured.*

Figure A4.27 *Azimuth scan, phase, 45°-plane c, up, f=11.5 GHz, cont.line: corrected, dot.line: measured.*

Figure A4.28 *Azimuth scan, amplitude, 45°-plane c, up, f=11.5 GHz, cont.line: corrected, dot.line: residual component.*
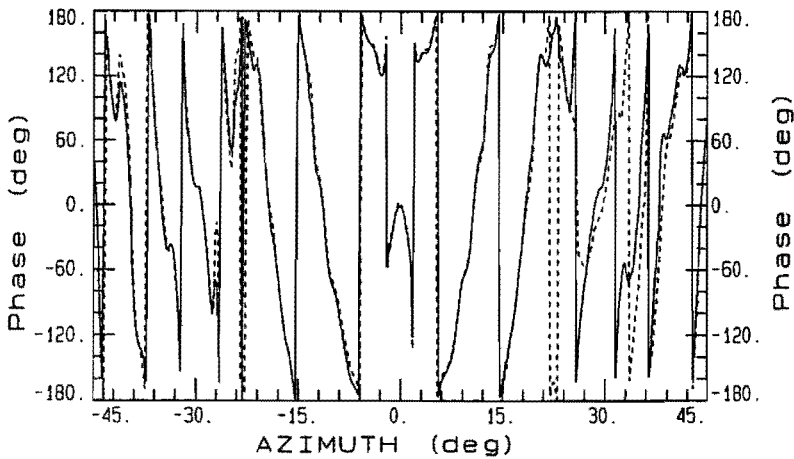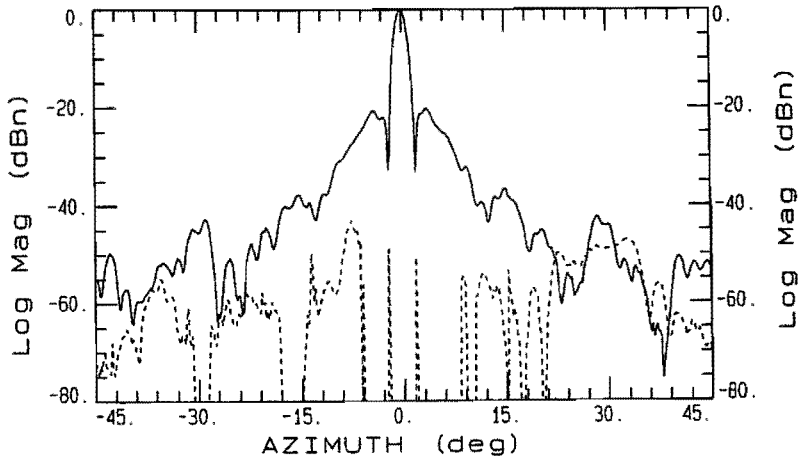

Figure A4.29 *Azimuth scan, amplitude, 45°-plane c, up, f=11.5 GHz, cont.line: novel APC, dot.line: gated.*

Figure A4.30 *Azimuth scan, phase, 45°-plane c, up, f=11.5 GHz, cont.line: novel APC, dot.line: gated.*

Figure A4.31 *Longitudinal scan, 45°-plane c, down, az= 0°, f=11.5 GHz.*
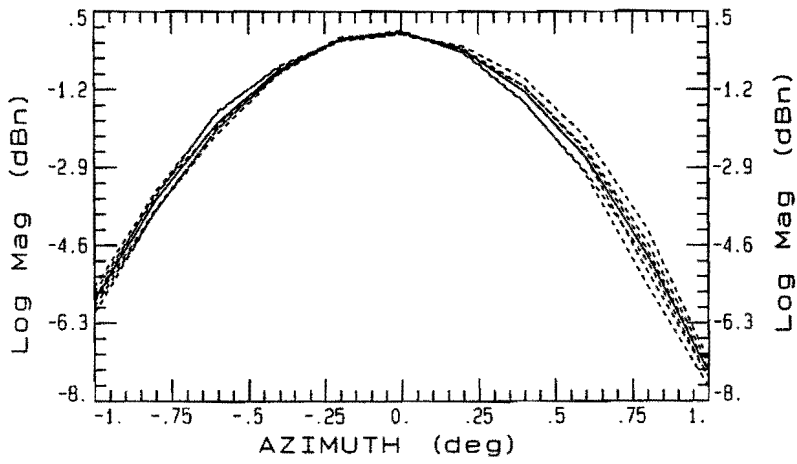
Figure A4.32 *Azimuth scan, amplitude, 45°-plane c, down, f=11.5 GHz, cont.line: corrected, dot.line: measured.*

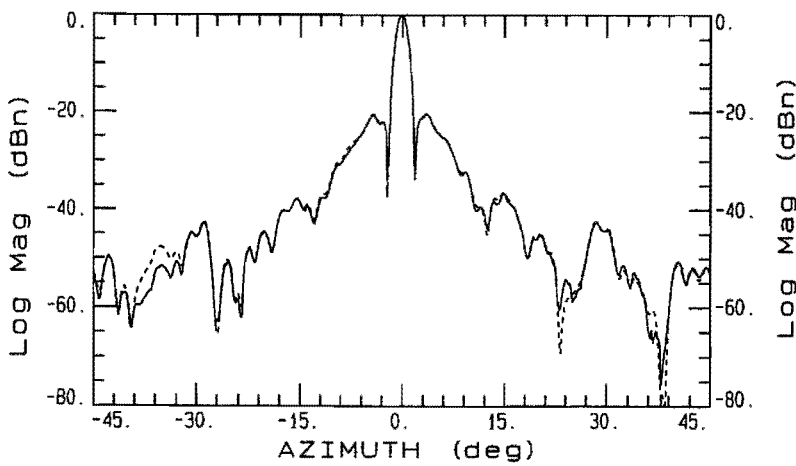**Figure A4.33** *Azimuth scan, amplitude, 45°-plane c, down, f=11.5 GHz, cont.line: corrected, dot.line: measured.*

Figure A4.34 *Azimuth scan, amplitude, 45°-plane c, down, f=11.5 GHz, cont.line: corrected, dot.line: measured.*

Figure A4.35 *Azimuth scan, amplitude, 45°-plane c, down, f=11.5 GHz, cont.line: corrected, dot.line: residual component.*
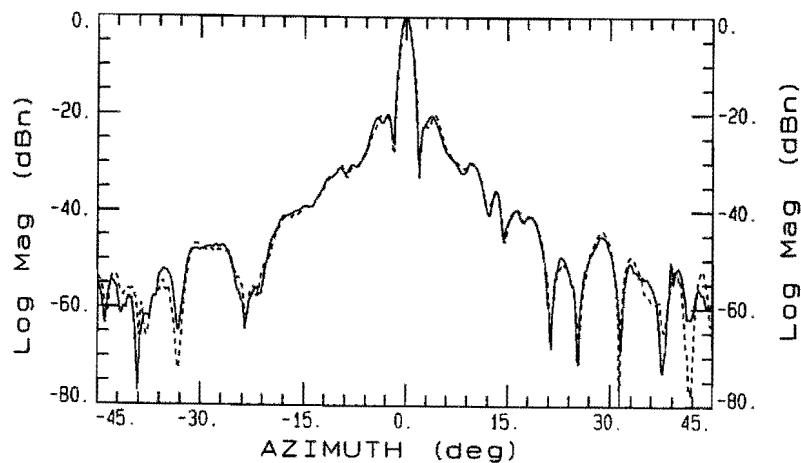
Figure A4.36 *Azimuth scan, corrected, amplitude, 45°-plane c, f=11.5 GHz, cont.line: up, dot.line: down.*
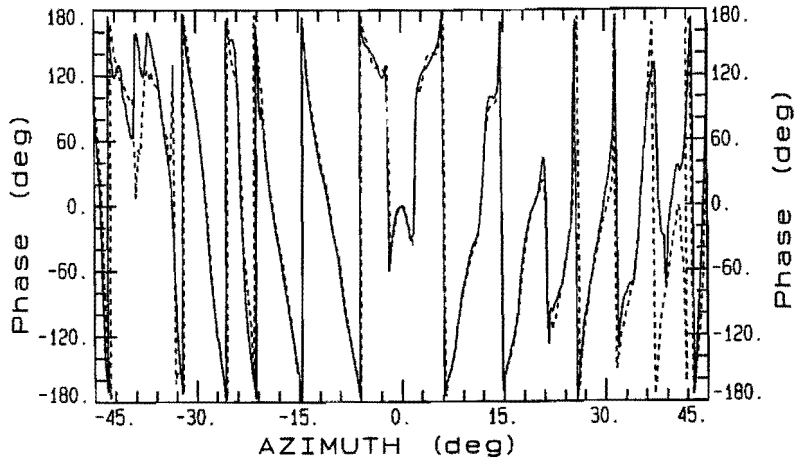
Figure A4.37 *Azimuth scan, corrected, phase, 45°-plane c, f=11.5 GHz, cont.line: up, dot.line: down.*
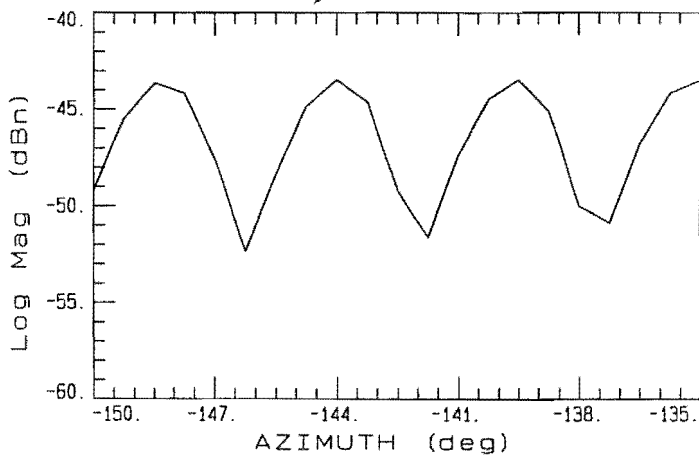
Figure A4.38 *Longitudinal scan, 45°-plane x, az= 0°, f=11.5 GHz.*
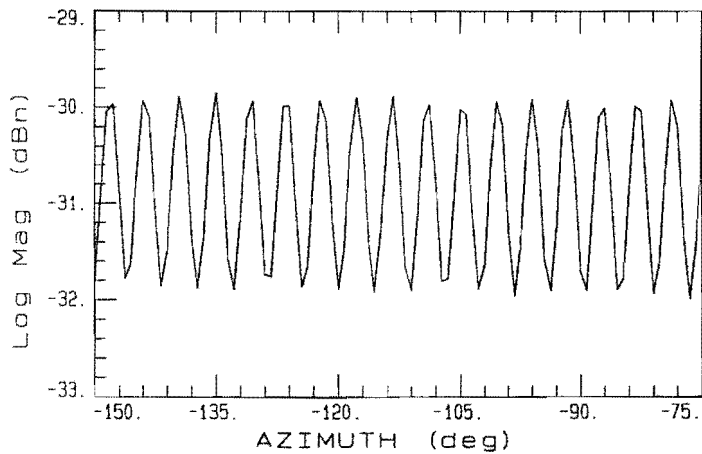
Figure A4.39 *Longitudinal scan, 45°-plane x, az= -1°, f=11.5 GHz.*
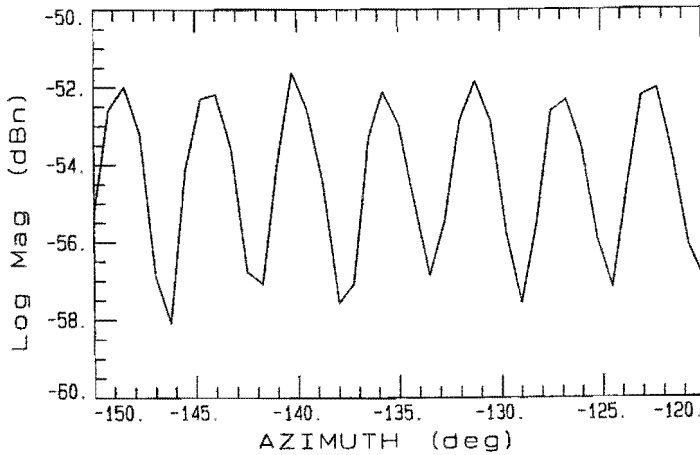
Figure A4.40 *Longitudinal scan, 45°-plane x, az= 3.5°, f=11.5 GHz.*

Figure A4.41 *Azimuth scan, amplitude, 45°-plane x, f=11.5 GHz, cont.line: corrected, dot.line: measured.*

Figure A4.42 *Azimuth scan, amplitude, 45°-plane x, f=11.5 GHz, cont.line: corrected, dot.line: measured.*

Figure A4.43 *Azimuth scan, amplitude, 45°-plane x, f=11.5 GHz, cont.line: corrected, dot.line: residual component.*
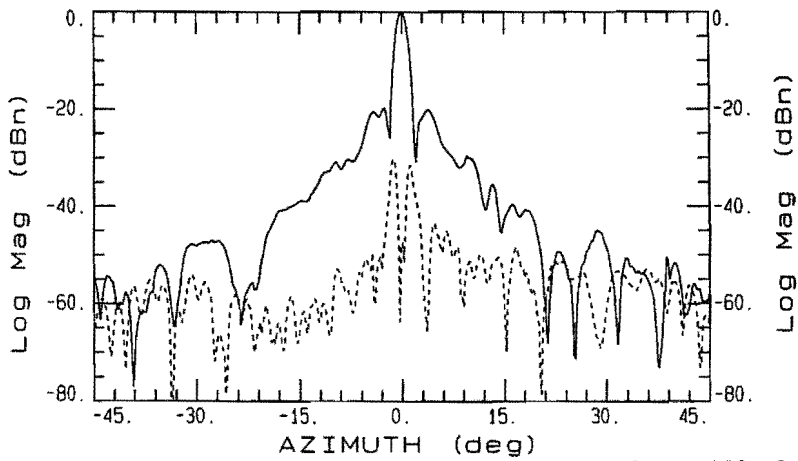
Figure A4.44 *Azimuth scan, corrected, f=11.5 GHz, cont.line: 45°-plane c, dot.line: 45°-plane x.*
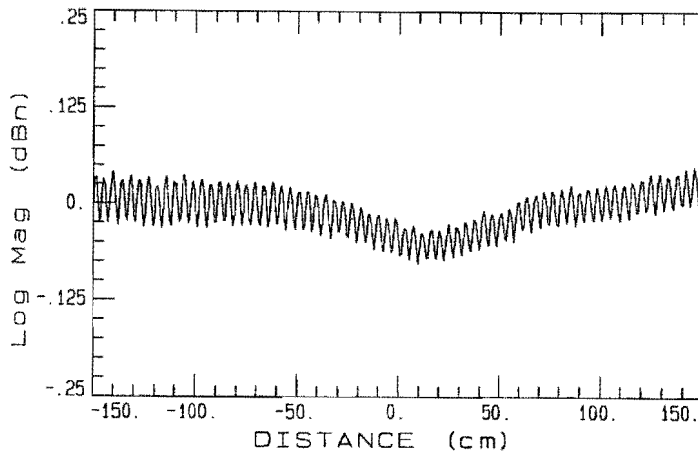
Figure A4.45 *Longitudinal scan, E-plane, az= 0°, f=11.5 GHz.*
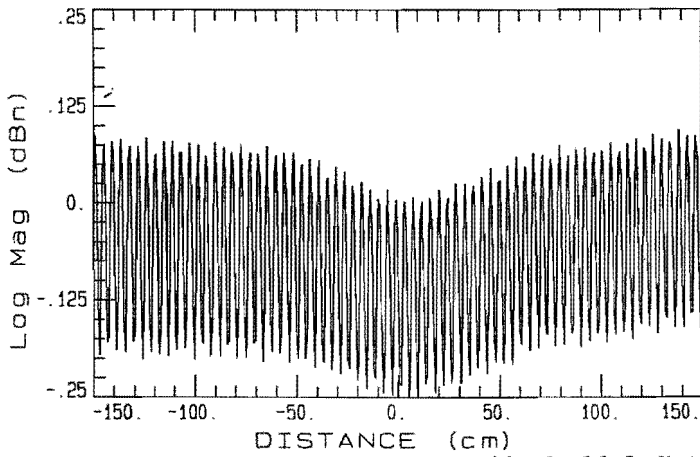
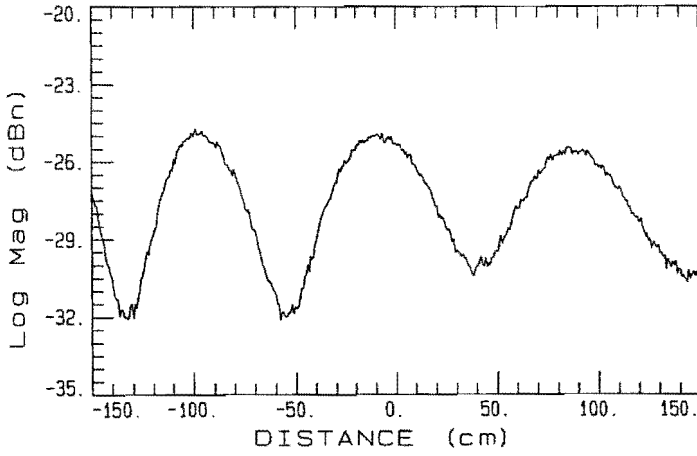**Figure A4.46** *Longitudinal scan, E-plane, az= 0°, f=11.8 GHz.*
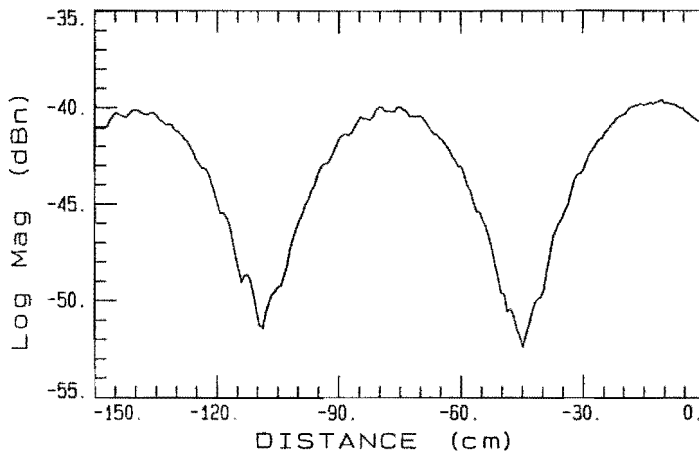
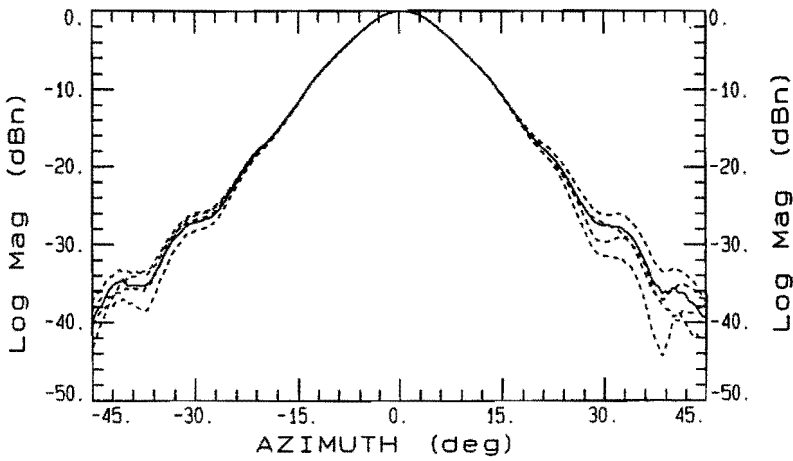**Figure A4.47** *Longitudinal scan, E-plane, az= 30°, f=11.5 GHz.*

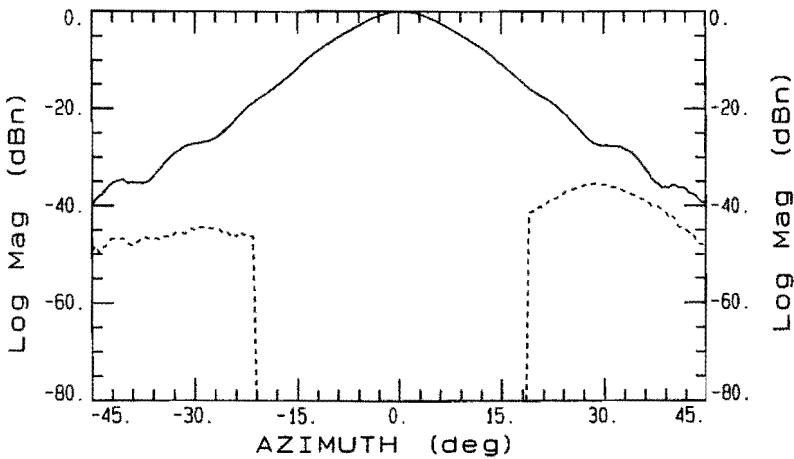**Figure A4.48** *Azimuth scan, amplitude, E-plane, f=11.5 GHz, cont.line: corrected, dot.line: measured.*

Figure A4.49 *Azimuth scan, amplitude, E-plane, f=11.5 GHz, cont.line: corrected, dot.line: measured.*

Figure A4.50 *Azimuth scan, amplitude, E-plane, f=11.5 GHz, cont.line: corrected, dot.line: measured.*

Figure A4.51 *Azimuth scan, phase, E-plane, f=11.5 GHz, cont.line: corrected, dot.line: measured.*

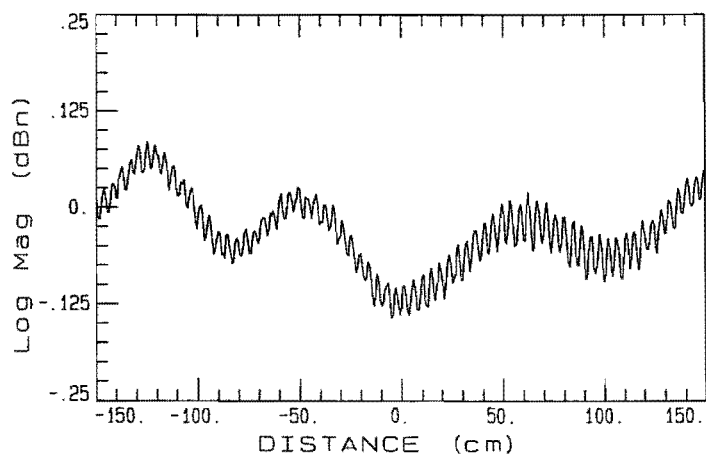**Figure A4.52** *Azimuth scan, amplitude, E-plane, f=11.5 GHz, cont.line: corrected, dot.line: residual component.*

Figure A4.53 *Azimuth scan, amplitude, E-plane, f=11.5 GHz, cont.line: novel APC, dot.line: gated.*
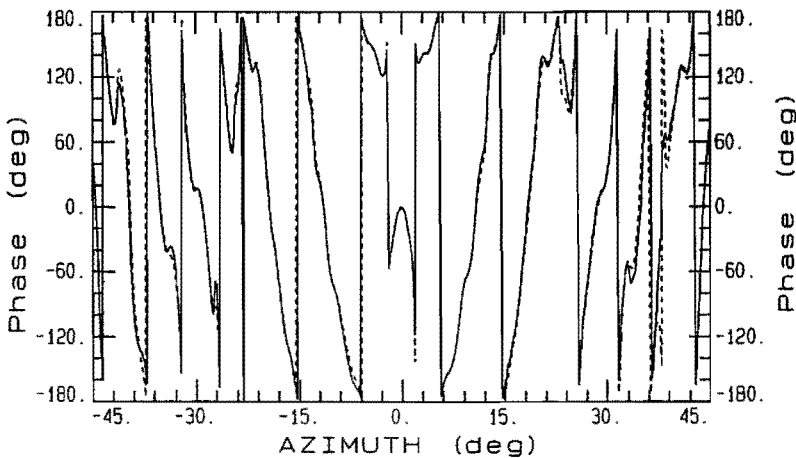
Figure A4.54 *Azimuth scan, phase, E-plane, f=11.5 GHz, cont.line: novel APC, dot.line: gated.*
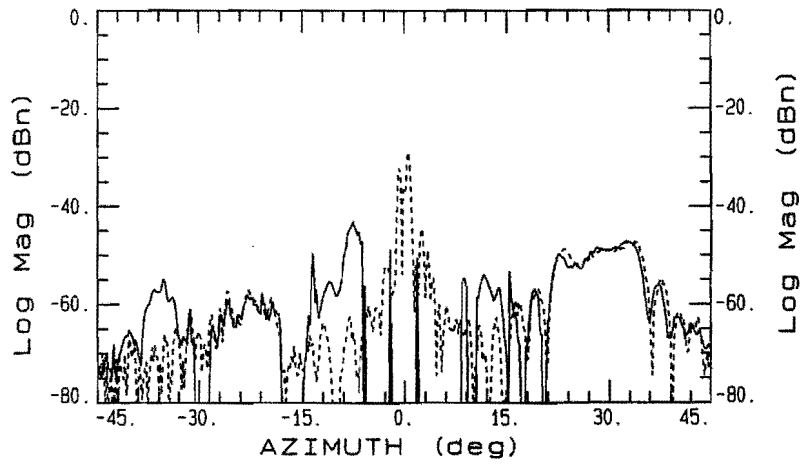
Figure A4.55 *Azimuth scan, residual component, E-plane, f=11.5 GHz, cont.line: novel APC, dot.line: gated.*

A.5 Horn

On longitudinal distance scales: 1cm= 3mm in reality.
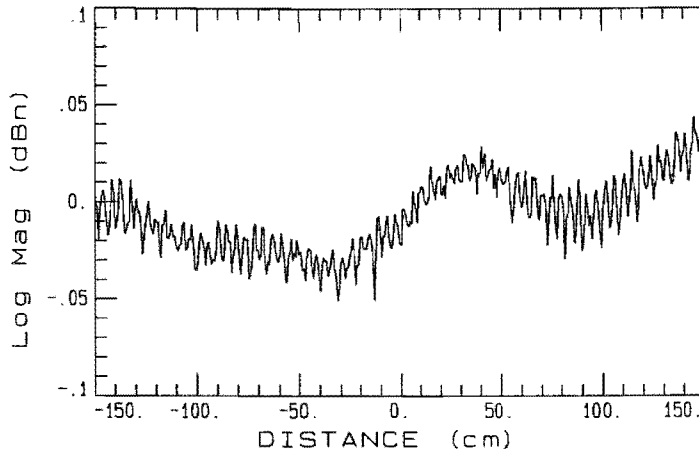
Figure A5.1 *Longitudinal scan, H-plane, az= 0°, f=11.5 GHz.*
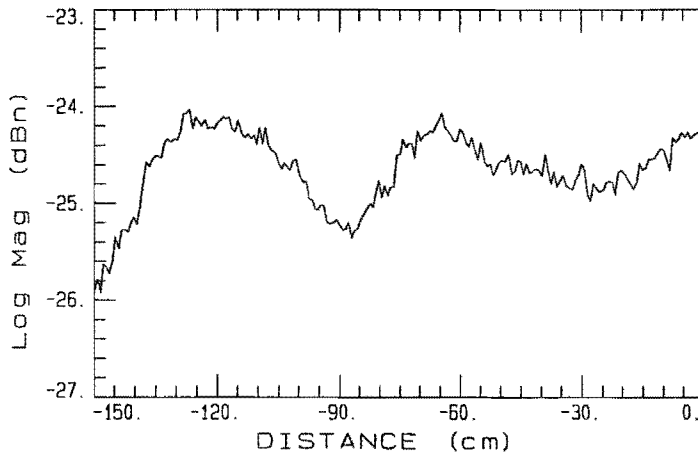
Figure A5.2 *Longitudinal scan, H-plane, az= -26°, f=11.5 GHz.*
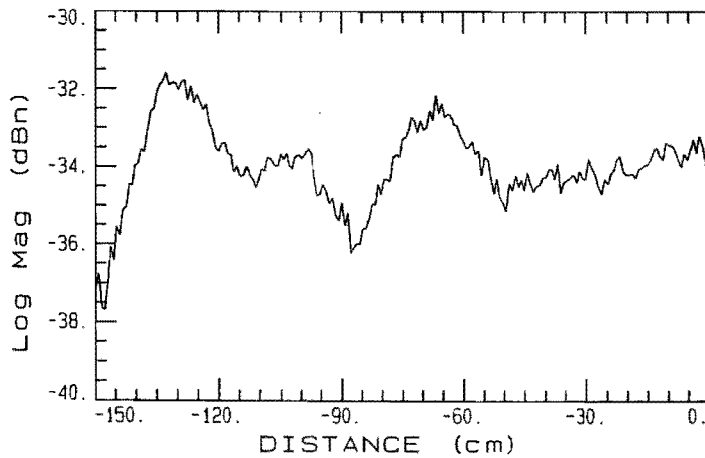
Figure A5.3 *Longitudinal scan, H-plane, az= -36°, f=11.5 GHz.*

Figure A5.4 *Longitudinal scan, H-plane, az= 30°, f=11.5 GHz.*

Figure A5.5 *Azimuth scan, amplitude, H-plane, f=11.5 GHz, cont.line: corrected, dot.line: measured.*

Figure A5.6 *Azimuth scan, amplitude, H-plane, f=11.5 GHz, cont.line: corrected, dot.line: residual component.*

Figure A5.7 *Longitudinal scan, E-plane, az= 0°, f=11.5 GHz.*
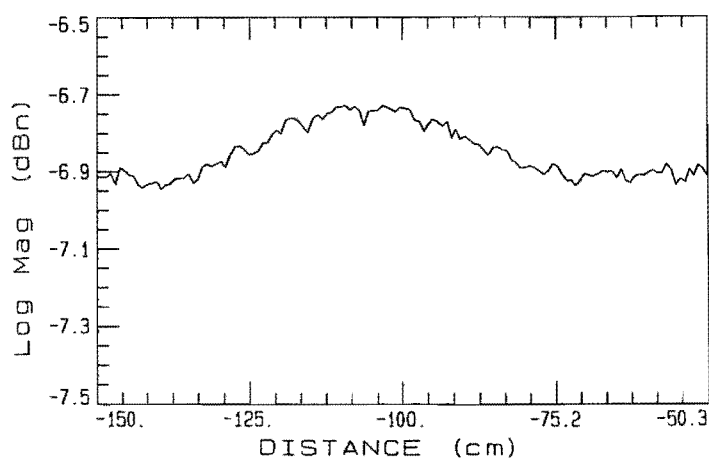
Figure A5.8 *Longitudinal scan, E-plane, az= -14°, f=11.5 GHz.*
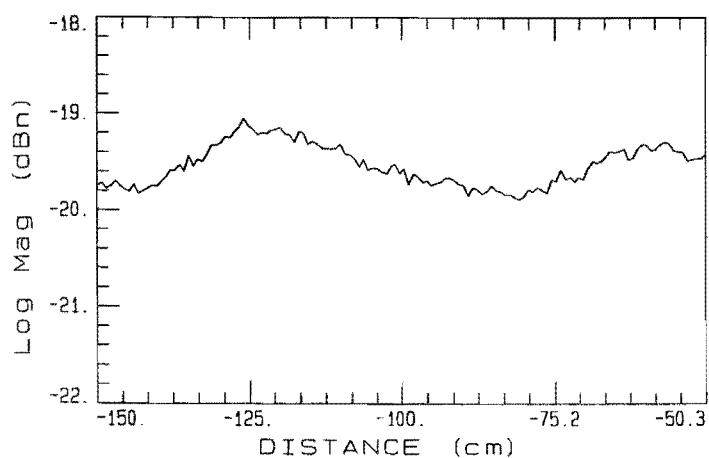
Figure A5.9 *Longitudinal scan, E-plane, az= -40°, f=11.5 GHz.*
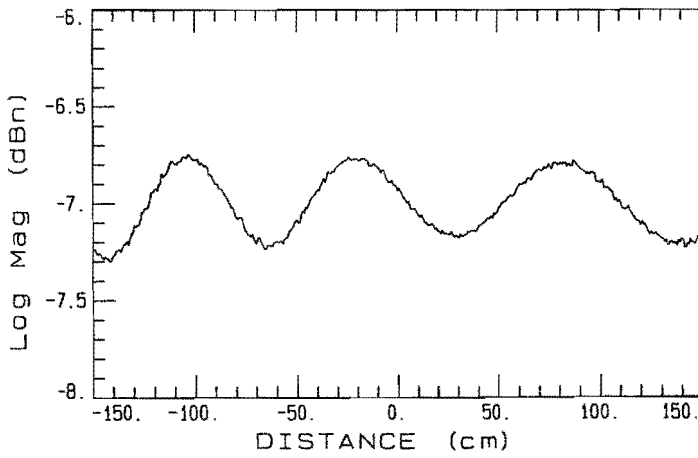
Figure A5.10 *Longitudinal scan, E-plane, az= 14°, f=11.5 GHz.*

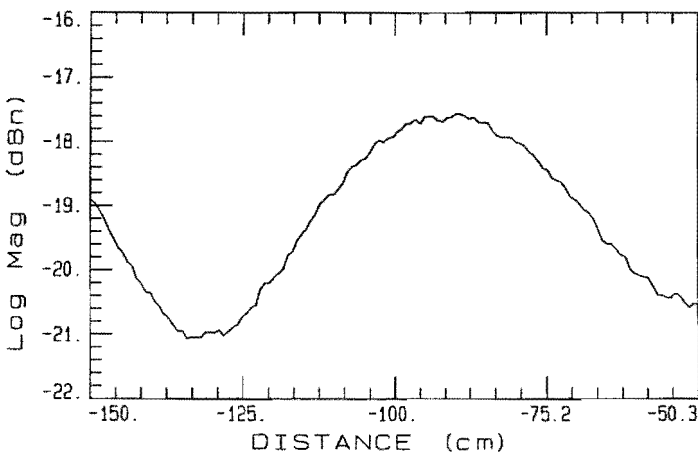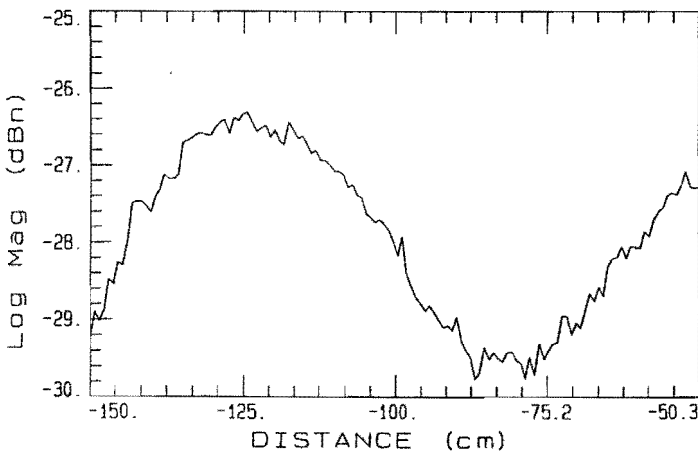**Figure A5.11** *Longitudinal scan, E-plane, az= 30°, f=11.5 GHz.*

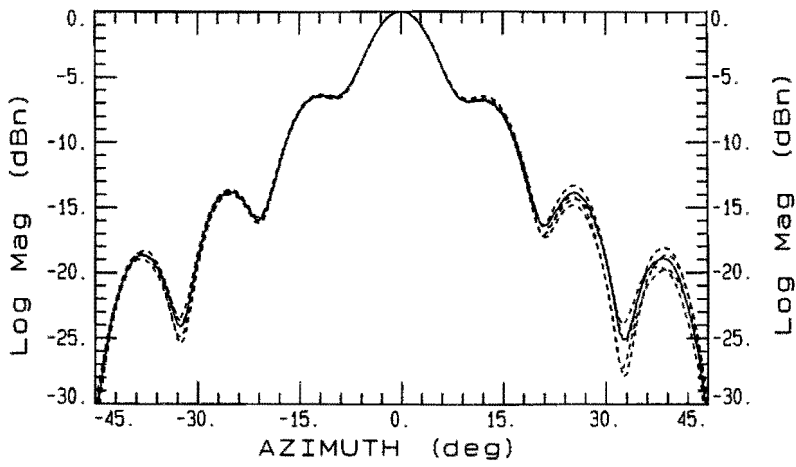**Figure A5.12** *Longitudinal scan, E-plane, az= 45°, f=11.5 GHz.*

Figure A5.13 Azimuth scan, amplitude, E-plane, f=11.5 GHz, cont.line: corrected, dot.line: measured.
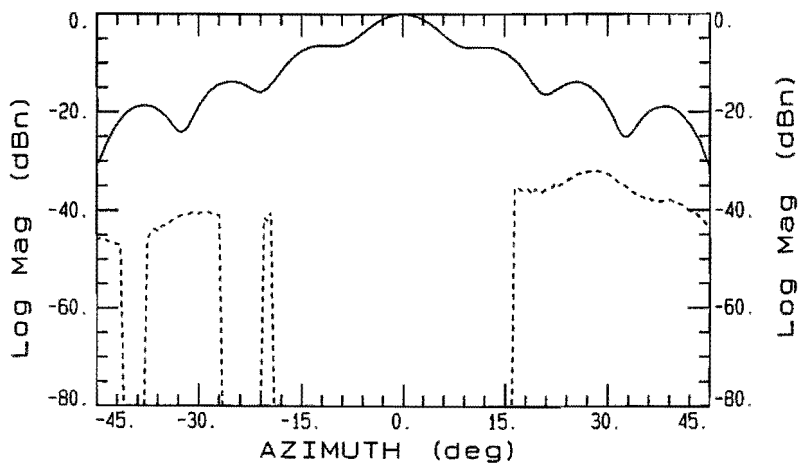

Figure A5.14 Azimuth scan, amplitude, E-plane, f=11.5 GHz, cont.line: corrected, dot.line: residual component.